Structure formation and fractionation in systems of colloidal rods

Dissertation

zur Erlangung des akademischen Grades
,,doctor rerum naturalium"
(Dr. rer. nat.)
in der Wissenschaftsdisziplin ,,Theoretische Physik"

eingereicht an der
Mathematisch-Naturwissenschaftlichen Fakultät der Universität Potsdam

angefertigt am
Max-Planck-Institut für Kolloid- und Grenzflächenforschung in Potsdam

von

Andreas Richter

geboren am 20. September 1977 in Bayreuth

Potsdam, im Januar 2007

Abstract

Nowadays, colloidal rods can be synthesized in large amounts. The rods are typically cylindrically and their length ranges from several nanometers to a few micrometers. In solution, systems of colloidal rodlike molecules or aggregates can form liquid-crystalline phases with long-range orientational and spatial order. In the present work, we investigate structure formation and fractionation in systems of rodlike colloids with the help of Monte Carlo simulations in the NPT ensemble.

Repulsive interactions can successfully be mimicked by the hard rod model, which has been studied extensively in the past. In many cases, attractive interactions like van der Waals or depletion forces cannot be neglected, however. In the first part of this work, the phase behavior of monodisperse attractive rods is characterized for different interaction strengths. Phase diagrams as a function of rod length and pressure are presented.

Most systems of synthesized mesoscopic rods have a polydisperse length distribution as a consequence of the longitudinal growth process of the rods. For many technical and research applications, a rather small polydispersity is desired in order to have well defined material properties. The polydispersity can be reduced by a spatial demixing (fractionation) of long and short rods. Fractionation and structure formation is studied in a tridisperse and a polydisperse bulk suspension of rods. We observe that the resulting structures depend distinctly on the interaction strength. The fractionation in the system is strongly enhanced with increasing interaction strength.

Suspensions are typically confined in a container. We also examine the influence of adjacent substrates in systems of tridisperse and polydisperse rod suspensions. Three different substrate types are studied in detail: a planar wall, a corrugated substrate, and a substrate with rectangular cavities. We analyze the fluid structure close to the substrate and substrate controlled fractionation. The spatial arrangement of long and short rods in front of the substrate depends sensitively on the substrate structure and the pressure. Rods with a predefined length are segregated at substrates with rectangular cavities.

Zusammenfassung

Kolloidale Stäbchen können mittlerweile in großen Mengen hergestellt werden. Die Form der Stäbchen ist in der Regel zylinderförmig und ihre Länge reicht von einigen Nanometern bis hin zu wenigen Mikrometern. Systeme aus kolloidalen stäbchenförmigen Molekülen oder Aggregaten können in Lösung flüssigkristalline Phasen mit langreichweitiger Orientierungs- und Raumordnung ausbilden. Im Rahmen dieser Arbeit werden Strukturbildung und Fraktionierung in Systemen aus stäbchenförmigen Kolloiden mittels Monte Carlo Simulationen im NPT Ensemble untersucht.

Replusive Wechselwirkungen können erfolgreich durch harte Stäbchen modelliert werden. Dieses Modell wurde in der Vergangenheit bereits ausgiebig untersucht. Oft jedoch können attraktive Wechselwirkungen, wie z. B. van der Waals- oder Depletionskräfte, nicht vernachlässigt werden. Im ersten Teil dieser Arbeit wird das Phasenverhalten von monodispersen attraktiven Stäbchen bei unterschiedlichen Wechselwirkungsstärken charakterisiert. Es werden Phasendiagramme bezüglich der Parameter Druck und Stäbchenlänge präsentiert.

Die überwiegende Mehrzahl von Systemen aus synthetisierten mesoskopischen Stäbchen weist eine polydisperse Längenverteilung aufgrund des Längswachstums auf. Für eine Reihe technischer und wissenschaftlicher Anwendungen sind hingegen schmale Längenverteilungen wünschenswert, um wohl definierte Materialeigenschaften zu haben. Die Polydispersität kann durch räumliche Trennung (Fraktionierung) langer und kurzer Stäbchen reduziert werden. Fraktionierung und Strukturbildung werden in einer tridispersen und einer polydispersen Suspension untersucht. Wir beobachten, dass die entstehenden Strukturen ganz wesentlich von der Wechselwirkungsstärke abhängen. Der Grad der Fraktionierung wird durch Attraktivität stark erhöht.

Suspensionen befinden sich typischerweise in Gefäsen. Wir untersuchen daher auch den Einfluss von begrenzenden Substraten auf Systeme aus tridispersen und polydispersen Stäbchensuspensionen. Drei verschiedene Substratstrukturen werden genauer betrachtet: Eine planare Wand, ein riefenförmiges Substrat und Substrate mit rechteckigen Aussparungen. Wir untersuchen die Flüssigkeitsstruktur in Substratnähe und substratinduzierte Fraktionierung. Die räumliche Anordnung von langen und kurzen Stäbchen hängt sehr sensibel von der Substratstruktur und dem Druck ab. Stäbchen mit einer festgelegten Länge werden an Substraten mit rechteckigen Aussparungen abgesondert.

Contents

List of symbols

β	inverse thermal energy, page 14
ΔG	free energy difference, page 24
D	diameter of spherocylinder, page 8
D_a	range of attractive potential, Eq. (2.15) on page 17
ϵ	potential depth, Eq. (2.15) on page 17
ϵ^*	reduced potential depth, page 35
$E_{\min}$	strongest pair interaction energy, Eq. (2.19) on page 18
$\langle E_{\mathrm{rod}} \rangle$	average rod energy, page 36
$g_{\|\|}(r_{\|\|})$	longitudinal pair correlation function, page 30
$g_{\perp}(r_{\perp})$	transverse pair correlation function, page 30
$g_{\theta}(z)$	orientational correlation function, Eq. (2.46) on page 33
$g_{\phi}(z)$	orientational correlation function, page 33
$G(N,P,T)$	Gibbs free energy, page 15
kT	thermal energy, page 14
λ	axis ratio, page 8
L	length of spherocylinder, page 8
$\mathbf{n}$	global director, page 29
N	particle number, page 13
P_B	Boltzmann factor, Eq. (2.21) on page 20
P^*	reduced pressure, page 35
$\mathcal{Q}$	configurational part of the partition function, Eq. (2.22) on page 20
$Q(N,P,T)$	partition function in NPT ensemble, page 15
$\rho^*(z)$	density distribution function, Eq. (2.39) on page 31
$\rho^*_{\lambda}(z)$	axis ratio resolved density distribution function, Eq. (2.40) on page 32
$\rho^*_{\lambda_1,\lambda_2}(z)$	cumulative density distribution function, Eq. (2.41) on page 32
$S(N)$	nematic order parameter in a finite system, Eq. (2.36) on page 29
S_{∞}	nematic order parameter in an infinite system, Eq. (2.38) on page 30
$\mathbf{u}_i$	rod orientation, page 2
U_{AR}	attractive rod potential, Eq. (2.18) on page 17
$U^{\mathrm{sw}}(r)$	square-well potential, Eq. (2.13) on page 17
V	volume, page 14
$x_{\lambda}(z)$	spatially resolved mole fraction, Eq. (2.42) on page 32
$x^{\mathrm{int}}_{\lambda}$	integrated mole fraction, Eq. (2.43) on page 32
x_C	length of the cavities, page 61
y_C	width of the grooves / cavities, page 61
z_C	heigth of the grooves / cavities, page 61

Chapter 1

Introduction

During the last years, more and more rigid, rodlike colloids have been created synthetically. Examples are carbon nanotubes [36], boehmite needles [10], cylindrical dendrimers [74], and metallosupramolecular coordination polyelectrolytes (MEPE) [42]. Rodlike molecules can serve as building blocks for mesoscopic structures and are able to self-aggregate. Like small liquid crystal molecules, colloidal rods can form phases with long-range spatial and/or orientational order. The length scale of such rods typically ranges from several nanometers to a few micrometers. Colloidal zinc oxide (ZnO) nanorods, for example, can be utilized in gas sensors [25] or in thin-film field-effect transistors [81]. Rods can be used as templates for a controlled creation of porous materials [40], as electrically conducting nanowires [20], as waveguides [84], or as building blocks for scaffold-like networks [12]. For many applications, a rather monodisperse length distribution is desirable. Most synthesis methods produce a suspension with a polydisperse length distribution because of the longitudinal growth process. Fractionation is a possibility to establish a sorting mechanism in polydisperse suspensions. This work is dedicated to investigate structure formation and fractionation effects in polydisperse systems of rodlike colloids. Special attention is paid to the influence of attractive rod interactions [67] and the impact of patterned adjacent substrates [68].

1.1 Basic aspects about liquid crystals

First of all some basic aspects about liquid crystals. We all know from everyday experiences that substances appear in different phases like the solid, fluid, and gaseous phase. Water, for example, is crystalline at temperatures below $0°C$, fluid in the temperature range between $0°C$ and $100°C$, and gaseous at temperatures above $100°C$. Besides these three well known phases

of matter other phases exist in nature as well. One example is the plasma, which occurs at extremely high temperatures like in stars. Another class of phases are the so-called liquid crystalline phases and parts of this work aim at their characterization in the employed model system.

The name liquid crystal itself is confusing. How can a liquid be crystalline or how can a crystal be fluid at the same time? The nomenclature for this specific state of matter makes sense, indeed, since a liquid crystal combines aspects of both the fluid and the crystalline phase. A liquid crystal behaves like a fluid in that it flows and can be deformed easily. At the same time long-range positional and/or orientational order is present as in crystals. The first experimental observation of liquid crystalline behavior was described by Reinitzer in 1888 [66]. Around 1900, Otto Lehmann identified the substances as a new thermodynamically stable phase and created the term liquid crystal. The names mesophase or mesomorphic phase (mesos (Greek) = middle, intermediate) is also widely used.

Liquid crystalline behavior is essentially connected to a strong anisotropy of the underlying molecules. Thus, every molecule has a combination of positional and orientational degrees of freedom. In the crystalline state, positions as well as orientations of the molecules are strongly constrained. The molecules are arranged on a lattice and the orientations are also fixed. When a solid melts to a liquid, positional and orientational order disappears at the same time. If, however, parts of the positional order or some kind of orientational order is preserved above the melting point, the system is in a liquid crystalline state. Single component systems, which show liquid crystalline behavior in a certain temperature range are called thermotropic. If the molecules are in solution, the liquid crystal is said to be lyotropic and the amount of solvent is a dominant control parameter. Colloidal systems studied in this work are typically lyotropic.

1.1.1 Liquid crystalline phases

The most common liquid crystalline phases are formed by rodlike molecules, which unify an elongated shape and a considerable rigidity. The orientation of a rigid body in three dimensions is determined by three coordinates, e. g. the Euler angles [30]. For the description of rodlike molecules, rotations around the long axis can usually be neglected. Thus, the orientation of each molecule i is specified by a unit vector $\mathbf{u}_i$, which is parallel to the rod axis. Rodlike molecules typically have a head-tail symmetry, i. e. $\mathbf{u}_i$ and $-\mathbf{u}_i$ are equivalent. A nematic liquid crystal is characterized by a high degree of long-range orientational order whereas the spatial correlations are short-ranged like those of a liquid. Most rod orientations $\mathbf{u}_i$ point along

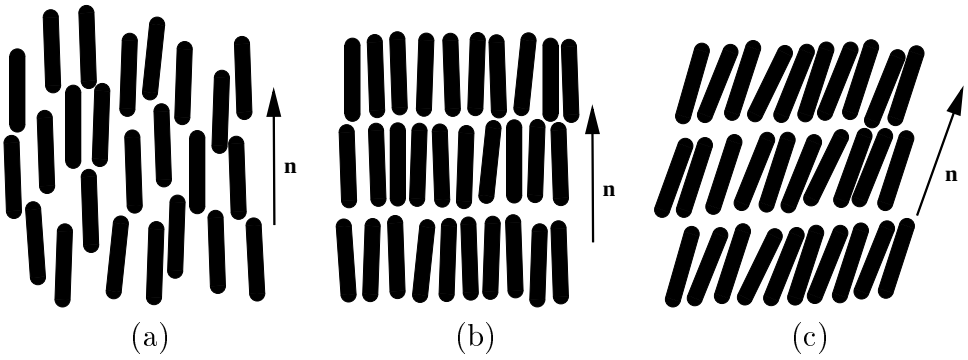

Figure 1.1: Illustrations of three different liquid crystals. (a) In the nematic phase, the rods align a global director $\mathbf{n}$. (b) In the smectic A phase, the rods are additionally arranged in layers. (c) In a smectic C liquid crystal, the orientation of the rods and the layer normal are different.

the global director $\mathbf{n}$ as sketched in Fig. 1.1 (a). The second big class of liquid crystalline phases exhibit smectic order. Here, orientational and one-dimensional spatial order emerge simultaneously. The molecules are arranged in layers as depicted in Fig. 1.1 (b) and (c). In the smectic A (SmA) and smectic C (SmC) phase each layer basically represents a two-dimensional fluid with the rods diffusing freely within the layer but only rarely between the layers. In a smectic A phase, the layer normal coincides with the global director $\mathbf{n}$. If $\mathbf{n}$ is tilted with respect to the layer normal, the phase is called smectic C. Both the smectic A and smectic C possess only short-range in-plane correlations between the molecule positions - typically in the range of a few molecule diameters. Another example of a smectic phase is the smectic B phase where bond-orientational order exists. In difference to a crystal, the molecules are not arranged on a lattice, i. e. there is no long-range spatial order. The in plane correlation function of a smectic B phase, however, has the characteristics of hexatic order. Smectic liquid crystals are often more viscous than nematics.

A special case of the nematic phase is a cholesteric liquid crystal as sketched in Fig. 1.2. The director of neighboring nematic layers is turned by a constant angle around an axis perpendicular to the director. A rotation of 360° defines the helical pitch height p. The majority of liquid crystalline substances show the nematic or smectic behavior introduced so far. A larger variety of liquid crystalline phases occurs in nature, however [17, 93].

Beneath rodlike molecules, a disklike shape of molecules leads to liquid crystalline phases, too. The normal vector on the disk plane represents the orientation of such a molecule. The nematic phase is characterized by a

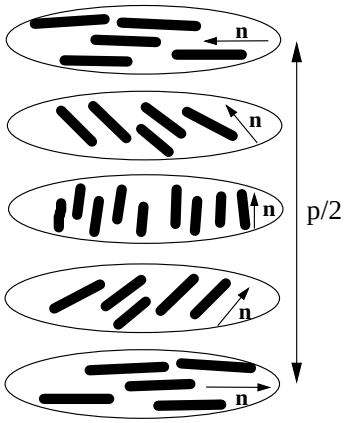

Figure 1.2: Illustration of a cholesteric liquid crystal. The nematic director $\mathbf{n}$ turns by 360° within the helical pitch height p.

global director $\mathbf{n}$, again, which is the average direction of the orientations as illustrated in Fig. 1.3 (a). A drawing of a columnar phase is given in Fig. 1.3 (b). Here, the molecules arrange themselves in columns in addition to the orientational order. The columns themselves form often hexagonal structures. Diskotic liquid crystals are subject of investigations for more than 30 years [39, 41, 87] but rodlike molecules are the predominant class of substances, which form liquid crystals. In this work, rodlike molecules will be considered, exclusively.

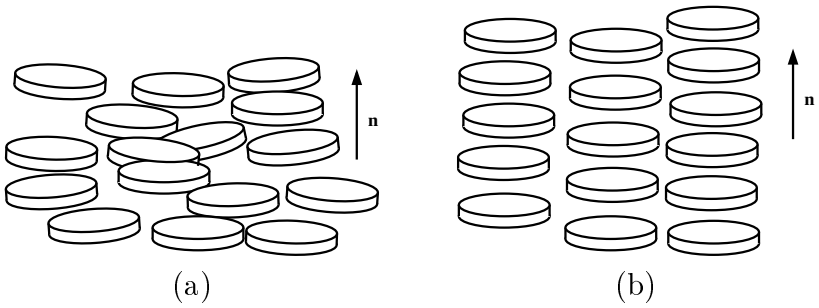

Figure 1.3: Schematic drawing of (a) the nematic and (b) the columnar phase in diskotic liquid crystals.

1.1.2 Applications of liquid crystals

The research in liquid crystals as a state of matter is of fundamental interest for its own. In addition, liquid crystals gained considerable importance in technical applications. The anisotropy of the liquid crystalline phases makes

these materials birefringent. As a consequence, the orientation of polarized light can be changed by the material.

The big advantage of a liquid crystal as a birefringent substance is that a setup of two crossed polarizers and the liquid crystal in between can be employed as a voltage controlled light valve. This property is the basis for the widespread usage of liquid crystals nowadays in displays (LCD) of devices like notebooks, flatscreens, or mobile phones. In 1971, Schadt and Helfrich reported on the voltage-dependent optical activity of a twisted nematic liquid crystal [71]. Up to now, the development of liquid crystal displays evolves rapidly and has become a billion dollar business [72, 77, 82, 83].

The simplest setup of the unit cell of a liquid crystal display is the so-called twisted nematic (TN) cell. Further developments with improved characteristics comprise, e. g. the super twisted nematic (STN) and the triple super twisted nematic (TSTN) LCD [82]. The operating mode of a TN unit cell is illustrated in Fig. 1.4. A nematic liquid crystal is located between two

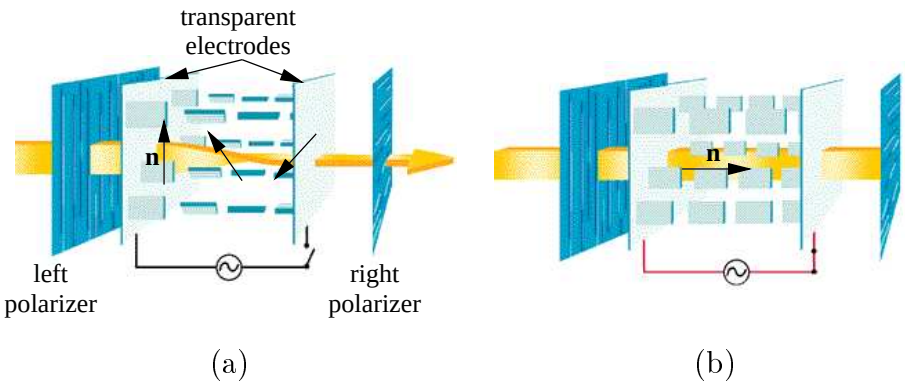

Figure 1.4: Illustration of a voltage-controlled light valve. (a) Without applied voltage, the twisted nematic liquid crystal between the electrodes turns the light by 90°. The cell is bright. (b) With applied voltage, the molecules orientent along the electic field. The light is filtered out by the right polarizer and the cell is dark.

transparent electrodes, which are arranged between two crossed polarizers. The electrode surfaces are treated such that a twist of 90° of the director **n** arises when no voltage is applied (Fig. 1.4 (a)). As the light traverses the cell the polarization is turned by 90°. Thus, light passes the right polarizer and the cell appears bright. Fig. 1.4 (b) illustrates the situation with an applied voltage. Now, the nematic director **n** aligns parallel to the electric field and the light traverses the liquid crystalline material unaffected. The light is filtered out by the right polarizer and the cell is dark. Beneath the usage

in display devices, liquid crystals are also applied in photonic applications as spatial light modulators [55] or as adaptive optical interconnects between printed circuit boards [103].

1.2 Model systems

A fundamental understanding of the mechanisms, which lead to liquid crystal formation is of general interest. In science, model systems are employed, in which relevant parameters can be identified and controlled precisely. In the following, we give a brief overview of experimental and theoretical models.

1.2.1 Lyotropic model systems

Systems of tobacco mosaic viruses (TMV) in solution are studied for more than 50 years as model systems for lyotropic liquid crystals. An electronmicrograph of TMV is presented in Fig. 1.5. The TMV combines two essential

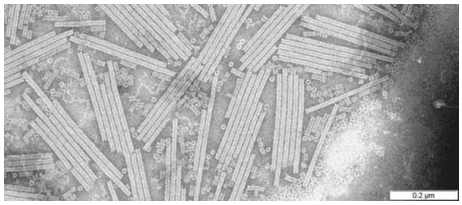

Figure 1.5: An electronmicrograph picture of TMV. The scale bar is $0.2\mu m$.

features - the particles are considerably stiff and rather monodisperse. Especially the latter property is often not fulfilled by chemically synthesized rods. In Fig. 1.6, we present two examples of liquid crystals formed by TMV. Part (a) depicts a sample with an isotropic phase in the upper and a nematic phase in the lower region. The picture shows the same sample twice. Two transparent liquids are observed under white light in the left half. In the right half the sample is viewed under crossed polarizers. The isotropic region is black whereas the nematic region appears bright. The smectic phase of TMV viewed under crossed polarizers is presented in Fig. 1.6 (b). The dark lines, which separate differently colored regions are disclinations.

Another model system consists of fd viruses in solution. Recent studies elucidated the kinetics of the isotropic-smectic transition in suspensions of fd viruses and non-adsorbing polymers [22]. The first step in the formation process of a smectic liquid crystal is depicted in Fig. 1.7 (a) where a nematic droplet can be seen. An interesting observation is the formation of a single layer in solution. The hexagonal shape of the layer in Fig. 1.7 (b) is a strong indication that long-range order exists within the layer [22].

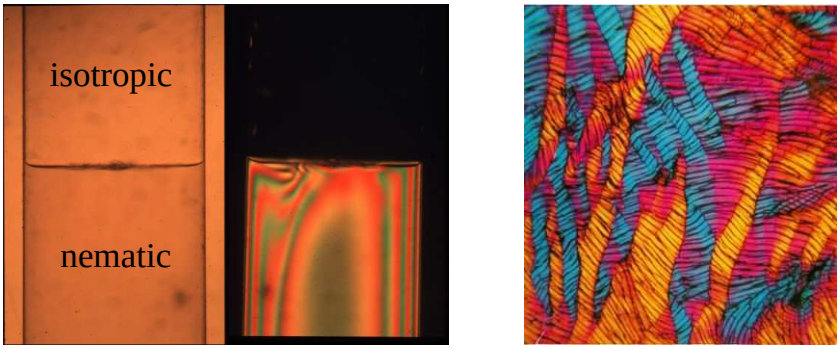

(a) (b)

Figure 1.6: Mesophases of TMV. (a) Isotropic-nematic coexistence viewed under white light (left half) and viewed under crossed polarizers (right half). The image is taken from the Fraden lab. (b) Smectic phase of dried TMV viewed under crossed polarizers [100].

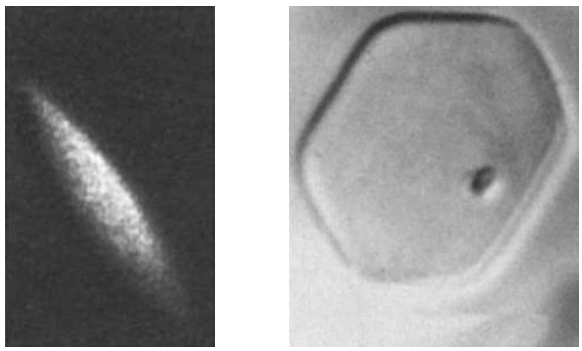

(a) (b)

Figure 1.7: Optical images in suspensions of fd virus and non-adsorbing polymers [22]. (a) In the first step of the isotropic-smectic transition a nematic droplet forms. The length of the droplet is about $6\mu m$. (b) Formation of a hexagonally shaped monolayer of fd viruses. The diameter of the monolayer is about $23\mu m$.

1.2.2 Theoretical models

The understanding of the physical principles that lead to long-range orientational order in rod systems was promoted fundamentally by Onsager's work in the 1940s [57]. He identified the interplay of orientational entropy and orientation-dependent excluded volume as sufficient driving force for the rods to align along a global director, i. e. for the formation of a nematic

phase. Each rod is considered as a spherocylinder of length L and diameter D and interactions are due to steric repulsion. The original work of Onsager only considered nematic order. With the help of density functional theory, smectic order can be treated analytically [14]. Because of the assumptions of Onsager's theory (steric repulsion, dilute system, $L \gg D$), the validity of the predictions are basically restricted to lyotropic rod systems. Long-range orientational order in thermotropic liquid crystals is resembled more appropriate in the Maier-Saupe theory [49]. Here, each rod is exposed to an average orienting field induced by its neighborhood whereas steric interactions are neglected. This approach is analogous to the explanation of the ferromagnetism by Weiss. Another approach is via the continuum theory developed by Oseen [59] and Frank [26], in which molecular details are neglected. This technique is used in many occasions where variations of the nematic director $\mathbf{n}$ occur on much larger length scales than the molecular dimensions. The continuum theory for nematic liquid crystals has been developed in the first half of the last century and is still a widely used tool [35, 43, 44, 86]. The development of computers provides an additional tool to study the collective behavior of many-particle systems - computer simulations. They establish the possibilities to use realistic interparticle interactions and to study the influence of confining walls. Computer simulations can also be adapted very flexible to new problems. The Monte Carlo (MC) and the molecular dynamics (MD) simulation technique represent the most widespread computer simulation techniques. In both cases, pair interactions have to be established.

Two model potentials are preferentially used to mimic rodlike particles. The first model – the Gay-Berne model – is an extension of the Lennard-Jones potential for uniaxial ellipsoids [28]. The potential is available in an analytical expression and forces and torques are obtained as derivatives of the potential. This feature is especially helpful in molecular dynamics simulations or for analytical calculations. The Gay-Berne potential is one of the few models, which appropriately takes into account the attractive interactions for rodlike molecules. The orientation of two rods with respect to each other is characterized by four scalars and an attractive pair interaction like the Gay-Berne potential takes care for this. The phase behavior of Gay-Berne mesogens has been studied extensively [4, 9, 18, 19, 92], also with incorporated quadrupoles [102], and in confining geometries [33, 34, 98]. The Gay-Berne model is typically employed to mimic thermotropic liquid crystals.

The second model consists of spherocylinders. A spherocylinder is composed of a cylinder of length L and diameter D, which is capped at both ends by hemispheres as illustrated in Fig. 1.8. The axis ratio $\lambda \equiv L/D$ characterizes a spherocylinder completely. Colloidal rods are typically cylindrically and in solutions of these rods short-range repulsive forces are often

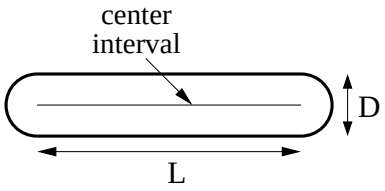

Figure 1.8: Schematic drawing of a spherocylinder with axis ratio $\lambda = L/D$.

predominant. Therefore, colloidal rods are frequently mimicked by hard spherocylinders, which take into account only hard core repulsions. The phase diagram of hard spherocylinders has been explored with the help of simulations [7, 91] and density functional theory [31] and is basically completely known [7] (Fig. 1.9). The first liquid crystalline phase, which sets in at grow-

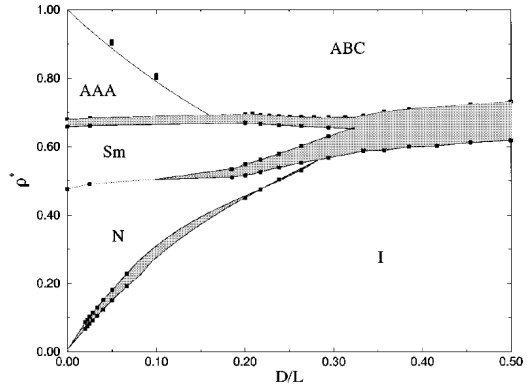

Figure 1.9: Phase diagram for hard spherocylinders [7]. The reduced density ρ^* is plotted along the ordinate and the inverse axis ratio D/L is plotted along the abscissa.

ing axis ratio $\lambda = L/D$ is the smectic phase ($\lambda \gtrsim 3.1$). At $\lambda \gtrsim 3.7$, a nematic phase exists at finite densities. For finite axis ratios, the isotropic-nematic phase transition is first order and occurs at finite density. In the limit of infinitely long cylinders ($D/L \to 0$), the isotropic-nematic transition shifts towards a vanishing density. At suitably high densities, solid phases with different layer stacking appear. Other aspects investigated with the hard rod model are, for example, the crystal nucleation in overcompressed fluids [73] or the isotropic-nematic interfacial tension [94].

In some cases, attractive interactions between colloidal rods cannot be neglected. For small colloidal rods, the van der Waals interaction becomes relevant. In the case of single walled carbon nanotubes (SWNTs), the van der Waals interaction is so strong that suitable dispersions of pure SWNTs have been achieved only recently [65]. In solutions of mesoscopic rods and polymers, attractive interactions are based on depletion forces [48, 52]. If a void between neighboring rods gets too small for the polymer coils to enter, the system favors a reduction of the gap in order to maximize the available

space for the polymers. Depletion forces between rods have been investigated for polymer stabilized fd viruses in polymer solutions [22].

Spherocylindrical rods with attractive interactions are discussed rather rarely in the literature. Often, the attractive contribution is considered strongly simplified, depending only on the shortest distance of the interacting rods [16, 50, 96]. In this work, we use an extension of a model potential by Bolhuis *et al.* [8], which depends on the rod distance as well as on the orientation of the interacting rods. Recently, Martinez-Haya *et al.* [51] proposed an attractive rod potential on the basis of the Gay-Berne potential with a spherocylindrical core. Both the potential used here and the potential from Martinez-Haya *et al.* incorporate the four scalars, which define the relative pair orientation of two rods.

1.3 Length polydisperse systems

Most systems of synthesized mesoscopic rods have a polydisperse length distribution. This is a consequence of the longitudinal growing process, which has no characteristic length scale. According to Gibbs' phase rule, the number of possible phases grows linearly with the number of constituents. Thus, polydispersity enriches the phase behavior. In the coexistence region of isotropic and nematic phases, the system gains spatial and orientational entropy if short rods are preferentially in the isotropic phase and long rods in the nematic phase. If this effect dominates the corresponding loss in mixing entropy, fractionation sets in. Bidisperse hard rod suspensions with only two constituents are widely studied. In these suspensions, a variety of new phenomena can be observed such as a widening of the biphasic isotropic-nematic (I-N) region, a triphasic I-N-N coexistence region, and strong fractionation of long and short rods [46]. The phase diagram beyond the nematic phase reveals columnar phases in systems of parallel spherocylinders [80]. Recent works also focused on smectic phases and report on a SmA-SmA phase transition and strong fractionation. Furhermore, the phases appear to depend on the length ratio of the components as well as on their axis ratio [14]. In binary mixtures of thick and thin hard rods, a depletion driven I-I demixing occurs [88]. In length tridisperse mixtures, nematic three-phase regions are found [97]. Length polydisperse hard rod systems with a continuous distribution have also been studied [15, 78]. In addition to the phenomena mentioned above, like a widening of the I-N coexistence region, the fractionation is found to depend distinctly on the polydispersity. A moderate fractionation is observed at a low polydispersity whereas the opposite is the case at high polydispersity [99]. Smectic phases become unstable at large polydispersity

whereas columnar phases become stable [3].

For many technical and research applications, a rather small polydispersity is desired in order to have precise material properties. Fractionation as a result of phase separation presents one possibility to establish a length specific sorting mechanism. In this work, we demonstrate with the help of Monte Carlo simulations how attractive interactions of the rods influence fractionation. We also point out, how suitably designed substrates can be exploit to generate highly monodisperse length distributions in preassigned regions, i. e. at the substrate. Various aspects of the influence of confining walls on monodisperse rod suspensions were already addressed in the past [21, 23, 62, 76, 79, 89]. The technical skills to design substrate patterns in the submicrometer regime are fast-paced comprising a variety of different techniques [29] like colloidal lithography [104] or lithographically induced self-assembly [13], thus delivering the opportunity to suitably tailor substrate structures.

1.4 Overview

This work is divided in three parts. The theoretical background is introduced in Chapter 2. After a brief overview of the statistical mechanics of polydisperse rod systems, the model potential for attractive rods is introduced. We demonstrate the potential dependence for various rod configurations. An effective method to calculate the attractive interaction is derived in Appendix A. The Monte Carlo simulation scheme in the isobaric-isothermal ensemble and also advanced simulation schemes like the biased multi-histogram sampling are introduced in Section 2.4. The last section of Chapter 2 covers the observables, which are employed to study the structure of the systems. We propose a rescaling of the nematic order parameter for finite particle numbers. The corresponding derivation is presented in Appendix C.

The results for bulk systems are presented in Chapter 3, which is divided in three sections dealing with monodisperse systems, a tridisperse suspension, and a polydisperse suspension. For all systems, the influence of attractive interactions is investigated. The attractivity changes the bulk behavior for monodisperse systems significantly as shown in the corresponding isotherms and phase diagrams. In tridisperse and polydisperse systems the focus lies on fractionation effects and structure formation.

The most extensive studies are performed for systems with adjacent substrates in Chapter 4. The suspensions investigated are tridisperse and polydisperse since we focus on fractionation effects. Three different substrate types are considered: A planar wall, a corrugated wall, and a wall with rect-

angular cavities. The substrates induce a broad spectrum of fluid structures depending on the applied pressure and the specific choice of the substrate pattern. We compare all patterns concerning their efficiency to control a length specific aggregation at the wall. The influence of attractive interactions is discussed in Section 4.1.6. The work finishes with a comprehensive summary of the results and an outlook in Chapter 5.

Chapter 2

Theoretical and technical framework

2.1 Statistical mechanics

We consider a system of N classical rodlike particles separated into $n_{\max}$ different components, which differ in certain properties, e. g. the mass or the length. Each component may have N_α particles:

$$N = \sum_{\alpha=1}^{n_{\max}} N_\alpha. \tag{2.1}$$

The internal energy $\mathcal{H}$ of the system has a kinetic ($\mathcal{K}$) and a potential ($\mathcal{U}$) contribution:

$$\mathcal{H} = \mathcal{K} + \mathcal{U} \tag{2.2}$$

$$= \sum_{i=1}^{N} t_i + \sum_{i=1}^{N-1} \sum_{j=i+1}^{N} v_{ij}, \tag{2.3}$$

where v_{ij} is a pairwise interaction between the particles i and j. The kinetic energy t_i of a single particle i has a contribution t_i^{trans} from the center of mass motion and a contribution t_i^{rot} from rotations. If $\mathbf{p}_i$ is the momentum of the center of mass and m_i the mass of particle i, then t_i^{trans} is given by

$$t_i^{\text{trans}} = \frac{\mathbf{p}_i^2}{2m_i}. \tag{2.4}$$

For simplicity we assume that the rodlike particles have a cylindrical symmetry and are elongated along the z-axis. In a body fixed coordinate system

the inertial tensor is diagonal, with

$$I_{i,1} = I_{i,2} \equiv I_i \tag{2.5}$$
$$I_{i,3} = 0. \tag{2.6}$$

If we call $(\dot{\Omega}_{i,1}, \dot{\Omega}_{i,2}, \dot{\Omega}_{i,3})$ the angular velocity with respect to the same reference frame, then the rotational part of the kinetic energy of particle i is given by

$$t_i^{\text{rot}} = \frac{I_i}{2}(\dot{\Omega}_{i,1}^2 + \dot{\Omega}_{i,2}^2) \tag{2.7}$$
$$= \frac{1}{2I_i}(p_{\Omega_i,1}^2 + p_{\Omega_i,2}^2), \tag{2.8}$$

where $p_{\Omega_i,k}$ is the conjugate momentum to the angle $\Omega_{i,k}$.

For the sake of simplicity, we first focus on a monodisperse system ($n_{\max} = 1$) at constant volume V and temperature $\beta = 1/kT$. The particles are located in a cubic box of dimension $\sqrt[3]{V}$. The partition function in the NVT ensemble then is

$$Z(N,V,T) = \frac{1}{N!\,h^{5N}} \int \left[\prod_{i=1}^{N} d^3\mathbf{p}_i\, d^3\mathbf{r}_i\, d^2\mathbf{p}_{\Omega_i}\, d^2\Omega_i\right] \times \exp\left[-\beta\left(\sum_j t_j^{\text{trans}} + \sum_j t_j^{\text{rot}} + \sum_{j<k} v_{jk}\right)\right]. \tag{2.9}$$

The integration over the momenta $\mathbf{p}_i$ is carried out easily. All integrals are of the same type $\int dx \exp(-ax^2) = \sqrt{\pi/a}$. The same holds for $\mathbf{p}_{\Omega_i}$. Furthermore, reduced units $\mathbf{s}_i \equiv \mathbf{r}_i/L$ are introduced. All in all, the partition function simplifies to

$$Z(N,V,T) = \frac{V^N}{N!\,\Lambda^{3N}\tau^{2N}} \int \left[\prod_{i=1}^{N} d^3\mathbf{s}_i\, d^2\Omega_i\right] \exp(-\beta \sum_{j<k} v_{jk}), \tag{2.10}$$

where $\Lambda = h/\sqrt{2\pi mkT}$ is the de Broglie wave length of a point mass. The corresponding analogon for cylindrical particles is $\tau = h/\sqrt{2\pi IkT}$.

Now we turn to the slightly more complex partition function at constant pressure P with $n_{\max} \geq 1$ components. The partition function in the NPT

ensemble is denoted $Q(N,P,T)$ [27]:

$$Q(N,P,T) = \beta P \left[\prod_{\alpha=1}^{n_{\max}} \frac{1}{N_\alpha!\,\Lambda_\alpha^{3N_\alpha}\tau_\alpha^{2N_\alpha}}\right] \int dV\, V^N \exp(-\beta PV) \times \int \left[\prod_{i=1}^{N} d^3\mathbf{s}_i\, d^2\Omega_i\right] \exp(-\beta \sum_{j<k} v_{jk}). \tag{2.11}$$

Once the partition function is known, all thermodynamic properties of the system can be deduced. The Gibbs free energy $G(N,P,T)$, for example, is related to $Q(N,P,T)$ through

$$G(N,P,T) = -kT \ln Q(N,P,T) \tag{2.12}$$

and all other thermodynamic quantities are derivatives of G. However, the integrals in Eq. (2.11) can only be solved in extremely idealized systems and thus the partition function is typically unknown.

2.2 The model

Colloidal particles in solution usually differ by a few orders of magnitude in size from the solvent molecules. For example a water molecule has a diameter of ~ 2.8Å whereas the dimensions of colloids range from several nanometers to a few micrometers. The explicit consideration of the solvent molecules turns investigations of the collective behavior of colloidal particles into an extremely challenging task. A broad range of problems, however, can be tackled by an implicit consideration of the solvent. Effective pair potentials between the colloids can be utilized, which on the one hand comprise the solvent independent colloidal interactions like van der Waals forces and on the other hand solvent induced interactions like depletion forces [6, 58].

The origin of the depletion forces is illustrated in Fig. 2.1 for two impenetrable spherical colloids. We assume that the colloids are in solution with non-adsorbing polymers and interact purely repulsively. Each polymer can be approximated by a sphere with radius equal to the radius of gyration, R_g. Since the polymer and the colloid cannot overlap, the centers of mass of the polymer coils are prevented from entering a shell of thickness R_g around the colloid. Fig. 2.1 (a) depicts the two colloids at large separation. The excluded volume for the polymers is the sum of both parts. The total excluded volume does not change until the surfaces of both colloids come closer than $2R_g$. In this case, the total excluded volume will decrease by the amount

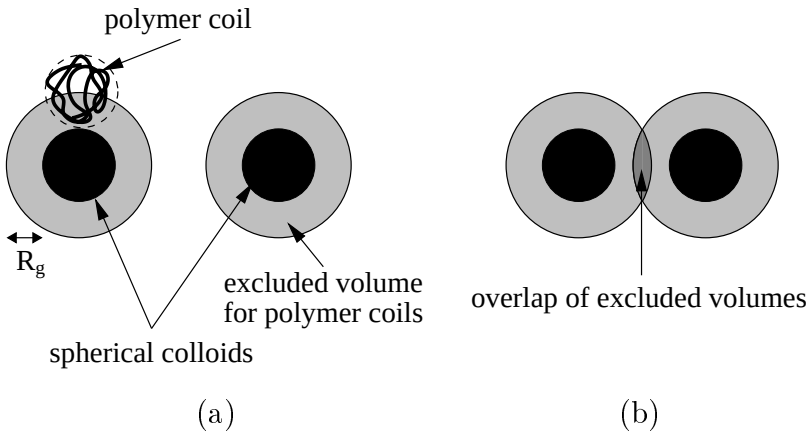

Figure 2.1: Illustration of depletion forces for spherical colloids. Around each sphere, the polymers cannot access a shell of width R_g around the colloid. (a) The excluded volumes do not overlap at large separation. (b) The overlap of excluded volumes gives rise to attractive interactions.

of overlap of excluded volumes as indicated in Fig. 2.1 (b). As a result, the two colloids feel an effective attractive interaction, since the polymers can increase their accessible volume by an increase of the overlap volume. Fig. 2.2 shows cartoons for rodlike colloids. The hard rod model is sketched in part

Figure 2.2: (a) Schematic sketch of the hard rod model. The hard core of the rods forbids overlaps. (b) Attractive depletion interactions are present if the green regions overlap. (c) The pair potential is minimal (=maximal attraction) when the rods are parallel and the hard cores touch.

(a) with an impenetrable core region. Depletion forces between two rods are illustrated in Fig. 2.2 (b) and (c). The green color represents the excluded volume. The overlap of the excluded volume is maximal when the two rods are parallel and their hard cores touch.

The phase behavior of spherical colloids has been successfully described with the help of hard sphere and spherical square-well potentials. The latter consists of a hard sphere part U^h that takes into account for hard core repulsions and an attractive part for short-range attraction. For two spherical colloids of distance r we have

$$U^{\mathrm{sw}}(r) = U^h(r) + U^a(r) \tag{2.13}$$

with

$$U^h(r) = \begin{cases} \infty & \text{, if } r < D \\ 0 & \text{, otherwise} \end{cases} \tag{2.14}$$

$$U^a(r) = \begin{cases} -\epsilon & \text{, if } r \leq D_a \\ 0 & \text{, otherwise} \end{cases}, \tag{2.15}$$

where $\epsilon > 0$ is the potential depth, D is the hard core range, and $D_a > D$ is the range of the attractive potential.

Now we consider two spherocylindrical colloids i and j with lengths L_i and L_j. A spherocylinder consists of a cylinder of diameter D and length L, which is capped by two hemispheres at both ends. The repulsive part of the interaction is obtained by integrating U^h for all pairs of points on the two cylinder axes

$$U_r^h = D^{-2} \int_{-L_i/2}^{L_i/2} \mathrm{d}\alpha_i \int_{-L_j/2}^{L_j/2} \mathrm{d}\alpha_j U^h \left(|\mathbf{r}_{ij} + \alpha_j \mathbf{u}_j - \alpha_i \mathbf{u}_i| \right). \tag{2.16}$$

The directions of the cylinders are $\mathbf{u}_i$ and $\mathbf{u}_j$. $\mathbf{r}_{ij}$ connects both centers of mass. Note that the hard cores of rods i and j have a total length $L_i + D$ and $L_j + D$, respectively. In analogy, the attractive part of the rod interaction is defined as

$$U_r^a = D^{-2} \int_{-L_i/2}^{L_i/2} \mathrm{d}\alpha_i \int_{-L_j/2}^{L_j/2} \mathrm{d}\alpha_j U^a \left(|\mathbf{r}_{ij} + \alpha_j \mathbf{u}_j - \alpha_i \mathbf{u}_i| \right). \tag{2.17}$$

The sum of both parts gives the attractive rod (AR) potential

$$U_{\mathrm{AR}} = U_r^h + U_r^a, \tag{2.18}$$

which has a spherocylindrical hard core and an attractive interaction when the surfaces of the rods come closer together than $D_a - D$. For equal cylinder lengths $L_i = L_j$ the AR potential corresponds to the potential described and investigated by Bolhuis *et al.* [8].

The properties of U_{AR} are demonstrated in Figs. 2.3 and 2.4 for different geometries of two rods with various lengths, where we chose $\epsilon = 1kT$ and

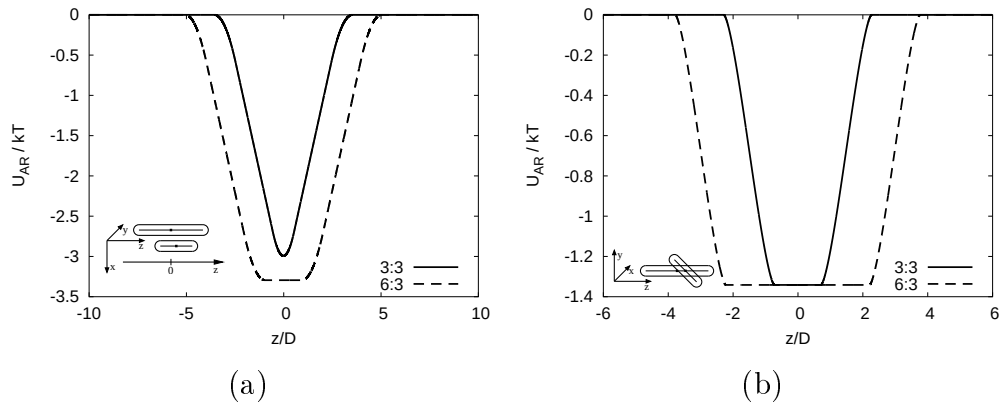

Figure 2.3: Attractive rod (AR) potential U_{AR} for two rods i and j with diameter D. Rod i is located at the origin and is oriented parallel with the z-axis. The center of mass of rod j is located at $(x, 0, z)$ with $x = 1.01D$. The AR potential is shown as a function of z/D for rod j having an axis ratio $\lambda_j = 3$ and rod i with axis ratios $\lambda_i = 3$ (—) and $\lambda_i = 6$ (– – –). In (a), the cylinder axis of rod j is oriented parallel to that of rod i, in (b), it is rotated by an angle of $\pi/4$ within the yz-plane.

$D_a = 1.15D$. The plots show that the size of U_{AR} depends on the shortest distance between the rods as well as on their alignment. More specifically, it depends on the amount of surface area of rod i sufficiently close to the surface of rod j. Furthermore, it is noteworthy that U_{AR}, though defined via a step function, goes to zero continuously. The strongest pair interaction energy $E_{\min} < 0$ occurs for parallel, perfectly aligned rods at a distance D, which corresponds to the conditions

$$\begin{aligned} \mathbf{u}_i \cdot \mathbf{u}_j &= 1, \\ \mathbf{r}_{ij} \cdot \mathbf{u}_i &= \mathbf{r}_{ij} \cdot \mathbf{u}_j = 0, \\ \|\mathbf{r}_{ij}\| &= D. \end{aligned}$$

For not too small rods, obeying $L_i \geq L_j \geq \sqrt{D_a^2 - D^2}$, integration of Eq. (2.17) yields

$$\begin{aligned} E_{\min} = -\frac{\epsilon}{D^2}\Bigg[& 2L_j\sqrt{D_a^2 - D^2} - \\ & - \frac{1}{4}\Big(L_i - L_j - \max[2\sqrt{D_a^2 - D^2}, L_i - L_j]\Big)^2\Bigg]. \end{aligned} \tag{2.19}$$

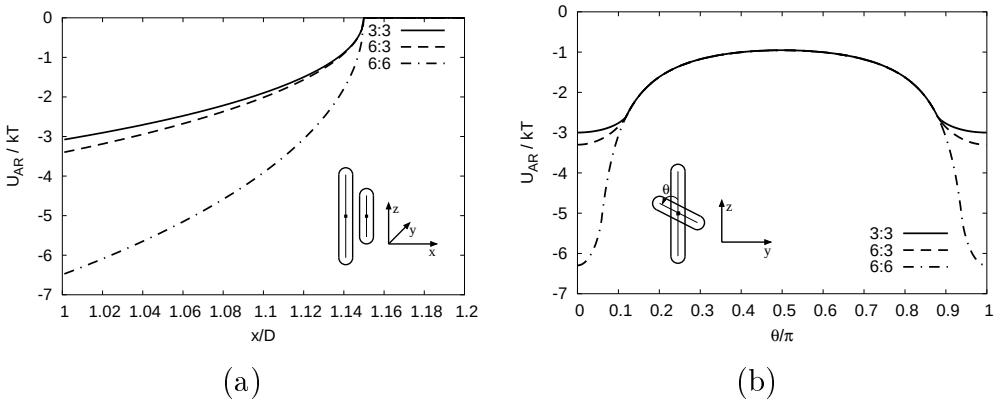

Figure 2.4: Attractive rod potential U_{AR} for two rods i and j with diameter D. Rod i is located at the origin and has a cylinder axis parallel to the z-axis. The center of mass of rod j is located at $(x, 0, 0)$. Results are shown for rod axis ratios $(\lambda_i, \lambda_j) = (3,3)$ (—), $(6,3)$ (– – –), and $(6,6)$ (–·–·–). In (a), the rods are parallel and U_{AR} is shown as a function of x. For $x < 1$ the hard cores overlap and U_{AR} becomes infinite. In (b), $x = 1.01D$ and U_{AR} is shown as a function of the angle θ between the rod axes.

The most CPU time consuming part of U_{AR} is the attractive interaction. For the hard core repulsion it is sufficient to check whether the shortest distance between the two cylinder axes is smaller than D. A method to calculate the integral in Eq. (2.17) is described in the appendix A.

2.3 The Monte Carlo method

Monte Carlo (MC) and molecular dynamics (MD) simulations are the most prominent types of computer experiments to investigate the behavior and the properties of fluids. In MD simulations, the equations of motion are integrated numerically. Macroscopic observables such as pressure, internal energy, and correlation functions are obtained as time averages. During a MC simulation, many independent configurations of the system under consideration are generated and utilized to gain thermal averages. In this work, Monte Carlo techniques are used exclusively.

2.3.1 Theoretical background

Suppose A is a quantity, which depends only on the microscopic variables $\mathbf{r}_i$ and $(\Omega_{i,1}, \Omega_{i,2})$ but not on the momenta[1]. For convenience, Γ is introduced as abbreviation for a point in configurational state space and $d\Gamma \sim dV \prod d^3 s_i d^2\Omega_i$. The thermal average $\langle\cdot\rangle$ is then computed in the standard way

$$\langle A \rangle = \frac{\int d\Gamma \, P_B(\Gamma) \, A(\Gamma)}{\mathcal{Q}} \tag{2.20}$$

with

$$P_B(\Gamma) \equiv V^N \, \exp[-\beta(\mathcal{U}(\Gamma) + PV)] \tag{2.21}$$

and

$$\mathcal{Q} \equiv \int d\Gamma \, V^N \, \exp[-\beta(\mathcal{U}(\Gamma) + PV)]. \tag{2.22}$$

Note the difference between Q as defined in Eq. (2.11) and the $\mathcal{Q}$ defined here.

Suppose we are able to generate M random configurations $\Gamma^{(i)}$ ($i = 1, .., M$) of the system according to P_B in the computer. The average in Eq. (2.20) is then approximately given by

$$\langle A \rangle \approx \frac{1}{M} \sum_{i=1}^{M} A(\Gamma^{(i)}). \tag{2.23}$$

Metropolis *et al.* [54] developed a scheme, which creates a Markov chain of configurations that are distributed corresponding to P_B. To understand their method we assume the following [27]: Let $\Gamma^{(i)}$ be the initial state of the system. We might have certain mechanisms to generate a new state $\Gamma^{(j)}$, e. g. by moving and/or rotating particles. The probability, with which $\Gamma^{(j)}$ is proposed may be called $p_{\text{try}}^{(ij)}$. It is important to note that not every proposed configuration will also be accepted. The acceptance probability $p_{\text{acc}}^{(ij)}$ will be specified later. In this manner, from the point $\Gamma^{(i)}$ a set of new states $\{\Gamma^{(j)}\}^{(i)}$ can be accessed. It is intuitively clear that in thermal equilibrium the probability to leave state $\Gamma^{(i)}$ must be equal to the probability to reach state $\Gamma^{(i)}$ from the set $\{\Gamma^{(j)}\}^{(i)}$. Otherwise some probability flux would occur, which is not possible in thermal equilibrium. In practice one imposes an even stronger condition called *detailed balance*, which demands the equality of in- and out-going probabilities for any two states $\Gamma^{(i)}$ and $\Gamma^{(j)}$:

$$P_B(\Gamma^{(i)}) \, p_{\text{try}}^{(ij)} \, p_{\text{acc}}^{(ij)} = P_B(\Gamma^{(j)}) \, p_{\text{try}}^{(ji)} \, p_{\text{acc}}^{(ji)}. \tag{2.24}$$

[1] Usage of the $\mathbf{r}_i$ implies also a dependence on the volume V.

It is not a prerequisite but in many situations it appears that the generating mechanism leads to a symmetric matrix $p_{\text{try}}^{(ij)} = p_{\text{try}}^{(ji)}$. In these cases the detailed balance condition (2.24) simplifies to

$$\frac{p_{\text{acc}}^{(ij)}}{p_{\text{acc}}^{(ji)}} = \frac{P_B(\Gamma^{(j)})}{P_B(\Gamma^{(i)})}. \tag{2.25}$$

The actual acceptance probability $p_{\text{acc}}^{(ij)}$ is not fixed by Eq. (2.25) but a common choice is

$$p_{\text{acc}}^{(ij)} = \min\left[1, \frac{P_B(\Gamma^{(j)})}{P_B(\Gamma^{(i)})}\right]. \tag{2.26}$$

The big advantage of this method stems from the fact that no a priori knowledge of the distribution function of microstates, i.e. the partition function is required. It is sufficient to know the Boltzmann factor, which, in general, is given. For some investigations it is desirable to generate Markov chains with other distribution functions than P_B. Section 2.4.1 will deal with these problems.

2.3.2 The Monte Carlo algorithm

We have applied the MC scheme, described in the last section, to a system of rods. For this system, the following trial moves were performed in random order: Moving a rod, rotating a rod, a combination of movement and rotation, and volume changes. During simulations of length-polydisperse mixtures, length changes were allowed to speed up equilibration.

Suppose rod i, whose center of mass is originally located at $\mathbf{r}_i^{(o)}$, is chosen to be moved. The configurational energy of the system in the old state is called $\mathcal{U}^{(o)}$. In a first step, a new position $\mathbf{r}_i^{(n)} = \mathbf{r}_i^{(o)} + \Delta\mathbf{r}$ is proposed where $\Delta\mathbf{r}$ is a random displacement vector whose components are uniformly distributed over an interval $[-\delta_m, \delta_m]$. The new position of particle i leads to a change $\Delta\mathcal{U} = \mathcal{U}^{(n)} - \mathcal{U}^{(o)}$ of the configurational energy. In the next step a decision is made whether the new position is accepted or not. For this purpose, the Metropolis criterion (Eq. (2.26)) is used:

$$p_{\text{acc}} = \min\left[1, \exp(-\beta\Delta\mathcal{U})\right]. \tag{2.27}$$

The new position is accepted immediately if $\Delta\mathcal{U} \leq 0$, which avoids to compute the Boltzmann factor $\exp(-\beta\Delta\mathcal{U})$. Otherwise a random number is generated in the interval $[0; 1)$. The new position is accepted if the random number is smaller than the Boltzmann factor. Regardless of whether the move is accepted or not, the final configuration has to be included into the Markov chain.

For the rotation of a rod, a random unit vector is generated. This vector defines the rotation axis, around which the director is rotated by a random angle $\Delta\vartheta\,\epsilon\,[-\delta_r, \delta_r]$. The further proceeding is equivalent to the particle movement. The sequence of single particle Monte Carlo steps is chosen entirely at random. This means that for a random particle we decide randomly whether it is moved, rotated, or moved and rotated.

MC simulations in the NPT ensemble require also a fluctuating volume. It has turned out that a random walk in $\ln V$ supports fast equilibration [24]. The old volume $V^{(o)}$ is rescaled according to $\ln V^{(n)} = \ln V^{(o)} + \Delta(\ln V)$. The new particle positions become $\mathbf{r}_i^{(n)} = \mathbf{r}_i^{(o)} \exp(\Delta(\ln V)/3)$ with $\Delta(\ln V) \in [-\delta_V, \delta_V]$. Note that this procedure correlates the three box dimensions L_x, L_y, and L_z. This may cause problems in the equilibration of rod configurations with long-range positional order such as smectic phases. In these cases L_x, L_y, and L_z were allowed to fluctuate independently. The generalization is straightforward. The logarithmic sampling leads to an additional factor of V in the partition function because $\int dV = \int d(\ln V)\, V$. The acceptance rule according to the Metropolis criterion for a volume move becomes

$$p_{\text{acc}} = \min\left[1, \exp\left(-\beta[\Delta\mathcal{U} + P\Delta V - (N+1)\,kT \ln(V^{(n)}/V^{(o)})]\right)\right] \quad (2.28)$$

with $\Delta V = V^{(n)} - V^{(o)}$. A volume move requires a recalculation of all pair interactions and is therefore computationally expensive. In the simulations, a volume move is attempted after one sweep ($= N$ single particle updates). The interval widths δ_m, δ_r, and δ_V are adjusted such that about 50% of the trial moves are accepted.

Saving CPU time A standard way to increase the speed of simulation programs is the usage of neighbor lists. There is no need to compute the pair potential of two rods if their shortest distance is larger than the cut-off radius D_a. A Verlet list keeps track of all particles, which are within a certain range – the Verlet radius r_V. For spherical particles it is obvious to search neighbors within a spherical volume. For a rod of length L_i, neighboring rods of length L_j are sampled within a sphere of radius $r_{V,sp} = (L_i + L_j)/2 + D_a + \sigma_{sp}$. The neighbor list has to be updated every time a particle has moved further than $\sigma_{sp}/2$. Especially in dense phases, such a spherical list locates many neighbors whose surface-to-surface distances are much larger than the interaction width (cmp. Fig. 2.5). Since the computation of the attractive rod potential U_{AR} is quite expensive a second spherocylindrical Verlet list is embedded in the spherical list, which reduces the number of neighbors drastically. This list keeps track of all rods whose center intervals have a shortest distance smaller than $r_{V,sc} = D_a + \sigma_{sc}$. The second list must be updated every time an end

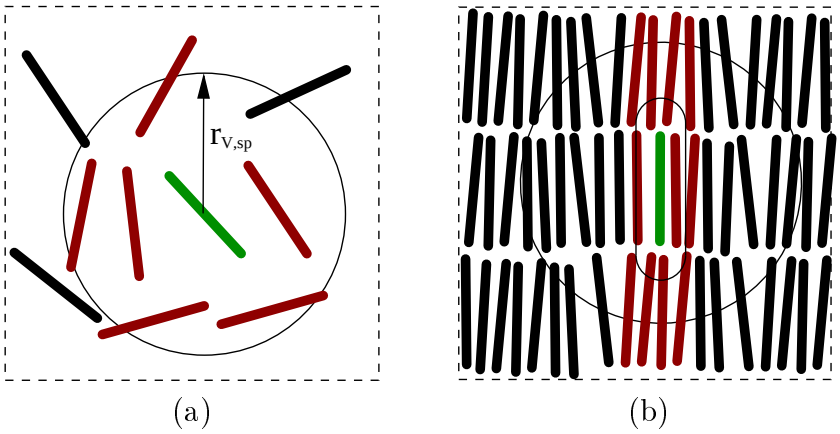

Figure 2.5: (a) Illustration of a spherical Verlet list. All red rods are within the spherical Verlet list of radius $r_{V,sp}$ of the the green rod. (b) Illustration of a spherocylindrical Verlet list embedded in a spherical Verlet list. In dense phases many rods are within the spherical volume. The number of neighbors reduces remarkably in the spherocylindrical volume. Neighbors are colored red, again.

point of the center interval has moved further than $\sigma_{sc}/2$. Particularly rod rotations lead to frequent updates of the spherocylindrical list. However, for an update of the second list only rods of the first list have to be considered so that over all the second list saves up to 50% of CPU time in dense phases. Furthermore, all pair interactions are stored and reused to compute the old interaction energy $\mathcal{U}^{(o)}$.

Random numbers The 'heart' of all Monte Carlo simulations is the random number generator. Strictly speaking, a computer cannot produce numbers by chance. In practice an algorithm generates a (reproducible) sequence of numbers, which should be as uncorrelated as possible. A suitably uncorrelated sequence of random numbers is required for a correct Markov chain. This requirement, however, is not fulfilled by all algorithms [75] [90]. In the beginning we used the widely accepted random number generator RAN3 [64]. Investigations of confined geometries, however, led to some unphysical observations, which could be attributed to correlations in RAN3 (see Appendix B). These problems did not occur with the random number generator MT19937 [53], which we therefore used to obtain correct results.

2.4 Advanced Monte Carlo techniques

The Monte Carlo scheme described in Section 2.3 produces a Markov chain with the stationary distribution $P_B/\mathcal{Q}$. The vast majority of samples used to compute the average in Eq. (2.23) are generated where P_B is maximal. In some cases a different sampling is reasonable. If an observable A is large in a region where P_B is small, only few samples are generated in this region giving rise to large statistical uncertainties of the average. For most observables, however, this effect is of minor relevance: On the one hand many observables are sufficiently smooth and on the other hand P_B is decreasing exponentially so that the product of A and P_B is small where P_B is small. Another problem might occur if P_B has several maxima (see Fig. 2.6). The system can be

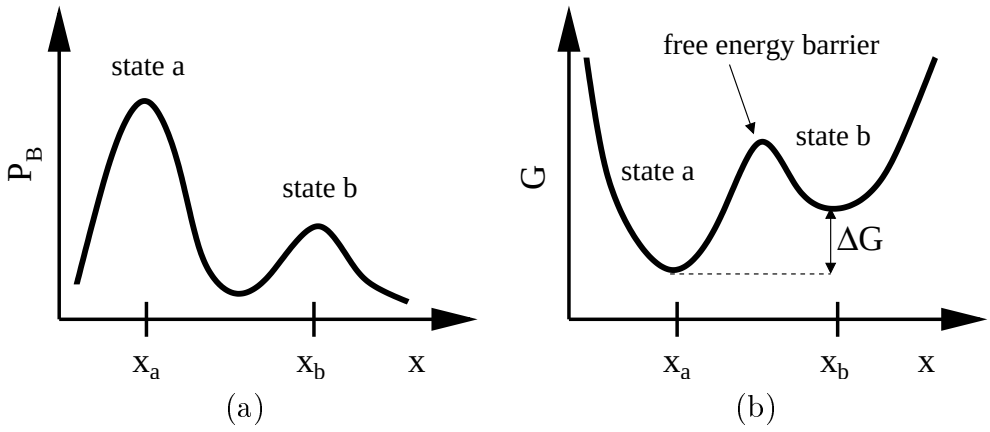

Figure 2.6: (a) Schematic drawing of a probability distribution P_B as function of a suitable parameter x. P_B has two maxima and state a is thermodynamically stable. A system, which is sampled around x_b, may take very long to traverse the minimum in P_B in order to find the global maximum at x_a. (b) The corresponding free energy landscape as function of x. Maxima of P_B turn into minima of G. The two minima differ by an amount of ΔG in free energy. Thermal fluctuations may not be large enough to cross the free energy barrier within a reasonable amount of time.

trapped in one region and it may take extremely long until it reaches the other minimum. Systems close to strong first order phase transitions are typical examples. The corresponding free energy landscape has two or more minima all separated by energy barriers that can in many cases not be overcome by thermal fluctuations. For the same reason, real systems show hysteresis.

Free energy barriers complicate not only the analysis of first order phase transitions. Investigations of protein folding, for example, have to deal with

complex free energy landscapes, as well. Thus, crossing free energy barriers and measuring free energy differences of two states (phases, conformations) is of widespread interest. In the past, several simulation techniques [5, 38, 85, 101] have been developed to tackle these problems. In this work, biased multi-histogram sampling is employed to drive a system smoothly from one local minimum of the free energy to another one and to estimate the free energy difference ΔG between both minima. Section 2.4.1 is dedicated to biased multi-histogram sampling. The phase coexistence is characterized by $\Delta G = 0$. Gibbs ensemble simulations [60, 61, 70] can be employed to investigate phase equilibria directly. The applicability of this method, however, is strongly restrained in dense systems and is thus not appropriate for our systems.

2.4.1 Biased multi-histogram sampling

Suppose the external control parameters N, P, and T are chosen such that the free energy landscape has one global and one local minimum. In this case, importance sampling according to P_B may be unsuitable for exploring the relevant configurational phase space. Consider a solid state at low temperature. Below the freezing temperature, the system has an absolute minimum for the crystalline state at a high density and typically a local minimum for the fluid state of lower density. Typical free energy curves during melting are depicted in Fig. 2.7. Both states, the high and low density state, are

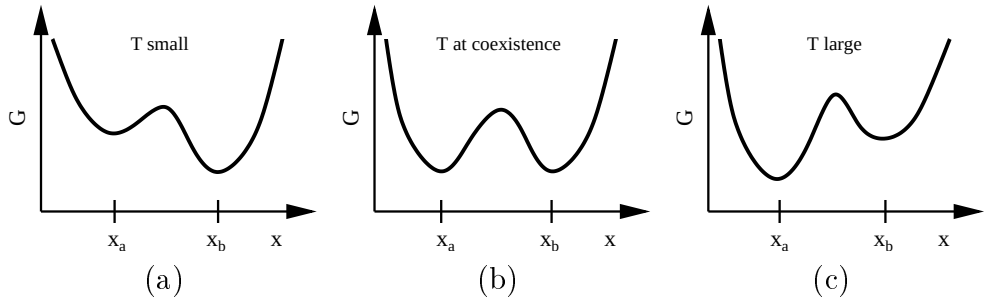

Figure 2.7: Schematic drawings of the free energy at different temperatures. The abscissa may represent the density, for example. The global minimum in (a) turns into a local minimum as the temperature is increased. In (b), the two phases are in coexistence.

separated by a system dependent energy barrier. In coexistence, the energy barrier represents the surface energy of the two adjacent phases. This energy

barrier leads to a more or less pronounced shift of the actual melting temperature from the coexistence temperature. For this reason, situations occur, in which the system is still in the high density state whereas the low density state is thermodynamically stable. If the energy barrier is much larger than thermal fluctuations, the system is trapped in the high density state when sampled according to P_B. Corresponding hysteresis effects occur also with an isotropic starting configuration. As a consequence, the average of an observable measured during the simulation depends on the initial condition and does not reach the thermodynamically stable phase. The simulation scheme explained in the following is appropriate to solve this problem.

A crucial point for the multi-histogram method is the definition of a suitable reaction coordinate or order parameter. On the one hand the reaction coordinate must distinguish between both phases. On the other hand a 'good' reaction coordinate should not hamper potential transient states by restricting the system to a narrow path through the free energy landscape. Examples of reaction coordinates are the density for fluids, the magnetization for ferromagnets, the amount of alignment for liquid crystals [94], or the size of a nucleus [2, 73]. The interaction energy per rod is a good candidate in the case of attractive rods since it varies significantly between the isotropic, smectic, and hexatic phase. The phase boundaries of the monodisperse rod systems in section 3.1 are determined by the use of this reaction coordinate. In principle, the free energy G as a function of the reaction coordinate x is obtained from the probability distribution

$$p(x) \equiv \frac{1}{\mathcal{Q}} \int d\Gamma \, P_B(\Gamma) \, \delta(\tilde{x}(\Gamma) - x) \tag{2.29}$$

$$= \langle \delta(\tilde{x} - x) \rangle \tag{2.30}$$

as

$$G(x) = -kT \, \ln\left(p(x)\right). \tag{2.31}$$

It has already been pointed out that free energy barriers may hamper the system in exploring the relevant regions of the reaction coordinate.

Assume a situation similar to the one depicted in Fig. 2.6 (b) with the system in the highly ordered phase[2] ($x = x_b$). The quantity of interest is the free energy difference $\Delta G = G(x_b) - G(x_a)$. The barrier region can be explored with the multi-histogram technique. In this method the free energy landscape is changed artifically for a set of supporting points $\{x_i\}$ between x_a and x_b. At each supporting point, a system is simulated, which differs

[2]Starting from high order is usually superior to the other way round since order is destroyed more easily than created.

from the original one by a bias potential $\mathcal{H}_i^b(x) \equiv \mathcal{H}_i^b$. The bias potential is constructed such that a minimum of the free energy arises in the vicinity of x_i. The sampling of each system is now performed according to the distribution $P_B\, W_i$, where

$$W_i = \exp(-\beta\, \mathcal{H}_i^b). \tag{2.32}$$

For the bias potential, a quadratic term like

$$\mathcal{H}_i^b(x) = \frac{\kappa}{2}\,(x - x_i)^2 \tag{2.33}$$

is suitable in most cases. For sufficiently large κ, the additional contribution $\mathcal{H}_i^b$ of the type (2.33) generates a minimum in the free energy close to x_i. The width of the window, to which the system is restricted, is regulated by the curvature κ. The resulting free energy is schematically drawn in Fig. 2.8. As a consequence a system with Hamiltonian $\mathcal{H}_i = \mathcal{H} + \mathcal{H}_i^b$ will explore a

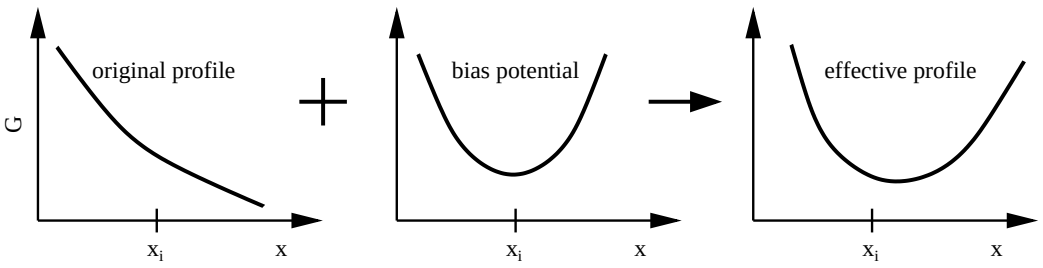

Figure 2.8: Schematic drawing of the free energy G as function of the reaction coordinate x. According to the original profile points close to x_i are visited rarely. The additional bias potential generates a minimum in the vicinity of x_i.

finite region around x_i.

The objective of the restriction to a small window region is to measure the probability distributions $p_i(x)$ (Eq. 2.29) in every window and to connect the corresponding free energy sections. In this manner, the free energy profile between x_a and x_b is constructed piecewise. The statistical accuracy is improved if neighboring windows overlap. In some occasions, much larger separations are either adequate or inevitable [47]. With the assumption that $G(x)$ is sufficiently smooth the first derivative can be utilized to construct the profile.

The stationary distribution of the Markov chain in window i is proportional to $P_B\, W_i$. The corresponding normalization factor, i. e. the partition function, is called $\mathcal{Q}_i \equiv \int d\Gamma\, P_B\, W_i$. An average according to the modified sampling distribution is denoted by $\langle\cdot\rangle_{P_B W_i}$. The probability distribution in

window i is thus given by

$$p_i(x) = \frac{\mathcal{Q}_i}{\mathcal{Q}} \frac{\langle \delta(\tilde{x} - x) \rangle_{P_B W_i}}{W_i(x)}. \tag{2.34}$$

From Eq. (2.34), the free energy in window i is calculated via $-kT \ln(p_i)$. Once the free energy around all supporting points x_i is known the complete profile can be constructed. The normalization factors $\mathcal{Q}_i$ are not measured explicitely but result from the vertical adjustments of the free energy parts such that a smooth function in x is obtained. The free energy difference between the two states a and b is thus

$$\Delta G = -kT \ln \frac{\mathcal{Q}_b}{\mathcal{Q}_a}. \tag{2.35}$$

In practice, $p_i(x)$ is measured in bins of finite width δ. Thus, $p_i(x)$ is a histogram, which keeps track of the amount of generated configurations with an order parameter in the interval $x \pm \delta/2$. Therefore, the name biased multi-histogram method.

2.4.2 Simulation of adjacent substrates

In Chapter 4, polydisperse rod systems with adjacent substrates are investigated. In the simulations, only one substrate at $-z_0$ and a 'half' system in the range $-z_0 < z < 0$ is explicitly considered. The 'half' system is mirrored at the $z = 0$ plane and shifted diagonally so that each rod with a center of mass (x, y, z) and an orientation vector (u_x, u_y, u_z) creates an image rod with a center of mass $(x + L_x/2, y + L_y/2, -z)$ and an orientation vector $(u_x, u_y, -u_z)$ as sketched in Fig. 2.9. In the original and the mirror region, periodic boundary conditions are applied in x- and y-direction. One must note, however, that the mirroring technique is restricted to systems, which are isotropic or axially symmetric to the z axis in the region close to $z = 0$. This is the case for all systems investigated with this technique.

The mirroring method has two advantages: Firstly, larger substrate separations can be investigated with a reasonable effort (Fig. 2.10). Wall separations of $2z_0 > 40D$ can easily be achieved. Secondly, since there is de facto only one substrate, the method avoids long-living metastable states, in which the rods are not distributed equally between the opposing substrates.

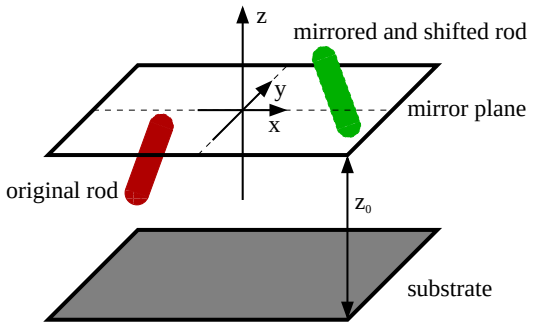

Figure 2.9: Visualization of the boundary conditions at the xy-plane in simulations of substrates. The original rod (red) is mirrored at the xy-plane and shifted diagonally resulting as the green rod.

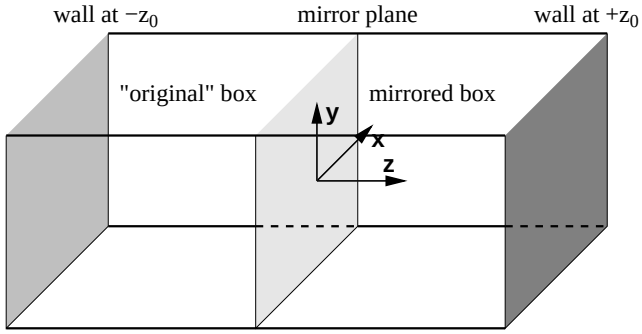

Figure 2.10: Illustration of the "original" and the mirrored simulation box. The effective wall separation is $2z_0$. Note that the z-axes points towards right.

2.5 Observables

2.5.1 The nematic order parameter

Orientational order is measured in terms of the nematic order parameter

$$S(N) = \langle \frac{1}{N} \sum_{i=1}^{N} P_2(\mathbf{u}_i \cdot \mathbf{n}) \rangle = \langle \lambda_{\max} \rangle, \tag{2.36}$$

where $P_2(\cdot)$ is the second Legendre polynomial and the average director $\mathbf{n}$ is the eigenvector of the largest eigenvalue $\lambda_{\max}$ of the alignment tensor

$$Q_{\mu\nu} = \frac{1}{2N} \sum_{i=1}^{N} (3u_{i,\mu}u_{i,\nu} - \delta_{\mu\nu}). \tag{2.37}$$

For a perfectly aligned system of rods, one has $S = 1$. In an infinitely large isotropic system, one has $S = 0$. For finite systems, however, $S(N)$ depends on the number of rods N. Especially for small isotropic systems, $S(N)$ is typically larger than 0 and shows a strong system-size dependence. To overcome this problem, Eppenga and Frenkel [24] suggested to replace $S(N)$ by

$$S_\infty \equiv \lim_{N\to\infty} S(N), \tag{2.38}$$

the order parameter of a corresponding infinite system. A method for calculating S_∞ is given in Appendix C.

The orientational order parameter S_∞ is independent of the considered number of rods. This is particularly helpful when measuring the orientational order of small subsets of rods in a system. It allows the determination of the orientational order for every component of a polydisperse suspension, in which certain rod lengths are present only in small amounts. Another useful application of S_∞ is the calculation of the local orientational order in a small subvolume of the simulation box. One typical example is the orientational order as a function of the distance from a substrate [98].

2.5.2 Pair correlation functions

Pair correlation functions reveal a deeper insight into the microscopic structure and allow distinction between different phases. Particularly, pair correlation functions along ($g_{||}$) and perpendicular ($g_\perp$) to the rod axis help to identify the phase of a system [18]. Like the radial pair correlation function, the functions $g_{||}(r_{||})$ and $g_\perp(r_\perp)$ are local densities divided by the overall density of the system. The region where the local density is obtained is chosen relative to a reference rod with center of mass $\mathbf{r}_0$ and a rod axis parallel to $\mathbf{u}_0$. Let $c(\mathbf{r}, \mathbf{u}, h, R)$ be a cylinder with a center of mass at $\mathbf{r}$, a rod axis parallel to $\mathbf{u}$, a height h and a radius R. Then $g_{||}(r_{||})$ considers the local density in the cylinders $c(\mathbf{r}_0 \pm \mathbf{u}_0\, r_{||}, \mathbf{u}_0, h_{||}, R_{||})$, where we chose $h_{||} = 0.05D - 0.1D$ and $R_{||} = 0.75D - 1D$. The function $g_\perp(r_\perp)$ takes account of rods whose center of mass lie within the cylinder $c(\mathbf{r}_0, \mathbf{u}_0, h_\perp, r_\perp + \delta R/2)$ but not in the cylinder $c(\mathbf{r}_0, \mathbf{u}_0, h_\perp, r_\perp - \delta R/2)$. The described geometry is a hollow cylinder of height $h_\perp$, radius $r_\perp$ and shell thickness δR where $h_\perp = 0.75D$ and δR is chosen between $0.05D$ and $0.1D$. Fig. 2.11 illustrates the geometry of both correlation functions.

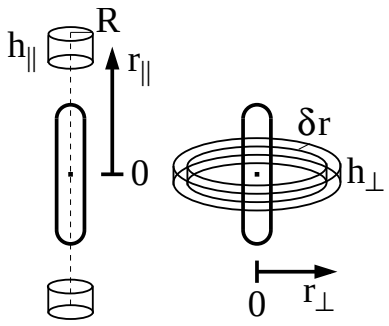

Figure 2.11: Sketch of the regions relative to a reference rod, which are used to determine the longitudinal and transverse pair correlation functions $g_{||}$ and $g_{\perp}$.

2.5.3 Density distribution function

Systems with an adjacent wall are analyzed in terms of density distribution functions. The density distribution function $\rho^*(z)$ is defined as the local number density $n(z)$ of rods with the z-coordinate of the center of mass at z normalized to the bulk number density N/V:

$$\rho^*(z) \equiv \frac{n(z)}{N/V} \tag{2.39}$$

$n(z)$ has the dimension particles per volume and represents an ensemble average. Note that $\rho^*(z)$ is dimensionless and may also be called a reduced density. In practice, the z-axis has to be discretized into intervals $(z_i - \Delta z/2, z_i + \Delta z/2]$. Therefore, the simulation box is divided into slices of thickness Δz as indicated in Fig. 2.12. $n(z)$ is the number of rods in the

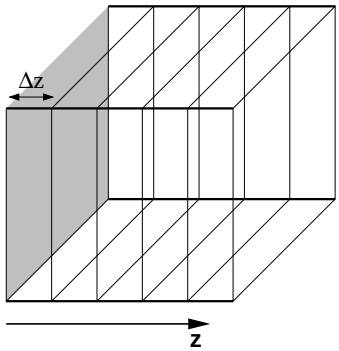

Figure 2.12: Illustration of the division of the simulation box into slices of thickness Δz.

corresponding slice divided by the volume of the slice.

For investigations of polydisperse mixtures, the density distribution function is measured for every rod component separately. For the rod component

with axis ratio λ one has:

$$\rho^*_\lambda(z) = \frac{n_\lambda(z)}{N_\lambda/V}, \tag{2.40}$$

where $n_\lambda(z)$ is the number density of rods with axis ratio λ in the slice located at z and N_λ is the total number of rods with axis ratio λ. In Section 4.2, results for cumulative density distribution functions are presented, for which more than one rod length is subsumed. The cumulative density distribution function of the components λ_1 and λ_2 is given by

$$\rho^*_{\lambda_1,\lambda_2}(z) = \frac{n_{\lambda_1}(z) + n_{\lambda_2}(z)}{(N_{\lambda_1} + N_{\lambda_2})/V}. \tag{2.41}$$

Note that $\rho^*_{\lambda_1,\lambda_2}(z) \neq \rho^*_{\lambda_1} + \rho^*_{\lambda_2}$.

2.5.4 Spatially resolved mole fraction

The effectiveness of various substrate patterns as far as demixing is concerned is also studied in terms of the spatially resolved mole fraction $x_\lambda(z)$. The mole fraction can be expressed in terms of the local number density as

$$x_\lambda(z) = \frac{n_\lambda(z)}{\sum\limits_\lambda n_\lambda(z)}. \tag{2.42}$$

Thus, $x_\lambda(z)$ is the number of rods with axis ratio λ in the respective slice divided by the overall number of rods in that slice.

In Section 4.2, results are presented, for which the mole fraction is considered in a larger volume than that of a slice, for example the volume inside the substrate structure. If the respective volume starts at $z_{\min}$ and ends at $z_{\max}$, the integrated mole fraction is given by

$$x^{\text{int}}_\lambda = \frac{n^{\text{int}}_\lambda}{\sum\limits_\lambda n^{\text{int}}_\lambda}. \tag{2.43}$$

with

$$n^{\text{int}}_\lambda \equiv \int\limits_{z_{\min}}^{z_{\max}} dz\ n_\lambda(z). \tag{2.44}$$

Note that x^{int}_λ is z-independent.

2.5.5 Orientational correlation functions

In addition to the density distribution function, which probes center of mass correlations, the two functions $g_\theta(z)$ and $g_\phi(z)$, which probe the influence of the substrate on the orientational degrees of freedom, are introduced. g_θ and g_ϕ will be called orientational correlation functions. One distinguished direction in simulations with an adjacent wall is the normal to the wall, i. e. the z-axis. Let $\cos\theta_i$ be the scalar product of rod i with director $\mathbf{u}_i$ and the unit vector in z-direction $\mathbf{e}_z$:

$$\cos\theta_i = \mathbf{u}_i \cdot \mathbf{e}_z = u_{i,z}. \tag{2.45}$$

The correlation function $g_\theta(z)$ is defined via the second Legendre polynomial $P_2(\cdot)$ as an ensemble average. The contributions are restricted to the N_z rods a distance z apart from the substrate:

$$g_\theta(z) \equiv \left\langle \frac{1}{N_z} \sum_{i=1}^{N_z} P_2(\cos\theta_i) \right\rangle \tag{2.46}$$

$$= \left\langle \frac{1}{2\,N_z} \sum_{i=1}^{N_z} \left(3\cos^2\theta_i - 1\right) \right\rangle. \tag{2.47}$$

In other words, $g_\theta(z)$ is nothing but the z-dependence of the nematic order parameter (Eq. 2.36) with the director parallel to the z-axis. g_ϕ is defined analogously but with a the director parallel to the x-axis. The x-direction is distinguished in simulations of structured substrates because of the choice of the structure.

Some remarks about the orientational correlation functions: g_θ and g_ϕ vanish if correlations are absent and adopt one if the considered rods point in the respective direction. If the majority of rods are perpendicular to the z-axis, for example, g_θ becomes negative with a lower bound of $-1/2$. Thus, g_θ and g_ϕ provide information about the preferred local orientation of the rods and about the range of substrate induced orientational correlations.

Chapter 3

Bulk behavior

3.1 Monodisperse systems

Systems of attractive spherocylinders are scarcely discussed in the literature. For the AR potential, used here, the phase diagram has only been analyzed for monodisperse systems with $\lambda = 5$ [8]. Therefore, in this section some new regions of the phase diagram of monodisperse suspensions are explored before we turn towards polydisperse systems. In the following, a dimensionless interaction strength $\epsilon^* \equiv \epsilon/kT$ is used. A reduced pressure is defined as $P^* = P\langle v\rangle/kT$, where $\langle v\rangle$ is the average volume of a rod:

$$\langle v\rangle = \frac{\pi D^3}{6} + \frac{\pi D^2}{4N}\sum_{i=1}^{N} L_i. \tag{3.1}$$

In monodisperse systems, $\langle v\rangle$ is the volume of a spherocylinder. Phase diagrams for interaction strengths $\epsilon^* = 0.25$ and $\epsilon^* = 0.5$ are presented as a function of the reduced pressure P^* and the axes ratio λ, which ranges from $\lambda = 3$ to $\lambda = 8$.

Simulations are started with an isotropic system at low pressure, which is then compressed and equilibrated step by step to obtain an isotherm. Close to phase boundaries, the pressure is increased in particularly small steps to avoid glassy states. Discontinuous phase transitions are always accompanied by hysteresis. As long as the hysteresis is small, phase boundaries can be localized well by compressing and expanding the system. Generally, for all isotropic-nematic transitions the hysteresis was found to be sufficiently small. In some cases, especially if the hexatic phase is involved, large hysteresis appears.

Isotherms at compression and expansion of a system of rods with $\lambda = 3$ and interaction strength $\epsilon^* = 0.5$ are presented in Fig. 3.1 (a). $\langle E_{\mathrm{rod}}\rangle/E_{\mathrm{min}}$

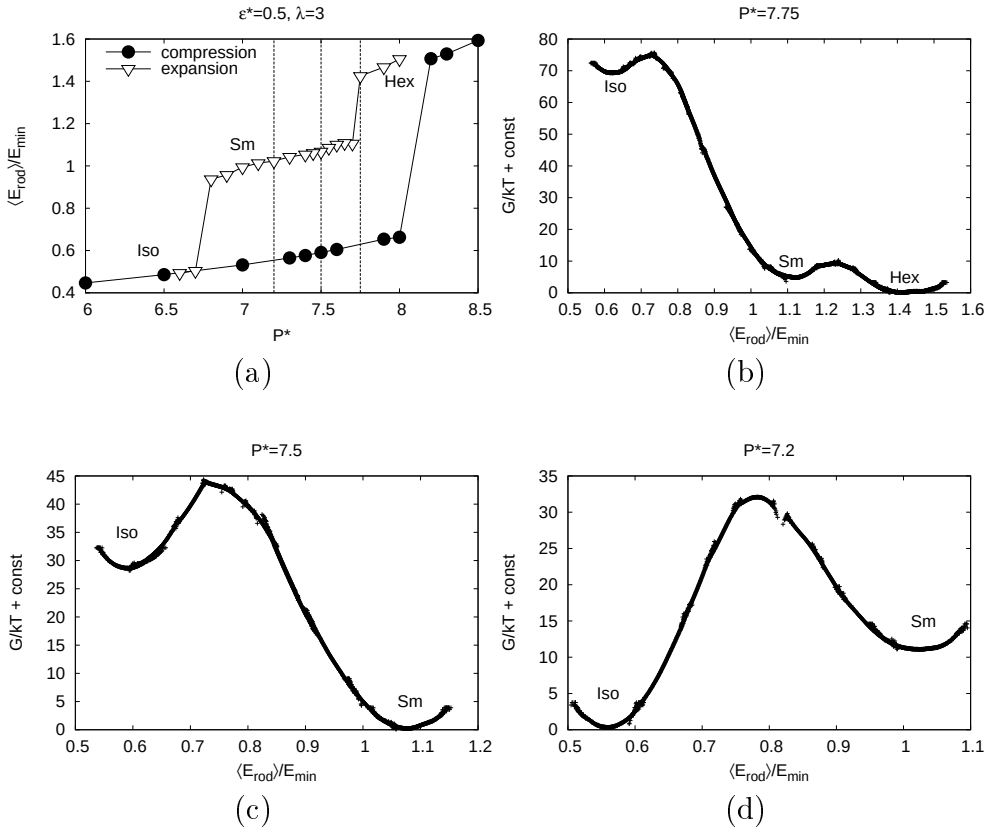

Figure 3.1: Analyzing the phase behavior of attractive rods. (a) The internal energy per rod $\langle E_{\text{rod}} \rangle$ divided by the strongest pair interaction energy E_{min} as a function of the pressure P^* at isothermal compression (●) and isothermal expansion (▽) of rod systems with $\lambda = 3$ and $\epsilon^* = 0.5$. The free energy G as a function of $\langle E_{\text{rod}} \rangle / E_{\text{min}}$ (b) at $P^* = 7.75$, (c) at $P^* = 7.5$, and (d) at $P^* = 7.2$.

is plotted along the ordinate. $\langle E_{\text{rod}} \rangle$ is the average interaction energy per rod and E_{min} is the minimum pair interaction energy as given in Eq. (2.19). Note that both $\langle E_{\text{rod}} \rangle$ and E_{min} are negative. The hysteresis is so strong that the isotherm at compression detects only the isotropic and the hexatic phase whereas at expansion a smectic A phase is observed over a large pressure range. In order to identify the stable phases and thus to locate the phase boundaries, biased multi-histogram simulations (Sec. 2.4.1) are employed, in which the free energy G is determined as a function of $\langle E_{\text{rod}} \rangle / E_{\text{min}}$. To be precise, $G + const$ is measured, but the constant has no physical relevance. Parts (b)-(d) of Fig. 3.1 present free energy profiles of systems at the pres-

sure $P^* = 7.75$, $P^* = 7.5$, and $P^* = 7.2$, which are indicated in Fig. 3.1 (a) by the dashed vertical lines. At $P^* = 7.75$, three minima appear, two from the metastable isotropic and smectic A phase and one from the thermodynamically stable hexatic phase. At this point, we already see the advantage in utilizing the internal energy as reaction coordinate. Firstly, $\langle E_{\mathrm{rod}} \rangle$ distinguishes significantly between the hexatic, smectic A, and the less ordered phases. Secondly, no additional computational efforts are necessary to determine E_{rod} during the simulation, since one has to keep track of the internal energy, in any case, to evaluate the Metropolis criterion. The probability of overcoming a free energy barrier of height ΔG_b between two states is proportional to $\exp(-\beta \Delta G_b)$ [45]. In our case, the isotropic state is separated from the smectic A or hexatic state by an amount of $\Delta G_b \approx 7kT$ at the pressure $P^* = 7.75$ (Fig. 3.1 (b)). The barrier could not be passed within 5×10^7 Monte Carlo sweeps at even higher pressure ($P^* = 7.9$), where the barrier height is supposed to be smaller. At compression, the system does not cross the free energy barrier to the stable smectic A phase until the smectic phase itself becomes unstable. Thus, the system switches directly from the isotropic to the hexatic phase. At $P^* = 7.75$, the free energy difference ΔG between the isotropic and the hexatic state is about $70kT$.

The free energy profile at $P^* = 7.5$ is depicted in Fig. 3.1 (c). The global minimum in G corresponds to the smectic A phase, which is now thermodynamically stable. The isotropic and the smectic A state are separated by a barrier of circa $15kT$ and the free energy of the two phases differs by an amount of about $28kT$. The isotropic state is stable at $P^* = 7.2$ as demonstrated in Fig. 3.1 (d).

The free energy profiles give information not only about the stability of phases but also about the surface energy between two phases, which are simultaneously present in the simulation box. An example is given in Fig. 3.2 (a), where the free energy profile of a system of rods with axis ratio $\lambda = 8$ and $\epsilon^* = 0.5$ is plotted. The two minima of the free energy correspond to the nematic and the hexatic phase. The hexatic phase corresponds to the global minimum and is, thus, thermodynamically stable. In the range $1 \leq \langle E_{\mathrm{rod}} \rangle / E_{\mathrm{min}} \leq 1.6$, the slope of the free energy is constant as indicated by the dashed line. The line tangential to the two minima of the respective phases (double tangent) exhibits the same slope and is also drawn in the diagram.

On the basis of Fig. 3.2 (a) some principles of thermodynamics will be exemplified. The free energy difference between the nematic and the hexatic phase in this case is $\Delta G \approx 70kT$. Since the free energy G is extensive, a system with twice as many particles would possess a free energy difference of $140kT$. A system prepared in the nematic state would have to overcome an

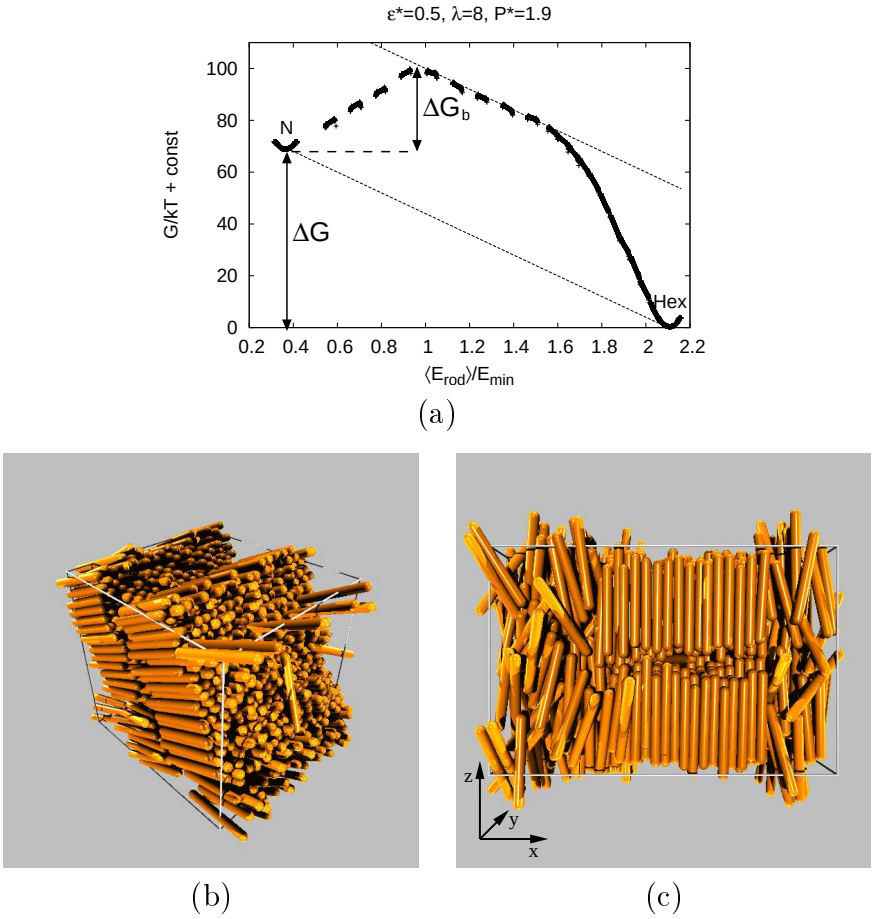

Figure 3.2: (a) Free energy G as function of $\langle E_{\text{rod}}\rangle/E_{\text{min}}$ in a system of rods with $\lambda = 8$ and $\epsilon^* = 0.5$ at $P^* = 1.9$. Snapshot of a system biased (b) at $\langle E_{\text{rod}}\rangle/E_{\text{min}} \approx 1.76$ and (c) at $\langle E_{\text{rod}}\rangle/E_{\text{min}} \approx 1.26$.

energy barrier of $\Delta G_b \approx 30kT$ to reach the thermodynamically stable state. The energy barrier is connected to the interface of the two phases, i. e. a surface costs energy. From the free energy profile, the surface tension σ between the hexatic and the nematic phase can be estimated as $\sigma \approx 0.062kT/D^2$. The corresponding calculation is given in Appendix D. The snapshot in Fig. 3.2 (c) shows a typical configuration at $\langle E_{\text{rod}}\rangle/E_{\text{min}} \approx 1.26$, which is in the regime of constant slope in G. The constant slope is because of the fact that the size of the phases can be varied without changing the interfacial area. From the snapshot (Fig. 3.2 (c)) we see that the hexatic phase fills the simulation box completely in y- and z-direction and a change of the phase extension in x-direction would not change the surface area. In the

ideal case, where a direct interface of the phases is absent (for example in a Gibbs simulation), the free energy profile between the nematic and the hexatic state would coincide with the double tangent, which connects both minima in Fig. 3.2 (a).

The knowledge of the surface tension and the free energy difference ΔG is sufficient to estimate the size of the critical nucleus according to classical nucleation theory (CNT). Suppose the system is prepared in the nematic state and the free energy landscape is that of Fig. 3.2 (a). In such a situation, the system is said to be overcompressed. Because of thermal fluctuations, small hexatic nuclei build and dissolve again. If the nucleus exceeds a certain size, it will spontaneously grow instead of dissolving. We assume that the shape of such a nucleus is like a cylinder of radius r and height h and the rods are aligned with the long axis of the cylinder. The height h is not continuous but an integer value of the layer thickness. We denote the change in free energy associated with the formation of a cylindrically shaped hexatic nucleus by $\Delta G_n(r,h)$. The system gains an amount of free energy $-r^2\pi h\,\Delta g$, where Δg is the free energy density ($\Delta g = \Delta G/V$). The costs for the creation of a nucleus are due to the surface tension. In our case we distinguish between the surface tension $\sigma_{||}$ and $\sigma_\perp$, which are related to the surface parallel and to the surface perpendicular to the rod direction, respectively. Thus, the net free energy change related to the cluster formation is

$$\Delta G_n(r,h) = -\pi r^2 h\,\Delta g + 2\pi r h \sigma_{||} + 2\pi r^2 \sigma_\perp. \tag{3.2}$$

The critical nucleus size at a fixed height h is obtained from the extremal condition

$$\frac{\partial \Delta G_n(r,h)}{\partial r} = 0, \tag{3.3}$$

which leads to the critical cylinder radius

$$r_{\text{crit}} = \frac{h\,\sigma_{||}}{h\,\Delta g - 2\sigma_\perp}. \tag{3.4}$$

In our case, the cylinder is de facto infinitely high. The finite dimension of the simulation box and the periodic image convention are responsible for an absence of the top and bottom contact zone between the nematic and the hexatic phase (cmp. Fig. 3.2 (c)). Thus, the contribution from $\sigma_\perp$ vanishes. Formally, the situation is equivalent with the limit $h \to \infty$, where the critical cylinder radius becomes $r_{\text{crit}} = \sigma_{||}/\Delta g$, which, in our case, corresponds to about $13D$. Note that $\sigma_{||}$ is equal to the σ calculated above.

The applicability of CNT to systems of rodlike particles is subject to legitimate concerns. In overcompressed systems of isotropic hard rods, nucleation

of multilayer structures is suppressed due to self-poisoning [73]. The results presented here are all obtained using the highly ordered hexatic state as starting configuration. The estimation of r_{crit} according to CNT should thus be understood as the radius, at which a shrinking hexatic region becomes unstable.

In Fig. 3.3, we present isotherms for different rod lengths at $\epsilon^* = 0.5$. Plot 3.3 (a) shows the orientational order parameter S_∞. Systems, which

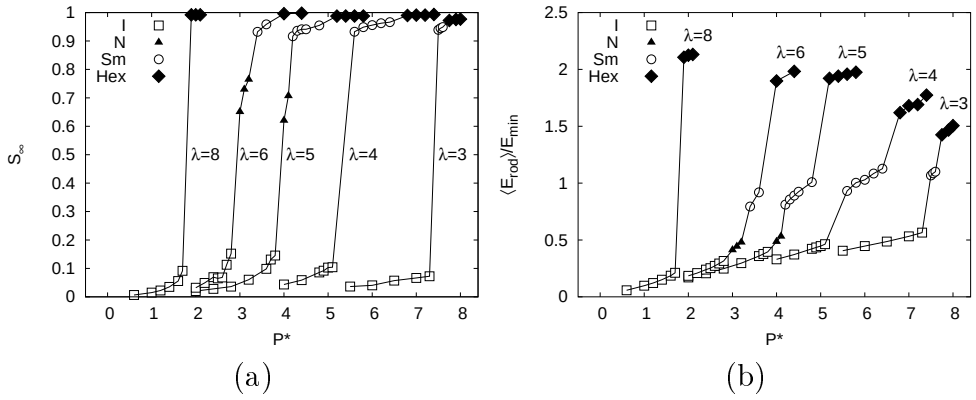

Figure 3.3: (a) The orientational order parameter S_∞ as a function of the reduced pressure P^* for monodisperse systems with different axis ratios λ. The symbols are measurements and are chosen differently for the different phases ($\square$ = isotropic, $\blacktriangle$ = nematic, $\bigcirc$ = smectic A, and $\blacklozenge$ = hexatic phase). (b) The reduced interaction energy per particle $\langle E_{\mathrm{rod}}\rangle/E_{\mathrm{min}}$ as function of the pressure P^*. $\langle E_{\mathrm{rod}}\rangle/E_{\mathrm{min}}$ differs distinctly between the hexatic, the smectic A, and the less ordered phases.

are deep in the isotropic state, have an order parameter $S_\infty < 0.1$. Close to the isotropic-nematic phase transition values, in the range $0.1 < S_\infty < 0.2$ are found, which arise from small transient nematic clusters that form in the isotropic system. During a simulation run, several cluster formations and dissolutions can be observed.

A jump of S_∞ is found at the transition to the nematic phase, where the nematic order parameter lies in the range $0.5 < S_\infty < 0.8$ and increases distinctly with P^*. Another discontinuous increase of S_∞ occurs at the nematic-smectic A transition, while within the smectic A phase S_∞ depends only slightly on P^*. At further compression, a transition to a hexatic phase occurs. The phases are recognized by the orientational order and the analysis of the spatial order, discussed below. The smectic-hexatic transition is accompanied by a small increase of S_∞, while a significant jump in the average interaction energy per particle $\langle E_{\mathrm{rod}}\rangle$ occurs. This is demonstrated in

Fig. 3.3 (b), where $\langle E_{\rm rod}\rangle/E_{\rm min}$ is shown as a function of P^* for various axis ratios λ. In fact, jumps in $\langle E_{\rm rod}\rangle/E_{\rm min}$ turn out to be a sensitive method for localizing all but the isotropic-nematic phase transition. The isotropic and nematic phase is characterized by $\langle E_{\rm rod}\rangle/E_{\rm min} \lesssim 0.5$, the smectic A phase by $\langle E_{\rm rod}\rangle/E_{\rm min} \approx 1$ and the hexatic phase by $\langle E_{\rm rod}\rangle/E_{\rm min} > 1.3$.

In order to recognize the liquid crystalline phases, spatial order is investigated with the help of pair correlation functions. Results for the longi-

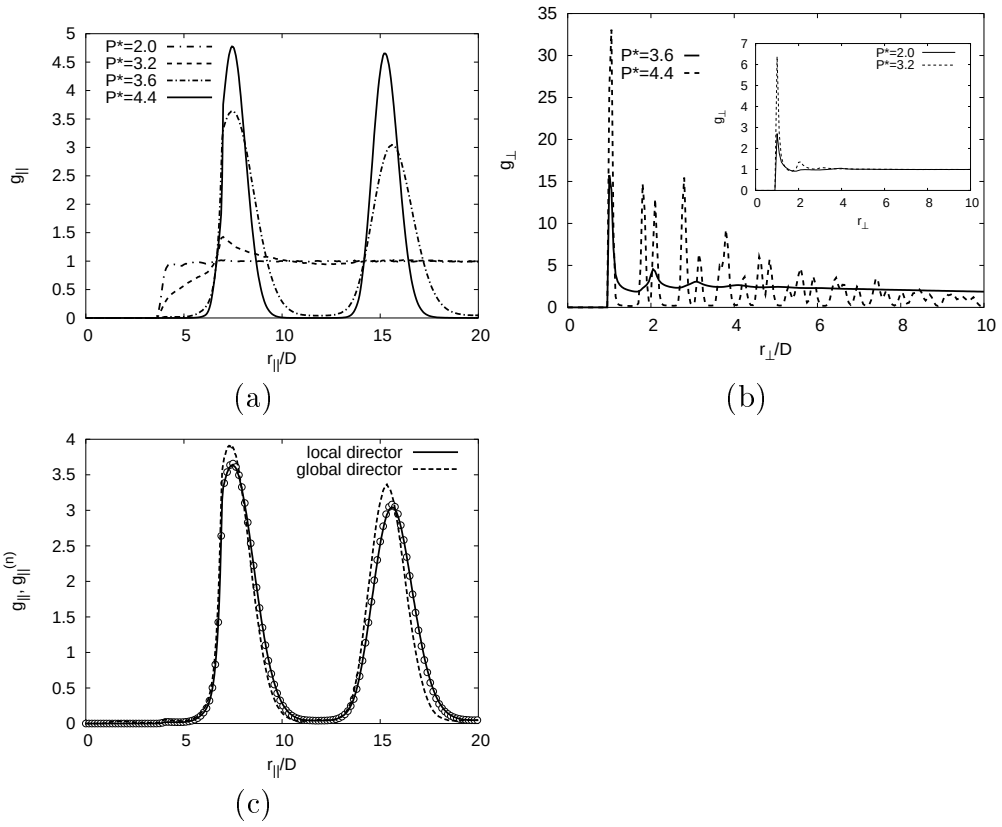

Figure 3.4: Pair correlation functions in the isotropic ($P^* = 2.0$), nematic ($P^* = 3.2$), smectic A ($P^* = 3.6$) and hexatic ($P^* = 4.4$) phase for rods with axis ratio $\lambda = 6$ and $\epsilon^* = 0.5$. (a) Longitudinal pair correlation function $g_{||}$ as function of the longitudinal distance $r_{||}$. (b) Transverse pair correlation function $g_\perp$ as function of the transverse distance $r_\perp$. Results for the isotropic and the nematic phase are shown in the inset. (c) A comparison of longitudinal pair correlation functions in the smectic A phase ($P^* = 3.6$): Pair correlations along the direction of the molecular axes $g_{||}$ (—), and along the layer normals $g_{||}^{(n)}$ (– – –). Symbols correspond to a system with $N = 2000$, while lines refer to $N = 1000$ rods.

tudinal and the transverse pair correlation function are shown in Fig. 3.4 for rods with axis ratio $\lambda = 6$. The longitudinal pair correlation function $g_{||}$ shows long range order in the smectic A and the hexatic phase. In the nematic phase, $g_{||}$ reveals a single peak at $r_{||} \approx 7D$, corresponding to the total rod length of $(6+1)D$. In the isotropic phase, longitudinal correlations are hardly visible. Since the pair correlation function $g_{||}$ is defined locally via the molecule axes, periodic oscillations in $g_{||}$ do not ensure a smectic A state of the system, since the parallel layers may show long-range bending. The flatness of the layers can be tested with the longitudinal pair-correlation function $g_{||}^{(n)}$ along the axis of the global director $\mathbf{n}$. As shown in Fig. 3.4 (c), $g_{||}^{(n)}$ also shows the characteristic oscillations of a smectic A system. In order to check system-size dependencies of the pair correlation functions, we have performed simulations with different numbers of rods. In Fig. 3.4 (c), the continuous line shows $g_{||}$ for a system of $N = 1000$ rods while symbols refer to a system of $N = 2000$ rods. Apparently, $g_{||}$ shows no significant finite-size effects. System-size dependencies of $g_{\perp}$ (not shown) were below the accuracy of measurement.

Correlations perpendicular to the rod axis show one maximum in the isotropic and two maxima in the nematic phase (inset of Fig. 3.4 (b)). At $P^* = 3.6$, where the system is in a smectic A phase, a number of maxima is visible, all approximately separated by a distance D. The hexatic structure at $P^* = 4.4$ becomes evident from the typical double peak pattern in $g_{\perp}$ [32]. Together with the nematic order parameter and E_{rod}, the pair correlation functions allowed the determination of the respective phases.

A comprehensive overview of the phase behavior found for monodisperse systems of attractive spherocylinders is given in Fig. 3.5, where phase diagrams for systems with $\epsilon^* = 0.25$ and $\epsilon^* = 0.5$ are shown in the $P^*\lambda$-plane. For $\epsilon^* = 0.25$, an isotropic and a smectic A phase exists for axis ratios $4 \leq \lambda \leq 8$. A hexatic phase sets in at higher pressures, beyond the smectic points shown in Fig. 3.5 (a), but has not been studied in detail for $\epsilon^* = 0.25$. The nematic region widens with increasing λ in agreement with the phase behavior found for hard spherocylinders [7]. Note that the AR model is equivalent to the hard spherocylinder model for $\epsilon^* = 0$.

For $\epsilon^* = 0.5$, the nematic and the smectic A phase are restricted to rods of intermediate length. The nematic phase exists only for rods with axis ratios $4 < \lambda < 8$, while a smectic A phase exists in the range $3 \leq \lambda < 7$. The smectic A and the nematic phase regions are lens shaped. For large axis ratios λ, both regions are narrowed by a predominant hexatic phase.

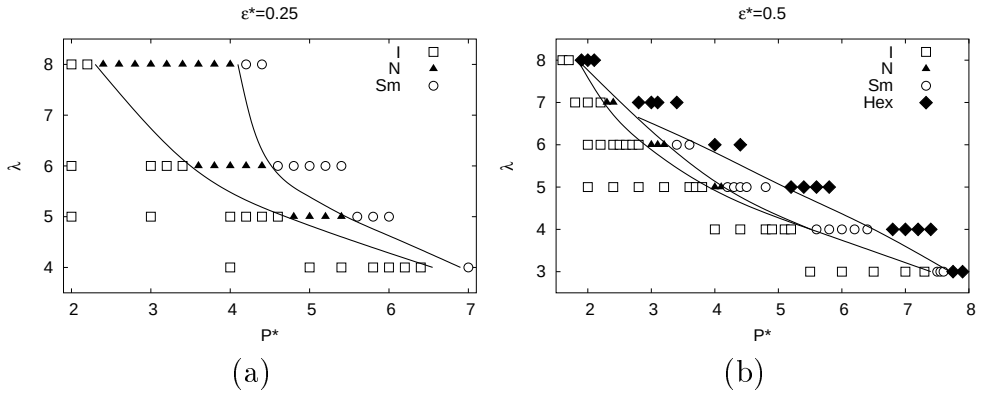

(a) (b)

Figure 3.5: Phase diagram for monodisperse systems of attractive spherocylinders as function of the parameters pressure P^* and axis ratio λ (a) at interaction strength $\epsilon^* = 0.25$ and (b) at interaction strength $\epsilon^* = 0.5$.

3.2 Tridisperse mixture

In this section, a tridisperse rod suspension is investigated. The system is composed of long ($\lambda = 7$), intermediate ($\lambda = 5$), and short ($\lambda = 3$) rods. The composition is chosen such that every component occupies the same volume fraction, i. e. the mixing ratio is $0.226 : 0.304 : 0.47$. Albeit its relatively simple composition, the tridisperse mixture serves as a kind of model mixture for more realistic compositions, which will be discussed in Section 3.3. It reproduces most of the effects observed in polydisperse suspensions with the additional advantage that an axis ratio resolved analysis is restricted to only a few components. Furthermore, thermal averages of λ-dependent observables can be obtained with very good statistical accuracy since there are many rods with the same axis ratio.

In the following, we analyze the structure formation in tridisperse suspensions of hard ($\epsilon^* = 0$) and attractive rods ($\epsilon^* = 0.5$). Therefore, it is illuminative to measure the orientational order parameter and the pair correlation functions separately for every component. Fig. 3.6 presents results for S_∞ as a function of the reduced pressure P^*. Some qualitative properties are independent of the interaction strength. In a system with given ϵ^* and P^*, the nematic order increases with the axis ratio of the component. At low pressure, the system is isotropic and S_∞ is almost zero for all rod lengths.

In contrast, the orientational order at higher pressures depends distinctly on ϵ^*. In Fig. 3.6 (a) the system of attractive rods is analyzed. Below $P^* = 2.84$, all components show almost no orientational order. From $P^* =$

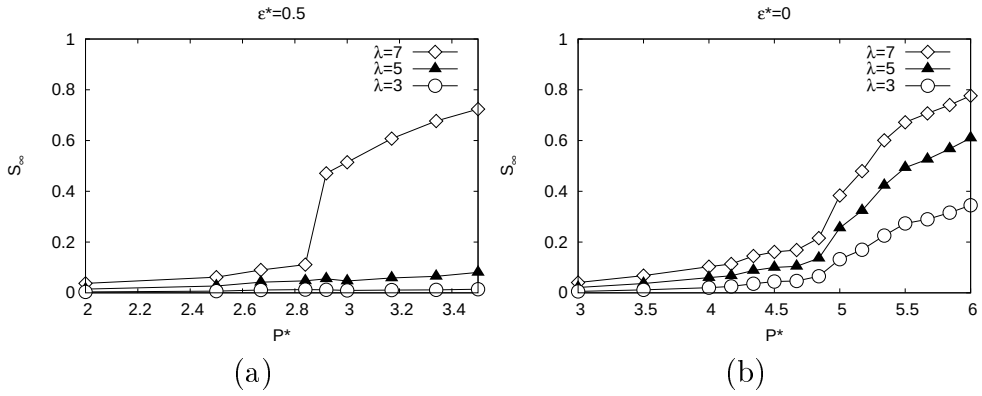

Figure 3.6: The axis ratio resolved nematic order parameter S_∞ as a function of the pressure P^* for (a) attractive ($\epsilon^* = 0.5$) and (b) hard rods ($\epsilon^* = 0$). (a) S_∞ jumps only for the longest constituent. Shorter rods remain isotropic. (b) All rod lengths participate in the global alignment.

2.84 to $P^* = 2.92$, a distinct jump can be seen in S_∞ for the longest rods ($\Diamond$) whereas the intermediate ($\blacktriangle$) and short rods ($\bigcirc$) stay isotropic even at further compression.

Data for hard rods is presented in Fig. 3.6 (b). The isotherms for all components show the same behavior qualitatively. Below $P^* = 4.84$, in the isotropic phase, S_∞ increases slightly and approximately linearly with P^*. For $P^* \geq 5$ the nematic order of all rod lengths grows significantly faster with P^*, an effect that increases with the rod length. In comparison to attractive rods, three points should be emphasized: Firstly, nematic order sets in at a higher pressure. Because of the absence of attractive interaction, orientational ordering is induced by steric interaction, exclusively. Secondly, all components contribute to the order in the system and thirdly, at the transition from the isotropic to the ordered state, the nematic order parameter increases less abruptly than for attractive rods.

Fig. 3.7 displays typical configurations of ordered systems. For the sake of clarity, small and intermediate rods are omitted. Attractive rods (Fig. 3.7 (a)) build a highly ordered monolayer of long rods surrounded by an isotropic fluid of shorter rods. As demonstrated below, the layer shows hexatic order. Hard rods (Fig. 3.7 (b)) do not arrange in a layer but develop a nematic structure.

Pair correlation functions reveal a deeper understanding of the structure of the considered systems. For a detailed analysis, the longitudinal and transverse pair correlation functions $g_{||}$ and $g_\perp$, as introduced in Section 2.5.2,

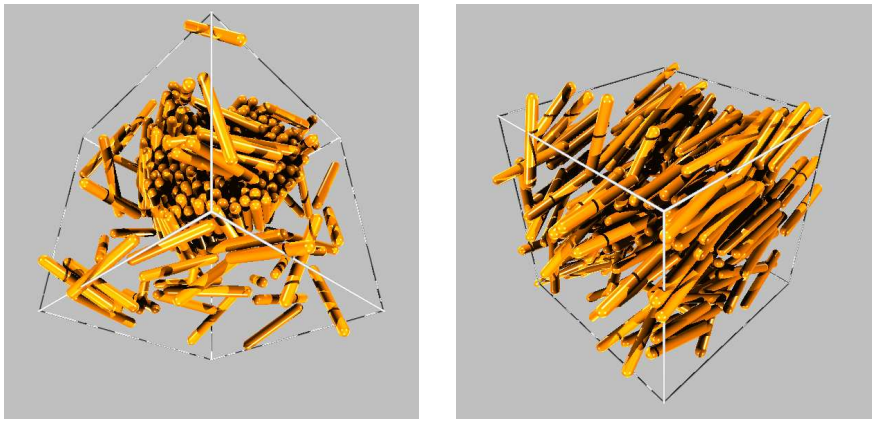

(a) $\epsilon^* = 0.5$, $P^* = 3.17$ (b) $\epsilon^* = 0$, $P^* = 6$

Figure 3.7: Representative configurations of (a) attractive rods ($\epsilon^* = 0.5$) at the pressure $P^* = 3.17$ and (b) hard rods ($\epsilon^* = 0$) at the pressure $P^* = 6$. Rods with axis ratio $\lambda = 3$ and $\lambda = 5$ are not drawn in the snapshot. (a) A hexatic monolayer of long rods ($\lambda = 7$) has formed, which is surrounded by an isotropic fluid of shorter rods ($\lambda \in \{3, 5\}$). (b) The system is nematic.

are additionally apportioned to rod lengths. Thus, $g_{||}^{(\lambda_{\mathrm{ref}},\lambda)}$ and $g_{\perp}^{(\lambda_{\mathrm{ref}},\lambda)}$ analyze the normalized densities of rods with axis ratio λ in the vicinity of reference rods with axis ratio λ_{ref}. In the following, only the longest rods serve as reference rods, i. e. $\lambda_{\mathrm{ref}} = 7$.

Before we turn to the data analysis, it is instructive to outline some typical rod configurations, which lead to peaks in the pair correlation functions. A constellation like in Fig. 3.8 (a) corresponds to the closest distance in the longitudinal direction. The closest distance in the transverse direction is sketched in Fig. 3.8 (c). The former configuration contributes to $g_{||}$ at $r_{||}/D \approx \lambda_{\mathrm{ref}}/2 + 1$ while the latter contributes to $g_{\perp}$ at $r_{\perp}/D \approx 1$. The configurations drawn in Figs. 3.8 (b) and (d) are listed because the orientational degrees of freedom of the target rod (red color) are no longer constrained by the reference rod (green color). The contributions to $g_{||}$ and $g_{\perp}$ are located at $r_{||}/D \approx (\lambda_{\mathrm{ref}} + \lambda)/2 + 1$ and $r_{\perp}/D \approx \lambda/2 + 1$, respectively. The four mentioned rod configurations will be noted in short as '$-|$', '$--$', '$||$', and '$|-$' configurations as indicated in Fig. 3.8, with the left dash representing the orientation of the reference rod. Finally some remarks about the reasons why the four emphasized rod constellations lead to maxima in the pair correlation functions: They are distinct because the entropy of the target rod and the entropy of the rest of the system are balanced well at the respective separations. Consider the '$|-$' constellation, for example. If we increase $r_{\perp}$ to a

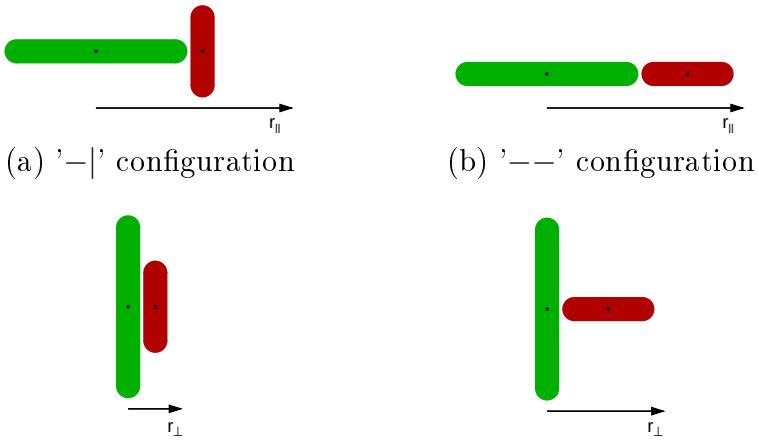

(a) '−|' configuration (b) '−−' configuration

(c) '||' configuration (d) '|−' configuration

Figure 3.8: Schematic drawing to illustrate the occurrence of maxima in the pair correlation functions. The reference rod is colored green.

value slightly larger than $(\lambda/2+1)D$, the orientational degrees of freedom of the target rod would not change, but some inaccessible volume between the reference rod and the target rod would be generated, which is unfavorable for the rest of the system. The attractive rod potential U_{AR} additionally enhances '||' configurations whereas attractive interactions play only a minor role for the other configurations.

Pair correlation functions in the isotropic regime of a hard rod system are depicted in Fig. 3.9. Part (a) shows the longitudinal pair correlation function $g_{||}$. Two maxima are observed in $g_{||}^{(7,3)}$ (**– – –**), the first from '−|' and the second from '−−' configurations. The first maximum is also observed in $g_{||}^{(7,5)}$ but here the second one is very small. The data for $g_{||}^{(7,7)}$ is not shown because the curve is basically identical with $g_{||}^{(7,5)}$. Correlations are absent for $r_{||} \gtrsim 7D$. In part (b) of Fig. 3.9, the transverse pair correlation function $g_{\perp}^{(7,\lambda)}$ is plotted for $\lambda = 3$, $\lambda = 5$, and $\lambda = 7$. The location of the first peak ('||' configurations) is identical for all λ at $r_{\perp} \approx 1D$ while the height increases with the axis ratio. The second peak stems from '|−' configurations and thus its location depends on λ. Note that the locations of the second peaks coincide very precisely with $\lambda/2+1$. The height of the peaks decreases with increasing rod length. The behavior of the pair correlation functions in combination with the small nematic order parameter underlines the isotropic nature of the system at $P^* = 2$.

Another set of pair correlation functions of hard rods is presented in Fig. 3.10, where the structure of the suspension is investigated in the high

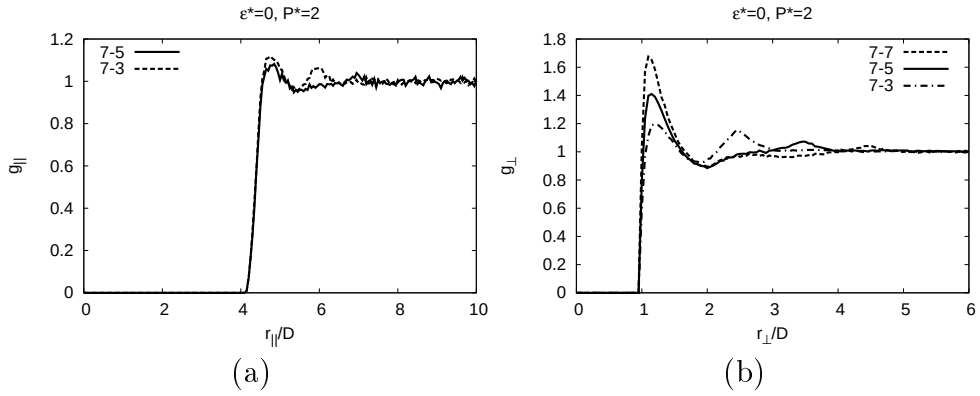

Figure 3.9: Pair correlation functions in an isotropic system of hard rods ($\epsilon^* = 0$) at pressure $P^* = 2$. (a) Longitudinal pair correlation function $g_{||}$ as function of the longitudinal distance $r_{||}$. (b) Transverse pair correlation function $g_\perp$ as function of the transverse distance $r_\perp$. In both cases, correlations are very weak and short-ranged.

pressure region ($P^* = 6$). As we already know from the analysis of the nematic order parameter, the hard rod system aligns along a global director at that pressure. The long-range orientational order is also accompanied by a spatial ordering as shown in Fig. 3.10 (a). Distinct peaks from '$--$' configurations occur in $g_{||}$ at $r_{||}/D = (\lambda_{\text{ref}} + \lambda)/2 + 1$ for all rod lengths.

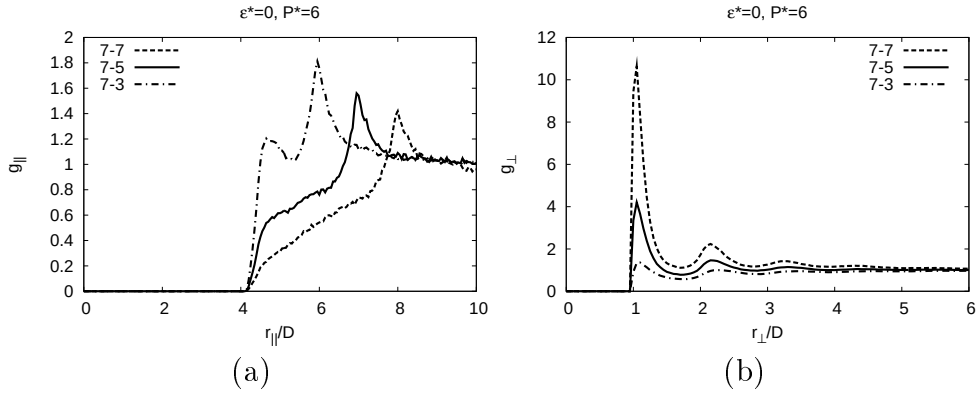

Figure 3.10: Pair correlation functions in the ordered state of a hard rod system at $P^* = 6$. (a) Longitudinal pair correlation function $g_{||}(r_{||})$. (b) Transverse pair correlation function $g_\perp(r_\perp)$. Both correlations are stronger than at $P^* = 2$ but are still short-ranged.

Longitudinal correlations are not observed for $r_{||} \geq 9D$. In the region between $r_{||} = 4D$ and the peak from the '$--$' configurations, only rods with $\lambda = 3$ show another broad maximum, which arises from '$-|$' constellations. The curves for $\lambda = 5$ and $\lambda = 7$ grow monotonically. This can be explained as follows: The volume needed for a rod to rotate freely is proportional to the third power of its length. Thus, orientational degrees of freedom are much more suppressed for long rods than those for short rods in dense systems. As a consequence, it becomes preferable for long rods to align. The direction of the long rods corresponds in good approximation to the direction of the global director $\mathbf{n}$. Obviously, only rods with $\lambda = 3$ have a sufficient amount of accessible volume to orient perpendicularly to the global director.

The maxima in the transverse pair correlation functions (Fig. 3.10 (b)) differ only in the height for different rod lengths whereas their locations coincide. The correlations are maximal approximately at integer values of the rod diameter and attain the bulk value for distances larger than $4D$. Signatures from '$|-$' configurations are missing. The combination of the results for the nematic order parameter and both correlation functions reveal the structure of a nematic fluid.

Next we turn to attractive rods. Pair correlation functions below the ordering transition are presented in Fig. 3.11. Some differences to the isotropic hard rod system will be pointed out, briefly. In Fig. 3.11 (a), $g_{||}^{(7,5)}$ (—) is significantly smaller than $g_{||}^{(7,3)}$ (—·—·) and the first peak from '$-|$' configu-

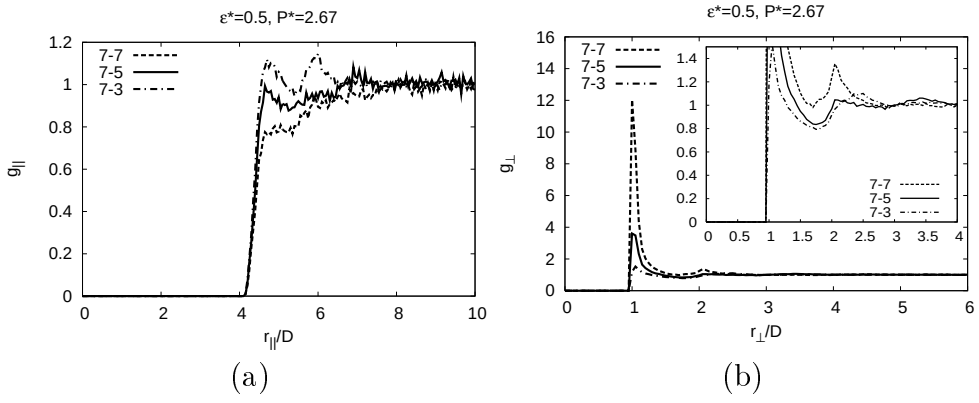

Figure 3.11: Pair correlation functions in an isotropic system of attractive rods ($\epsilon^* = 0.5$) at $P^* = 2.67$. (a) Longitudinal pair correlation function $g_{||}(r_{||})$ and (b) transverse pair correlation function $g_{\perp}(r_{\perp})$. The first maximum in $g_{\perp}$ is enhanced because of the attractivity, which favors parallel alignment. The inset highlights the second maximum in $g_{\perp}$.

rations appears to be sharper. $g_{||}^{(7,5)}$ and $g_{||}^{(7,7)}$ (– – –) differ distinctly in the range $4 \leq r_{||}/D \leq 6$ with $g_{||}^{(7,7)}$ being smaller and showing no evidence of '$-|$' constellations. As shown in Fig. 3.11 (b), transversal pair correlations are quite pronounced in the immediate neighborhood of the reference rods. The corresponding peak of $g_\perp$ at $r_\perp \approx 1D$ is a consequence of the attractive interaction. The inset of Fig. 3.11 (b) points out the characteristics of $g_\perp$ for $r_\perp \geq 2D$. One recognizes a second maximum in $g_{||}^{(7,7)}$ and also indications for '$|-$' constellations of $\lambda = 3$ and $\lambda = 5$ rods. Overall, there are no long-range correlations due to attraction in the considered system but on a shorter length scale attractivity has a certain influence.

Above the ordering transition, the structure of the system changes drastically. In Fig. 3.12 (b), a different kind of order is indicated by the double peak pattern in the transverse pair correlation function $g_\perp^{(7,7)}$ (– – –), which is characteristic for a hexatic structure [32]. The hexatic order is long-ranged

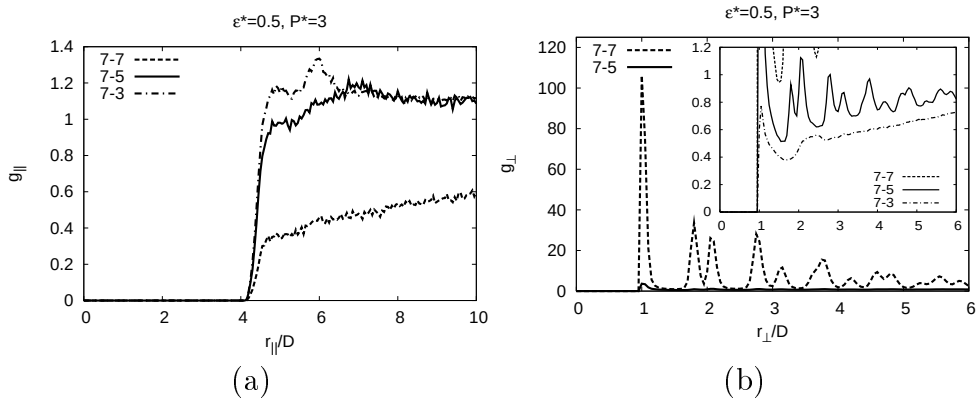

Figure 3.12: Pair correlation functions of the ordered state of an attractive rod system at $P^* = 3$. (a) The longitudinal pair correlation function $g_{||}(r_{||})$ and (b) the transverse pair correlation function $g_\perp(r_\perp)$. The double peak pattern in $g_\perp$ is characteristic for hexatic order. The inset highlights $g_\perp^{(7,5)}$ and $g_\perp^{(7,3)}$.

and almost completely restricted to $\lambda = 7$ rods. Correlations with smaller rods are about two orders of magnitude smaller and hardly visible on the scale of $g_\perp^{(7,7)}$. The inset for Fig. 3.12 (b) highlights $g_\perp^{(7,5)}$ and $g_\perp^{(7,3)}$. A double peak modulation is found for $g_\perp^{(7,5)}$ but not for $g_\perp^{(7,3)}$, which approaches the bulk value for $r_\perp \gg 6D$. The fluid has separated into a highly ordered layer of mainly long rods with only few intermediate rods incorporated. The vast majority of $\lambda = 3$ and $\lambda = 5$ rods forms an isotropic fluid surrounding the

layer. The depletion of long rods in the isotropic part is demonstrated in Fig. 3.12 (a) by $g_{||}^{(7,7)}$, which grows extremely slowly towards 1 with increasing $r_{||}$. Since most long rods are used for the layer and thus located in the transverse direction, only few $\lambda = 7$ rods are detected by $g_{||}^{(7,7)}$. The lack of a maximum at $r_{||} \approx 8D$ proves that the domain consists of a single layer. In the following, the structure of long rods will also be called (hexatic) monolayer. The peaks from '$-|$' and '$--$' configurations are visible in $g_{||}^{(7,3)}$ whereas $g_{||}^{(7,5)}$ shows only a broad maximum corresponding to '$--$' constellations.

The observed results point out that attractivity of rodlike particles has great impact on the structure formation in polydisperse bulk systems, especially at high pressure[1]. While the tridisperse mixture of hard rods is in a liquid-crystalline nematic state, attractive rods with the same composition separate into a hexatic monolayer of long and an isotropic fluid of shorter rods. Long-range positional correlations are absent in the former system while the opposite is true for the latter.

The overall structure in the low pressure regime is less strongly affected by the attractivity but the correlation functions show differences for the direct neighborhood as Fig. 3.13 demonstrates for the transverse pair correlation function. For $r_\perp \gtrsim 2D$, the presented curves coincide nicely. The largest differences between hard and attractive rods are observed for large axis ratios.

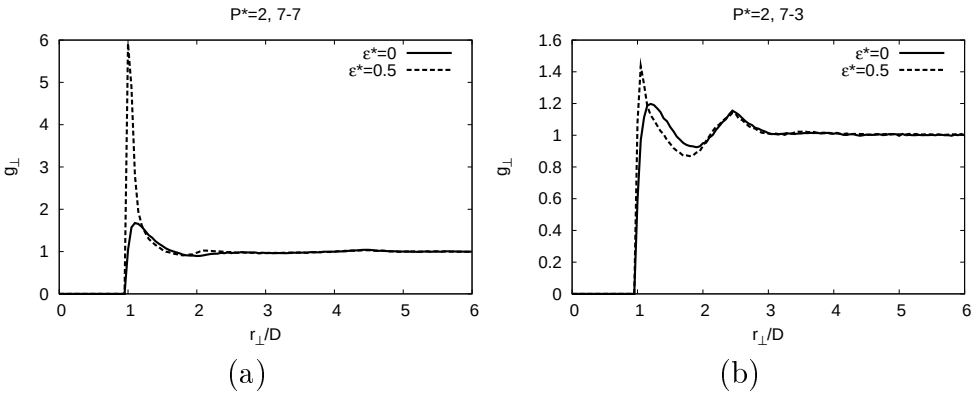

Figure 3.13: Comparison of the transverse pair correlation function $g_\perp(r_\perp)$ for hard (—) and attractive rods (– – –) in the isotropic state. (a) Correlations between long rods, i. e. $g_\perp^{(7,7)}(r_\perp)$. (b) Correlations between long and short rods, i. e. $g_\perp^{(7,3)}(r_\perp)$.

[1]The numerical value of P^* in the high pressure regime differs for hard and attractive rods.

For attractive rods, the first peak in $g_\perp$ is sharper and is shifted towards smaller $r_\perp$ in comparison to hard rods due to the additional gain in internal energy when two rods come close. The difference in the relative heights of the first maxima between $g_\perp^{(7,7)}$ and $g_\perp^{(7,3)}$ arises from the fact that the attractive rod potential U_{AR} grows with the rod length. Thus, the gain in internal energy for long rods is greater than for short rods. In fact, for the chosen potential parameter $D_a = 1.15D$, the minimal interaction energy E_{min} (Eq. (2.19)) is approximately proportional to λ.

Finally, some remarks about the influence of finite-size effects. The dependence of the system size on the ordering transition of attractive rods is investigated in Fig. 3.14 (a) and (b). Part (a) displays the nematic order

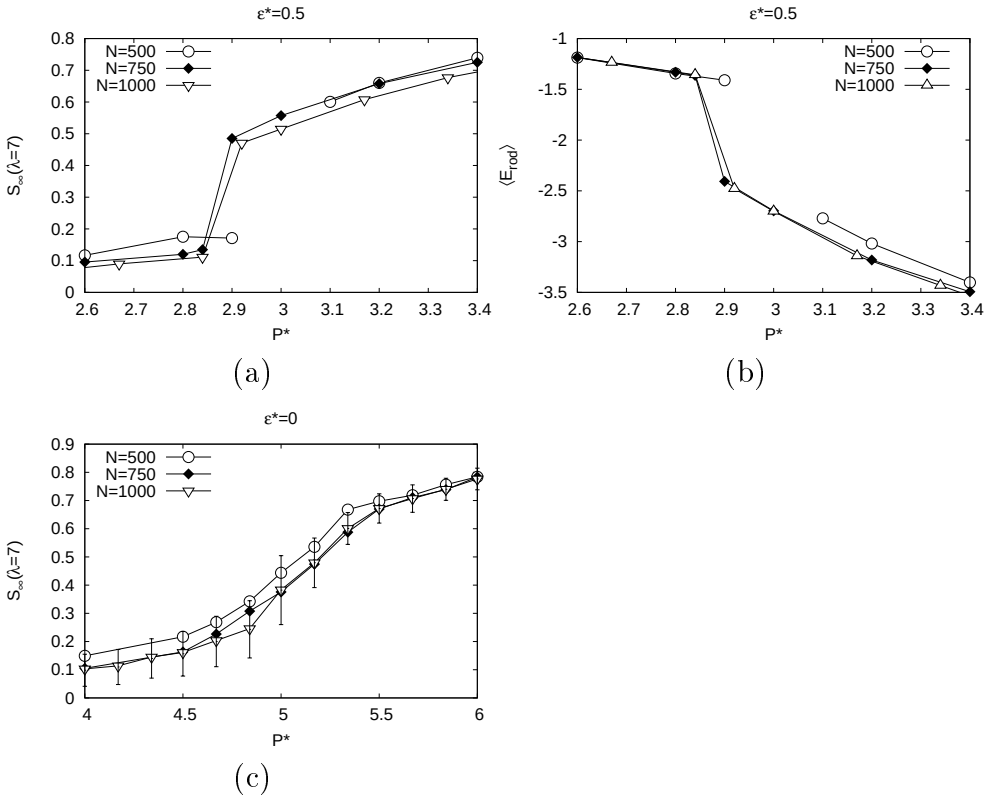

Figure 3.14: Data for systems with $N = 500$ (○), $N = 750$ (♦), and $N = 1000$ rods (▽). (a) Nematic order parameter S_∞ of the longest rods and (b) average interaction energy per rod $\langle E_{\mathrm{rod}} \rangle$ as a function of the pressure P^* for attractive rods ($\epsilon^* = 0.5$). (c) The nematic order parameter S_∞ for the longest rods as a function of the pressure for a hard rod system. In all plots, systems with $N = 750$ and $N = 1000$ rods behave almost identically.

parameter of the longest rods as a function of the pressure. The value of S_∞ in both the isotropic and in the ordered phase changes only slightly with N. Especially the systems with $N = 750$ and $N = 1000$ rods behave quite similarly. For the smallest system, finite-size effects lead to a shift of the ordering transition towards higher pressure. The data point for the $N = 500$ system at $P^* = 3$ is not drawn because no reliable average could be obtained due to several cluster formations and dissolutions during the Monte Carlo run. The shift of the ordering transition between the smallest and the two larger systems is about $\Delta P^* \approx 0.15$. Thus, one can conclude that finite-size effects are insignificant in the $N = 1000$ system. All results shown in this work are obtained from systems with $N = 1000$ or more rods. The average interaction energy per rod $\langle E_{\text{rod}} \rangle$ is depicted in Fig. 3.14 (b). The jumps in $\langle E_{\text{rod}} \rangle$ occur at the same pressures as those in S_∞. The curves of $\langle E_{\text{rod}} \rangle$ for $N = 750$ and $N = 1000$ coincide very well.

The nematic order parameter of the longest rods of a hard rod system is plotted in Fig. 3.14 (c). Again, the systems with $N = 750$ and $N = 1000$ particles behave almost identically except for some deviations at $P^* \approx 4.7$, i. e. in the region where nematic order sets in. In this region, however, the standard deviation of S_∞ is relatively large as demonstrated by the errorbars for $N = 1000$. For the system with $N = 500$ rods, S_∞ is always slightly larger except for the highly ordered state at $P^* > 5.5$. A significant shift of the ordering transition like for attractive rods is not observed.

Subsuming the results for various system sizes one can draw the conclusion that for $N = 1000$ the observed structures in the tridisperse suspension of hard and attractive rods are only subject to weak finite-size influences.

3.3 Polydisperse mixture

Most systems of synthesized colloidal rods have a polydisperse length distribution. This is a consequence of the longitudinal growth process, which has no characteristic length scale. The length of the rods is, in general, a multiple of the length of its building blocks, e. g. atoms or ligands [1]. In simulations of length-polydisperse rod systems, the rod length has to be discretized into intervals of width $\Delta\lambda$. A large $\Delta\lambda$ simplifies a λ-dependent analysis of the system whereas a small $\Delta\lambda$ might be more realistic. In practice, a compromise has to be found. Most results presented in this section are obtained for $\Delta\lambda = 1$. A smaller discretization $\Delta\lambda = 0.1$ does not change the outcome significantly as demonstrated at the end of this section.

The polydisperse system investigated here consists of rods with axis ratios $\lambda = 1, 2, \ldots, 8$. The length distribution is assumed to be fixed and chosen as

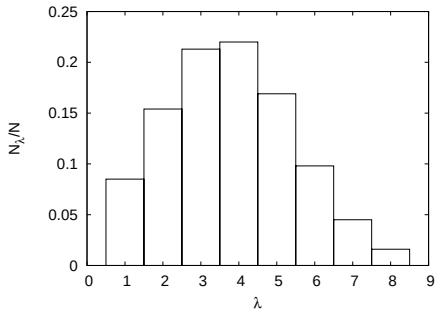

Figure 3.15: The relative number of rods N_λ/N with axis ratio λ in the polydisperse mixture.

shown in Fig. 3.15. Similar distribution functions have been measured, for example, in solutions of amyloid fibrils [69] or suspensions of clay rods [105].

Results for S_∞ are presented in Fig. 3.16 for various interaction strengths ϵ^*. In addition to hard rods ($\epsilon^* = 0$) and attractive rods with $\epsilon^* = 0.5$, rods with interaction strengths $\epsilon^* = 0.25$ and $\epsilon^* = 0.33$ are studied.

The qualitative properties of the curves in Fig. 3.16 are very similar to those of the tridisperse mixture discussed in Section 3.2. For all polydisperse systems, the nematic order apportioned by components increases with the length of the rods. At low pressures, the system is isotropic and S_∞ is close to zero for all rod lengths. At high pressures, $S_\infty \geq 0.8$ is found for rods with axis ratio $\lambda = 7$ and $\lambda = 8$, while short rods are distinctly less ordered.

The system with the largest interaction strength $\epsilon^* = 0.5$ is analyzed in Fig. 3.16 (a). Below $P^* = 3$, all components show hardly any orientational order. At $P^* = 3$, a jump can be seen in S_∞ for the two longest constituents. For intermediate axis ratios ($\lambda \in \{5, 6\}$), S_∞ grows almost linearly with P^* for $P^* > 3$ while short rods remain mostly isotropic.

For lower interaction strengths ϵ^*, considerable orientational order sets in at higher pressure and the step-like increase of S_∞ for the longest rods becomes rather continuous. At high pressures, the system is less clearly divided into long rods with essential orientational order and short rods with almost no orientational order. Instead, for the hard rod limit, S_∞ increases almost linearly with λ and, at high pressures, even rods of axis ratio 2 show a distinct nematic order.

Fig. 3.17 shows typical configurations of ordered systems with (a) $\epsilon^* = 0.5$ and (b) $\epsilon^* = 0$. For the sake of clearness small rods with axis ratios $\lambda \leq 5$ are omitted. In Fig. 3.17 (a), a highly ordered monolayer is visible in the middle of the box. As will be demonstrated below, the layer is ordered hexatically. In

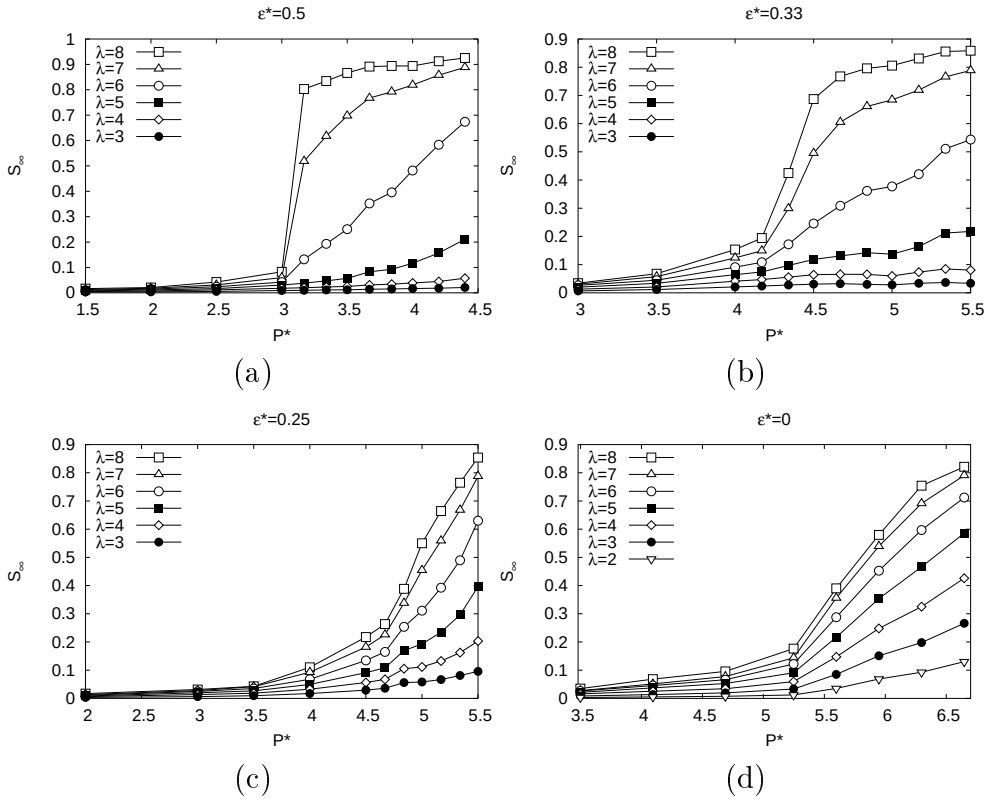

Figure 3.16: The orientational order parameter S_∞ as a function of the pressure P^* determined for every component with axis ratio λ in systems with interaction strength (a) $\epsilon^* = 0.5$, (b) $\epsilon^* = 0.33$, (c) $\epsilon^* = 0.25$, and (d) $\epsilon^* = 0$. The system with $\epsilon^* = 0$ corresponds to the hard rod model.

Fig. 3.17 (b), long hard rods form a nematic droplet, which is less marked off from the surrounding system. Note that the formation of a nematic droplet has not been observed in Section 3.2. This is the most significant difference compared to the tridisperse mixture.

One may assume that the formation of the monolayer is a finite-size effect. However, similar monolayers have been observed in experiments with attractive rods, where they turn out to be extremely long-living configurations [22]. In the hard rod system, a nematic droplet is formed by predominantly long rods. Long-living nematic domains of the size of several rod lengths are also found experimentally [22]. Because of the surface energy at the droplet interface, the formation of ordered domains may be shifted towards higher pressures in the chosen ensemble.

The hexatic order of the cluster as well as fractionation are reflected in

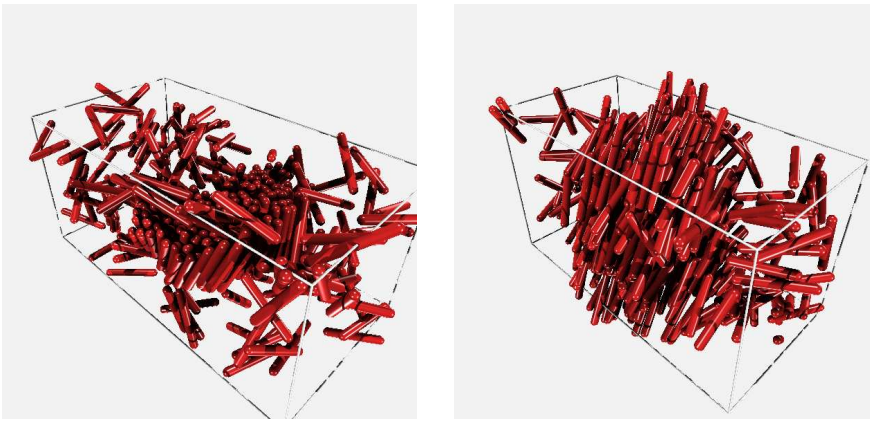

(a) (b)

Figure 3.17: Typical ordered configurations of (a) attractive rods ($\epsilon^* = 0.5$) at pressure $P^* = 3.5$ and (b) hard rods at pressure $P^* = 6.3$. For clarity, short rods ($\lambda \leq 5$) are omitted.

the pair correlation functions. A good insight into the system is provided by $g_{\parallel}^{(6,\lambda)}$ and $g_{\perp}^{(6,\lambda)}$, which analyze the local density of rods with an axis ratio λ around reference rods with an axis ratio 6. The isotropic structure of the system at low pressure is confirmed in Fig. 3.18 (a) and (b). They show pair correlations between rods with axis ratio $\lambda_{\text{ref}} = 6$ and other rods, which are typical for an isotropic state (cmp. Fig. 3.4 (a) and (b)). Fig. 3.18 (c) and (d) shows pair correlation functions for a highly ordered system with $\epsilon^* = 0.5$ and $P^* = 3.84$. Correlations with long rods (represented by $g_{\perp}^{(6,8)}$ (– – –) and $g_{\perp}^{(6,6)}$ (—)) show a double peak pattern, which indicates hexatic order while correlations with smaller rods, represented by $g_{\perp}^{(6,4)}$ (–·–·), have the weakly structured curve of an isotropic state. These observations can be explained as follows: Systems with $\epsilon^* = 0.5$ at high pressure form a hexatic monolayer of predominantly long rods in coexistence with an isotropic system of short rods. A large fraction of the rods with axis ratio $\lambda_{\text{ref}} = 6$ is included in the monolayer while the rest is located in the isotropic part of the system. Contributions to $g_{\perp}^{(6,\lambda)}$ for large λ stem predominantly from reference rods inside the monolayer while the remaining rods of length $\lambda_{\text{ref}} = 6$ are surrounded by an isotropic system of small rods. For the same reason, $g_{||}^{(6,\lambda)}$ is comparable to the isotropic curves for $\lambda = 4$ while for large λ, $g_{||}^{(6,\lambda)}$ grows extremely slowly towards 1 with increasing $r_{||}$, since almost all long rods are located transversely.

In Fig. 3.19 (a)-(c), the growth of the hexatic monolayer is documented

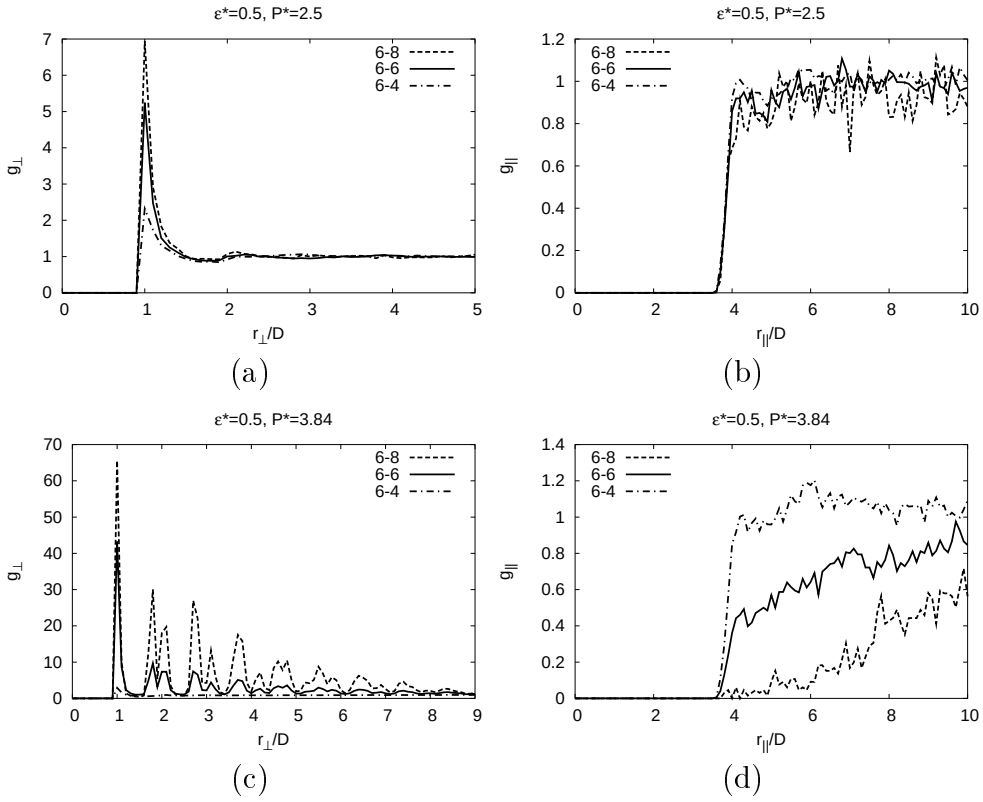

Figure 3.18: (a) Transversal pair correlation function $g_\perp(r_\perp)$ and (b) longitudinal pair correlation function $g_{||}(r_{||})$ in a system of attractive rods ($\epsilon^* = 0.5$) in the isotropic state at pressure $P^* = 2.5$. (c) $g_\perp(r_\perp)$ and (d) $g_{||}(r_{||})$ in the ordered state at pressure $P^* = 3.84$. The double peak pattern in (c) is characteristic for long-range hexatic order.

for $\epsilon^* = 0.33$ and various pressure values. At $P^* = 4.17$, the system is predominantly isotropic, but small clusters of long rods have formed, yet. The shoulder of the second peak of $g_\perp^{(6,8)}$ (▬▬) already hints at the formation of a hexatic ordering, which becomes clearly visible from the double-peak at $P^* = 4.34$. The hexatic monolayer has formed completely at $P^* = 4.84$. Altogether, an increasing pressure leads to the growth of a highly ordered monolayer made up predominantly by long rods. This results in a rise of the overall order parameter S_∞ for large rod lengths in Fig. 3.16. In Fig. 3.19 (d), $g_\perp^{(6,\lambda)}$ is shown for a hard rod system at a high pressure. Here, no hexatic order exists and, consequently, no double peaks are visible.

The local fractionation in the system can be measured directly from $\langle\lambda\rangle_{\mathrm{ngb}}(\lambda_{\mathrm{ref}})$, which is defined as the average axis ratio of the 36 nearest neigh-

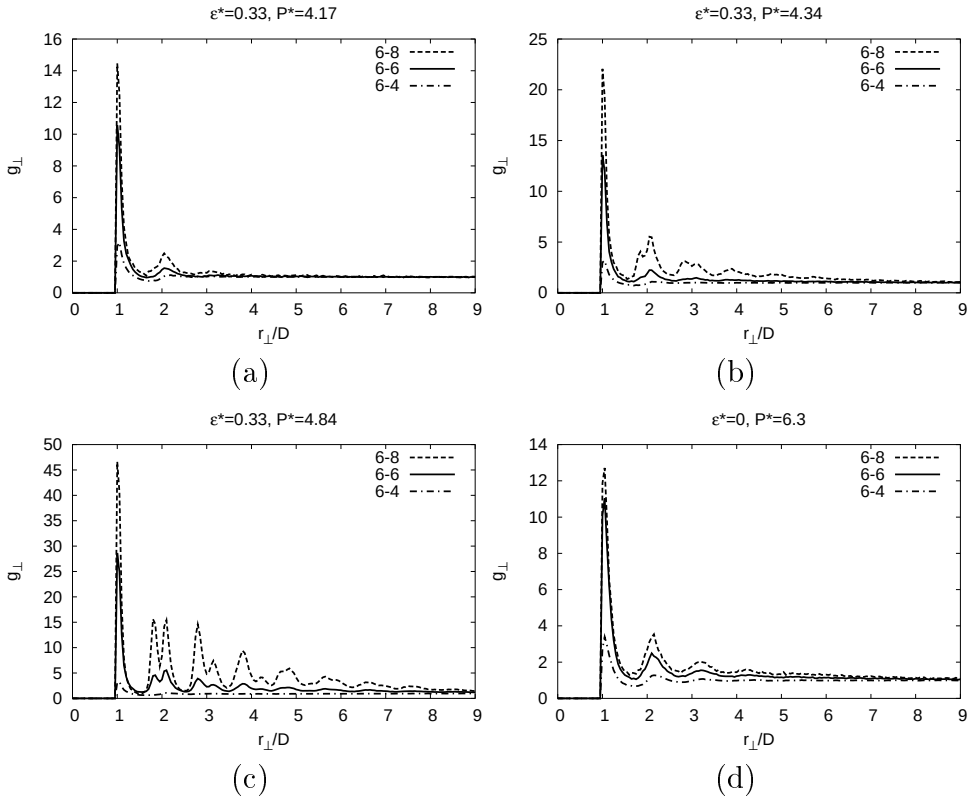

Figure 3.19: (a)-(c) Transversal pair correlation function $g_\perp(r_\perp)$ for attractive rods with $\epsilon = 0.33$ (a) at $P^* = 4.17$, (b) at $P^* = 4.34$, and (c) at $P^* = 4.84$. The second maximum in (a) vaguely indicates a double peak structure, which becomes more pronounced at higher pressures. (d) Transversal pair correlation function $g_\perp(r_\perp)$ of a hard rod system in the ordered phase at $P^* = 6.3$.

bors of reference rods with axis ratio $\lambda_{\rm ref}$. (In a perfect hexatic monolayer, a rod i has 36 neighboring rods j with $r_{ij} < 3D$.) In Fig. 3.20, $\langle\lambda\rangle_{\rm ngb}$ is presented as a function of $\lambda_{\rm ref}$. In the isotropic state (□), $\langle\lambda\rangle_{\rm ngb}$ is nearly constant, which implies that long and short rods are surrounded by rods of the same average length. The solid symbols in Fig. 3.20 show $\langle\lambda\rangle_{\rm ngb}$ for highly ordered phases with different interaction strengths at pressures, for which the orientational order for $\lambda = 7$ is approximately $S_\infty \approx 0.7$. In the ordered states, short rods are preferentially surrounded by rods of small length while rods with a large axis ratio accumulate long rods. The separation of long rods increases with the size of ϵ^*, showing that fractionation is enhanced by the attractive interaction of the rods.

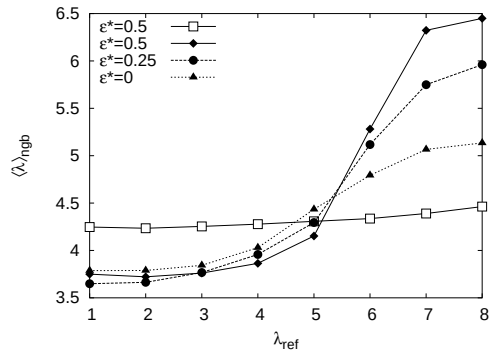

Figure 3.20: Average axis ratios $\langle\lambda\rangle_{\mathsf{ngb}}$ of the 36 closest neighbors of reference rods with axis ratio λ_{ref}. Shown are results for an isotropic system with $\epsilon^* = 0.5$, $P^* = 1.5$ (□) and ordered systems with $S_\infty^{\lambda=7} \approx 0.7$, obtained by $\epsilon^* = 0.5$ at $P^* = 4.0$ (♦), $\epsilon^* = 0.25$ at $P^* = 5.5$ (●) and $\epsilon^* = 0$ at $P^* = 6.64$ (▲).

A polydisperse suspension with a length distribution of the same shape as that in Fig. 3.15, but $\Delta\lambda = 0.1$ is studied in the following. Fig. 3.21 (a) shows the corresponding length distribution. The behavior of the nematic

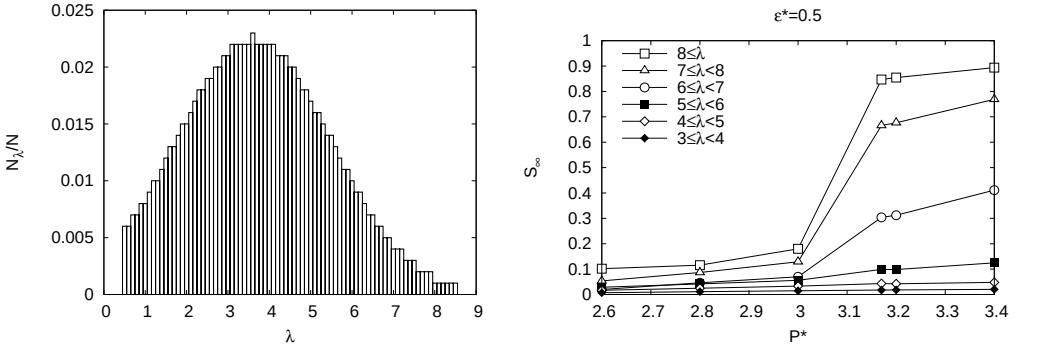

(a) (b)

Figure 3.21: (a) The length distribution of the polydisperse mixture with a higher resolution of the axis ratio λ. (b) Nematic order parameter S_∞ as a function of the pressure P^* in the mixture of attractive rods with $\Delta\lambda = 0.1$.

order parameter of the mixture with $\Delta\lambda = 0.1$ is presented in Fig. 3.21 (b). Differences from the mixture with $\Delta\lambda = 1$ shown in Fig. 3.16 (a) appear to be marginal. S_∞ jumps for rods with $8 \leq \lambda$ and $7 \leq \lambda < 8$ from a small to a large value between $P^* = 3$ and $P^* = 3.17$. Intermediate rod lengths $6 \leq \lambda < 7$ participate partially in the ordering process whereas shorter rods remain

isotropic at $P^* \geq 3.17$. It is remarkable that the ordering transition occurs exactly in the same pressure region as for the mixture with $\Delta\lambda = 1$, i. e. between $P^* = 3.0$ and $P^* = 3.17$. One can conclude that the polydisperse mixture with axis ratios restricted to integer values resembles mixtures with continuous axis ratios in most aspects, at least for the applied parameter range.

Chapter 4

Substrate induced effects

The structure of fluids, especially of complex fluids, can be affected significantly in the vicinity of a wall like the confining walls of the container. From a technical point of view, two adjacent walls can be realized easily in computer simulations. For not too large wall separations, the described geometry is a slit pore and a variety of studies focused on complex fluids in slit pores [23, 32, 37, 63, 79, 98]. The influence of a single confining wall can be investigated either for very large wall separations or with special simulation techniques [21]. In order to avoid the additional costs of the method described in [21] two plane parallel walls with large separations are simulated with the mirroring technique introduced in Section 2.4.2. It turns out that wall induced correlations decay relatively fast with increasing distance from the wall in mixtures of length-polydisperse rods and thus the fluid behavior near one wall is not influenced by the other wall.

The structure of the confining walls has great relevance on the fluid properties. We check the impact of the three different substrate patterns sketched in Fig. 4.1. The planar wall does not break any symmetry in the xy-plane. The groove pattern is translational invariant along the x-direction. It is characterized by the depth z_C and the width y_C of the grooves. The translational invariance of the corrugated substrate is broken in a cavity pattern. The rectangular cavities have depth z_C, width y_C, and length x_C. Results are compared for grooves that vary in y_C and cavities that differ in x_C.

4.1 Tridisperse suspension

This section copes the behavior of the tridisperse mixture in the vicinity of a substrate. The pressures, which are investigated in detail, are $P^* = 0.5$ and $P^* = 4$ and are below the regime where a corresponding bulk system

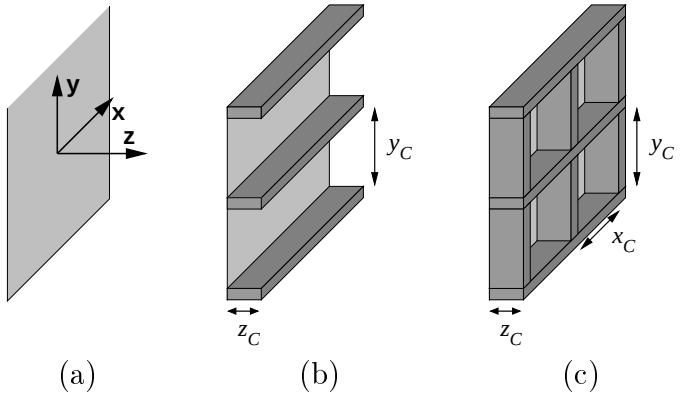

Figure 4.1: Illustrations of the three investigated substrate types. (a) Planar wall, (b) corrugated wall (grooves), and (c) cavity pattern.

of hard rods becomes anisotropic (cmp. Fig. 3.6 (b) on page 44). We call $P^* = 0.5$ low pressure and $P^* = 4$ high pressure. The emphasis lies on hard rod systems since most interesting effects are observed at $P^* \approx 4$, for which bulk systems of attractive rods show a pronounced structure formation and fractionation, already. Here, we focus on substrate induced structure formation and attractive rod systems are thus of minor interest. For comparison, some studies are performed with attractive rods. In these cases, interactions of rods with the substrate are purely repulsive as for the hard rod system.

The structure of the systems is analyzed in terms of density distribution functions and orientational correlation functions as introduced in Section 2.5.3 and Section 2.5.5. The properties of the various substrate patterns concerning demixing and fractionation are investigated in terms of the spatially resolved mole fraction (see Sec. 2.5.4).

4.1.1 Planar substrate

The planar wall is examined first. Fig. 4.2 displays the density profile of each component of a hard rod system at low and high pressure. Part (a) shows the results for $P^* = 0.5$. The substrate is located at $|z - z_0| = 0$ for all plots. The density profiles of long (▬ ▬), intermediate (▬), and short rods (▬·▬·) exhibit a maximum at $|z - z_0|/D = (\lambda + 1)/2$. At the respective distance from the substrate, the orientational degrees of freedom are no longer restricted by the substrate. The maximum in the density is actually a depletion effect because an unaccessible void is created if a rod with orientation parallel to the wall normal is located at separations slightly larger than $|z - z_0|/D = (\lambda + 1)/2$. Similar observations were already

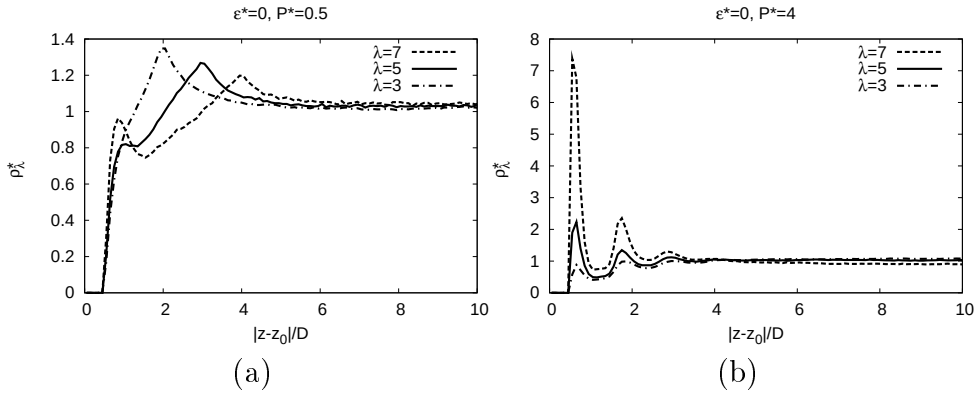

Figure 4.2: Density distribution ρ_λ^* as a function of the distance to the wall $|z-z_0|$ of the tridisperse hard rod suspension in contact with a planar substrate. The single component densities are plotted (a) at low pressure and (b) at high pressure.

described in Section 3.2 where the corresponding peaks in $g_\perp$ arose from so called '|−' constellations. In the following, the notation is adopted with '||' symbolizing a rod, which adheres flat on the substrate, and '|−' indicates a rod, which is perpendicular to the wall at distance $|z - z_0|/D = (\lambda + 1)/2$. The density distribution of the long rods (▬▬) shows a small maximum at $|z - z_0| \approx 0.7D$ but is distinctly reduced in the range $1.2 < |z - z_0|/D < 2.5$. Apparently, long rods either contact the substrate at full length or stay away from the substrate far enough so that rotations are not strongly hindered by the substrate.

Part (b) of Fig. 4.2 depicts the same distribution functions at $P^* = 4$. The structure of the fluid is changed significantly. The maxima from '|−' configurations disappear and several layers of rods, which are aligned parallel to the substrate, are formed all separated by about one rod diameter. The height of the peaks increases with the rod length. It is more favorable for the system to deposit long rods at the substrate for entropic reasons. The explanation is as follows: Assume a long rod is taken from the bulk, i. e. far away from the substrate and is adhered at the substrate. The orientational degrees of freedom of the rod are reduced but at the same time more free volume is accessible to the rest of the rods in the bulk. If, on the contrary, two short rods with the same overall length as the long rod are taken from the bulk and adhered at the wall, more rotational entropy gets lost, but the gain in accessible volume is comparable. Thus, a pronounced segregation of long rods at the substrate is observed.

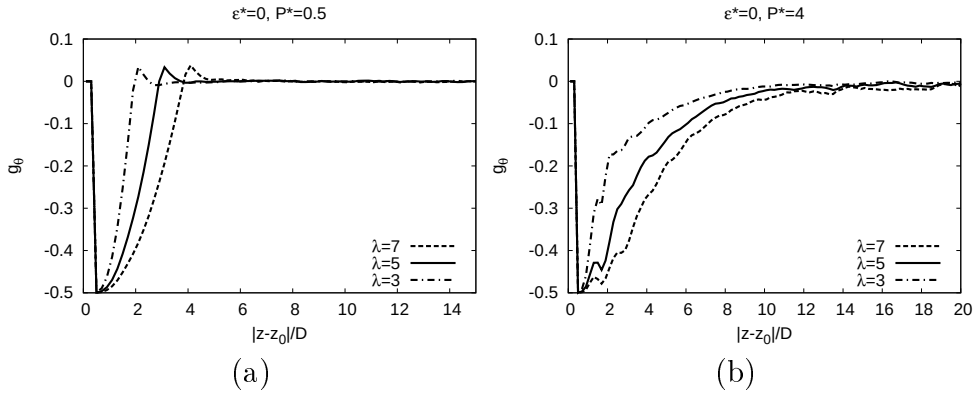

Figure 4.3: The orientational distribution function g_θ as a function of the distance $|z - z_0|$ to the wall in a system of hard rods in contact with a planar substrate at (a) low and (b) high pressure.

The orientational correlation function g_θ is plotted in Fig. 4.3 at low and high pressure. Some properties of g_θ are recalled quickly: g_θ is the z-dependence of the nematic order parameter with the director $\mathbf{n}$ parallel to the z-axis $\mathbf{e}_z$. The codomain comprises the interval $[-0.5, 1]$, where the lower bound is adopted by rods perpendicular to $\mathbf{e}_z$ and the upper bound is reached when all rods are parallel to the z-direction. g_θ vanishes for an isotropic distribution. The low pressure results for g_θ are depicted in Fig. 4.3 (a). g_θ is minimal (and negative) at $|z - z_0| = 0.5D$ for all rod lengths since rods proximate to the substrate have to orient parallel to the substrate and thus perpendicular to $\mathbf{e}_z$. Each curve adopts its maximal value at $|z - z_0|/D = (\lambda+1)/2$, which is in perfect agreement to the observations from the density distribution functions, where the corresponding peaks were addressed to '$|-$' constellations. At larger distances from the wall, g_θ is identically zero reflecting the isotropic state of the system. Fig. 4.3 (b) shows g_θ in the high pressure regime. The layer formation close to the wall is confirmed by 2-3 minima in g_θ whereas indications for '$|-$' configurations are absent. With increasing distance from the substrate, the correlations decay[1], but much slower than at low pressure. The correlations of long rods decay slowest. g_θ is around zero at large separations from the wall ($|z-z_0| \gtrsim 13D$). Orientational correlations range distinctly longer than correlations of the density (Fig. 4.2 (b)). The extension of the simulation box comprises $20D$ in z-direction[2].

[1] A decay of correlations in this case is related to an increase of g_θ, if $g_\theta < 0$.

[2] Note that the effective wall separation is $40D$ due to the applied mirroring simulation technique.

Thus, artefacts from the finite box dimensions should be small.

The evolution of the density profile for the tridisperse system at compression is studied in more detail in Fig. 4.4. Data for the short rods is presented

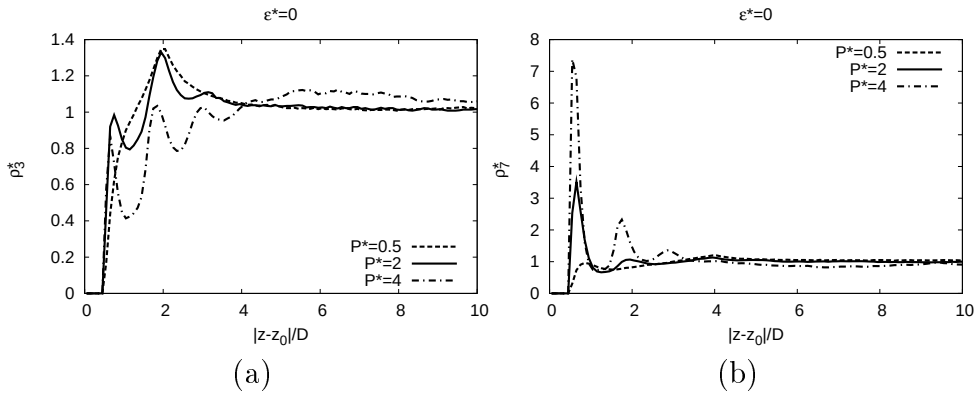

Figure 4.4: Density distribution ρ_λ^* as a function of the distance $|z - z_0|$ to the wall of the tridisperse hard rod system in contact with a planar substrate for (a) small rods ($\lambda = 3$) and (b) long rods ($\lambda = 7$) at different pressures.

in part (a). The low pressure results (▬▬) were already discussed above. At intermediate pressure (—) significancies from '||' and '|−' constellations are present. The multilayer structure at high pressure (▬·▬·) is reflected in ρ_3^* by several maxima separated by $1D$. Indications for '|−' configurations are absent. It is noteworthy that the density of short rods in the layers is smaller than in the bulk. The density profile of long rods is displayed in Fig. 4.4 (b). The curves for $P^* = 0.5$ and $P^* = 4$ have already been described. At $P^* = 2$, one distinct maximum from rods flat on the substrate is observed. There are also indications for a second layer at $|z - z_0| \approx 1.8D$ and for '|−' configurations at $|z - z_0| \approx 4D$.

Hard and attractive rod systems are compared in Fig. 4.5. Note that the rod-substrate interaction is purely repulsive in both cases. Results for the low pressure regime are plotted in Fig. 4.5 (a) and (b). The density profiles of short rods are almost identical (Fig. 4.5 (a)). The density distribution function of large rods deviates slightly at the first maximum that stems from rods lying flat on the substrate but is identical else. One observes that ρ_7^* of hard rods (▬▬) is somewhat larger than ρ_7^* of attractive rods (—) at $|z - z_0| \approx 0.7D$. This effect can be explained as follows: Imagine an isotropic system of attractive rods. A rod in the bulk experiences attractive interactions from all directions. If one rod is taken from the bulk and placed flat onto the (hard) substrate, it is screened from attractive interactions on

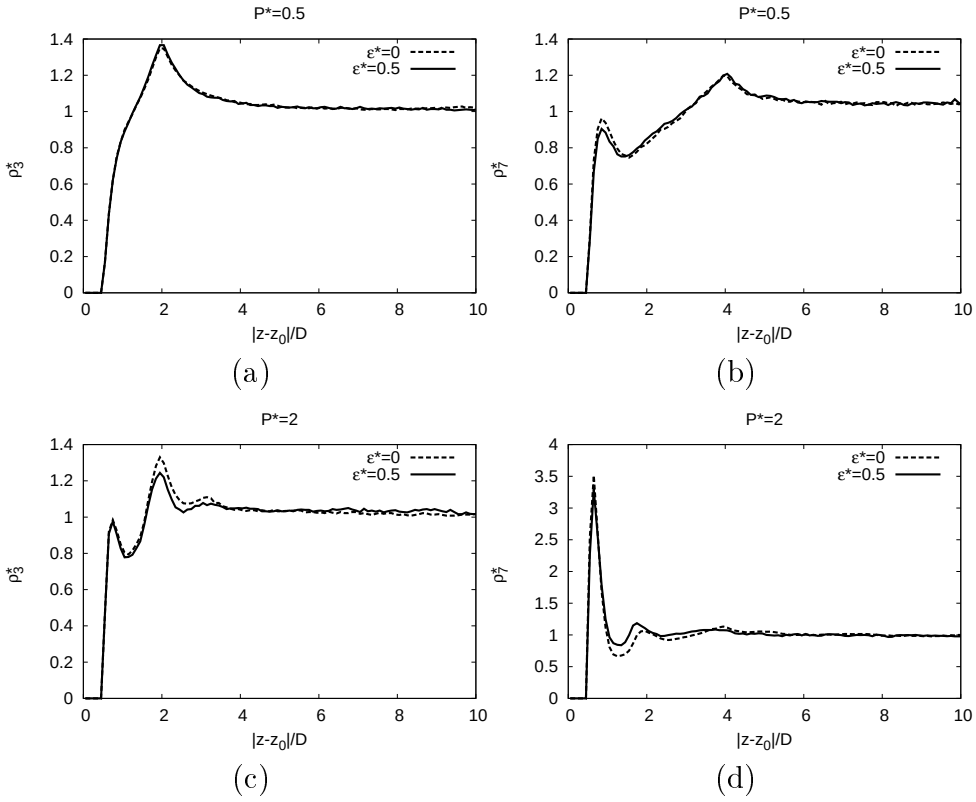

Figure 4.5: Comparison of hard (– – –) and attractive rods (—). Density profiles as a function of the distance $|z - z_0|$ to the wall in the low pressure regime ($P^* = 0.5$) for (a) short and (b) long rods. Corresponding plots are shown in (c) and (d) for an intermediate pressure ($P^* = 2$).

the substrate side. As a result, the internal energy of the system increases and the corresponding configuration is slightly less favorable.

The same effect occurs in the intermediate pressure regime as demonstrated in Fig. 4.5 (d). The density of long hard rods (– – –) in the first layer is increased with respect to attractive rods (—). The second layer, however, is more pronounced for attractive rods and the maximum is shifted towards the substrate. Short rods are compared in Fig. 4.5 (c). The two curves agree to a large extent but deviate at the second maximum, which is due to '|−' configurations, with the density of hard rods being larger. Obviously, there is more accessible volume for short hard rods than for short attractive rods at $|z - z_0| \approx 2D$ since ρ_7^* exhibits the reverse behavior in this region.

The spatially resolved nematic order parameter S_∞ is plotted in Fig. 4.6 for hard rods. The order at the substrate is substantially larger than in the

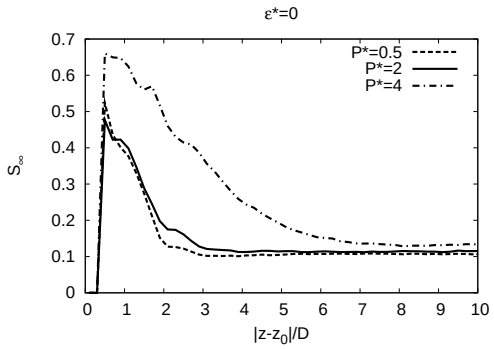

Figure 4.6: Nematic order parameter S_∞ as a function of the distance $|z-z_0|$ to the wall of hard rod systems at low (▬▬), intermediate (—), and large (▬·▬·) pressure.

bulk for all considered pressures. At $P^* = 0.5$ (▬▬) and $P^* = 2$ (—), order decays rapidly with increasing $|z - z_0|$ and adopts the bulk value at $|z - z_0| \geq 3D$. The value of S_∞ proximate to the wall is quite similar. In the high pressure region (▬·▬·), nematic order is distinctly larger and ranges much further into the bulk. S_∞ is about 50% of its maximal value at $|z - z_0| = 3D$ where the systems with lower pressures have already reached the bulk value.

The investigations of the tridisperse suspension in contact with a planar wall are finalized by two pictures of typical rod configurations at low and high pressure in Fig. 4.7. Part (a) corresponds to the low pressure situation. The substrate is the big area in front. The system is basically isotropic and no obvious coverage of the substrate is visible. At high pressure, the substrate is preferentially covered by long rods.

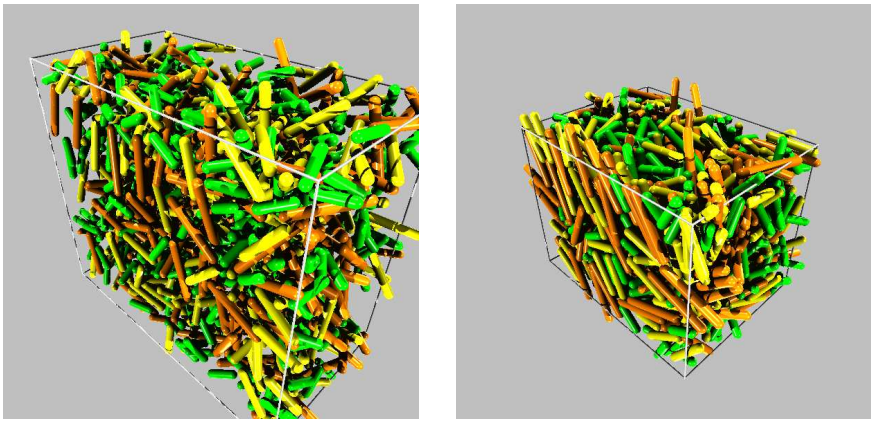

(a) $P^* = 0.5$ (b) $P^* = 4$

Figure 4.7: Snapshots of hard rod systems in contact with a planar substrate (a) in the low pressure and (b) in the high pressure region. The substrate is located at the front plane of the box.

4.1.2 Corrugated substrate

The second investigated substrate type is a groove-like structure. The pattern is composed of a planar wall located at $|z - z_0| = 0$ with equally-spaced side walls on top. The side walls consist of stacks of infinitely long cylinders oriented along the x-axis. The depth of the grooves is $z_C = 4D$ for all data presented here, i. e. each side wall of a groove consists of 4 cylinders of diameter D stacked on top of each other (see Fig. 4.8 (d)). Fig. 4.8 shows density profiles for grooves of width $y_C = 3.5D$ at different pressures. For a low pressure, short (▬·▬·) and intermediate rods (▬) are mainly homeotropic inside the grooves as the peaks at $|z - z_0| = 2D$ and $|z - z_0| = 3D$ in Fig. 4.8 (a) reveal. Interestingly, long rods (▬▬) do not form a layer flat on the substrate as this is the case for the planar wall. The side walls of the grooves restrict the orientational degrees of freedom in the xy-plane. This influence is apparently enough to suppress the layer formation. Note that at $P^* = 0.5$ and for a groove width of $y_C = 3.5D$ the density of short rods is largest inside the grooves. At further distances from the substrate, three small peaks are observed located at $|z - z_0|/D \approx z_C + (\lambda + 1)/2$ for all rod lengths. At the respective positions the corresponding rods are no longer directly affected by the substrate structure.

At a slightly higher pressure $P^* = 1$, we find a distinct change of ρ_7^* and ρ_5^* inside the grooves as demonstrated in Fig. 4.8 (b). The density of long rods (▬▬) is maximal at $|z - z_0| \approx 0.8D$ and a second layer is indicated weakly.

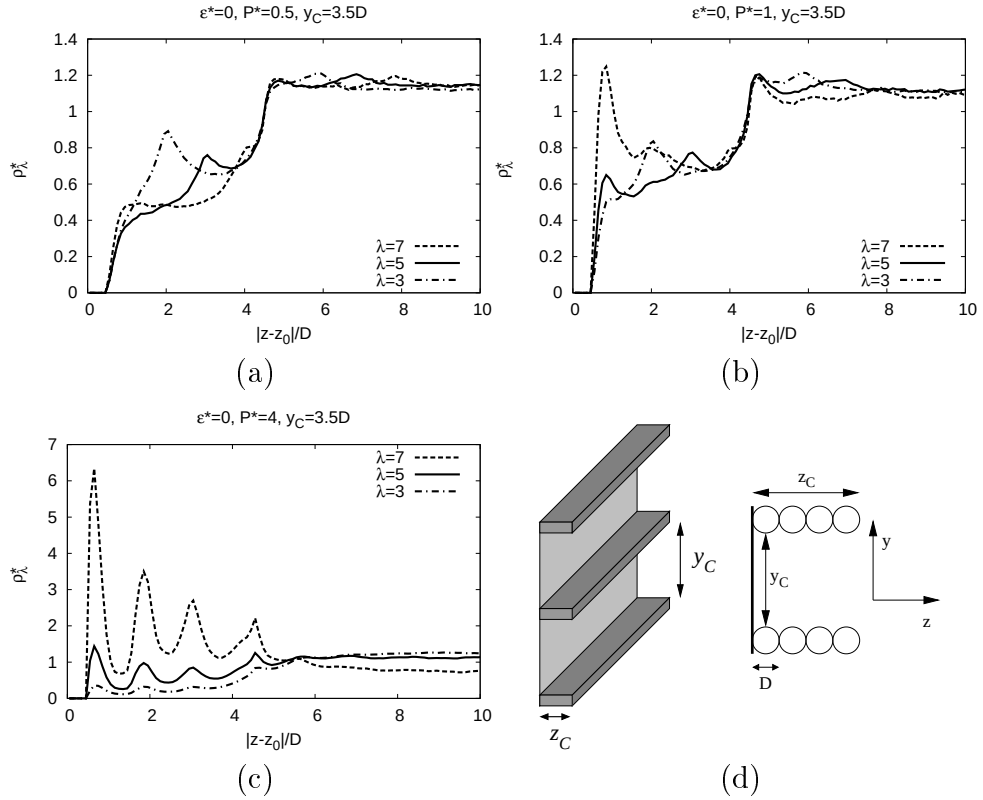

Figure 4.8: (a)-(c) Density profiles ρ_λ^* as a function of the distance $|z - z_0|$ to the wall of hard rod systems in contact with a substrate with grooves of width $y_C = 3.5D$ at the pressure (a) $P^* = 0.5$, (b) $P^* = 1$, and (c) $P^* = 4$. (d) Illustration of the substrate with grooves. Each side wall is composed of four cylinders of diameter D.

Rods of intermediate length (—) exhibit an additional peak in the density from '||' configurations. The density profile of short rods (-·-·-) remains basically unchanged.

The density distribution functions in the high pressure regime are plotted in Fig. 4.8 (c). Four pronounced maxima of ρ_7^* are observed with the first three peaks inside and the fourth peak on top of the grooves. The density of shorter rods is reduced significantly in the grooves with ρ_5^* being about 25% of ρ_7^*. The density of $\lambda = 3$ rods inside the grooves is about 20% of the bulk value.

The structure of the system is elucidated further via the orientational correlation functions g_θ and g_ϕ (see Section 2.5.5) in Fig. 4.9. Part (a) depicts g_θ at low pressure ($P^* = 0.5$). The values of g_θ at the peaks from

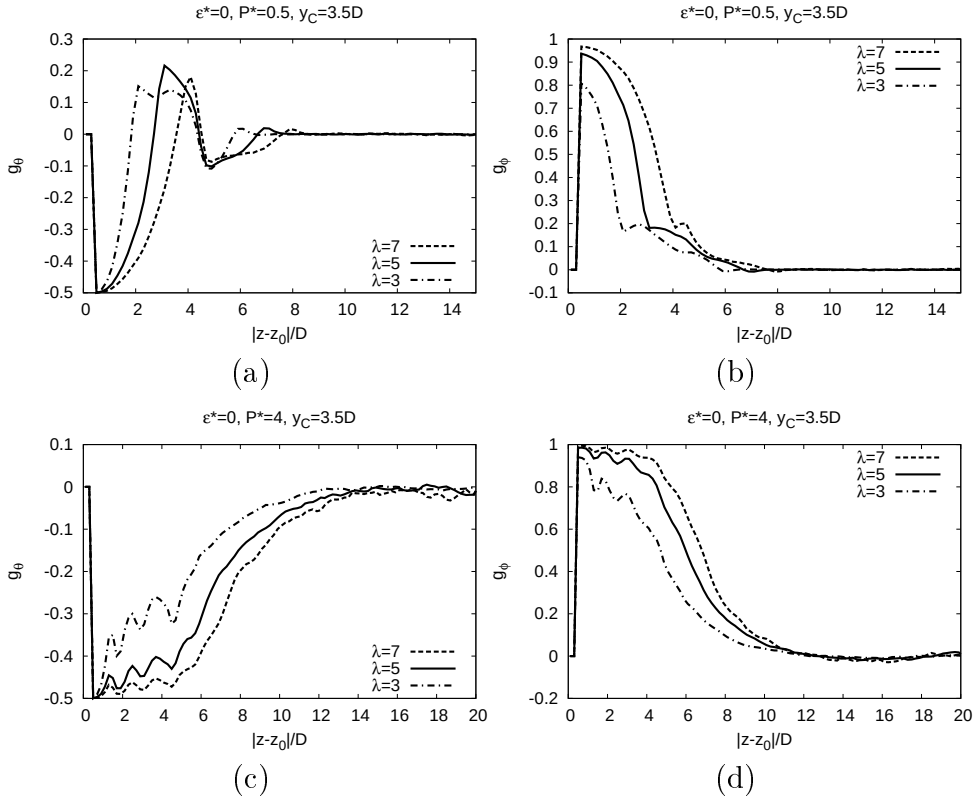

Figure 4.9: Orientational correlation functions g_θ and g_ϕ as a function of the distance $|z - z_0|$ to the wall of a tridisperse hard rod mixture in front of a substrate with broad grooves ($y_C = 3.5D$). Results are presented for the low pressure regime ((a) and (b)) and for the high pressure regime ((c) and (d)).

the '|−' configurations are measurably larger than in the case of the planar wall because the orientations are focused more in z-direction by the grooves. In addition to the minimum inside the grooves, a second weaker minimum occurs at $|z - z_0| \approx 4.7D$ from rods flat on top of the grooves. The range of the correlations induced by the groove pattern exceeds the range of the correlations for the planar wall very precisely by the depth $z_C = 4D$ of the grooves.

The orientational correlations in x-direction measured by g_ϕ are plotted in Fig. 4.9 (b). g_ϕ is maximal at the substrate for all rod lengths and decays quickly with increasing $|z-z_0|$. g_ϕ decreases particularly fast when $|z-z_0|/D$ approaches $(\lambda + 1)/2$ and meets in a sharp bend, an effect which is related to the preferred occurrence of '|−' configurations. Orientational correlations in x-direction vanish at separations $|z - z_0| \geq 8D$.

The layer formation inside the grooves at high pressure is also reflected in g_θ and g_ϕ as shown in Fig. 4.9 (c) and (d). Maxima of the local density are accompanied by strong orientational order parallel to the x-direction so that g_θ and g_ϕ adopt a local minimum or maximum, respectively. Note that perfect alignment perpedicular to the z-axis corresponds to $g_\theta = -0.5$. Both correlation functions are basically zero for $|z - z_0| \geq 15D$.

Density distribution functions for narrow grooves of width $y_C = 1.5D$ in the low and high pressure regime are presented in Fig. 4.10. The essential

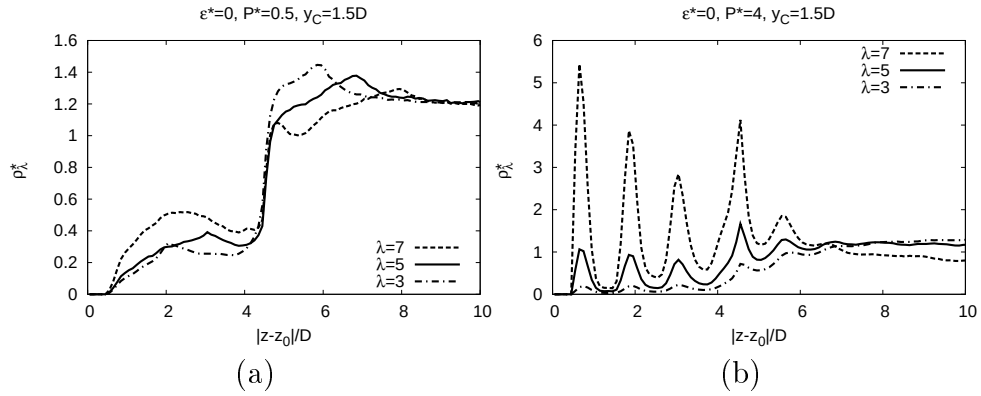

Figure 4.10: Density distribution ρ^*_λ as a function of the distance $|z - z_0|$ to the wall of a hard rod system in contact with a corrugated substrate with narrow grooves ($y_C = 1.5D$) at (a) low and (b) high pressure. At low pressure, the density of long rods is largest inside the grooves in contrast to the case of broad grooves (Fig. 4.8 (a)).

new aspect of the narrow grooves compared to the broader grooves of width $y_C = 3.5D$ is the fact that now the orientation space of *all* rods is strongly reduced inside the grooves. Especially at low pressure this effect comes into play as shown in part (a) of Fig. 4.10. The density of short and intermediate rods is distinctly lower than for the broad grooves but the maxima from '|−' configurations remain. Long rods possess the largest density due to the reduction of shorter rods. The value of ρ^*_7, however, does not change much compared to the broader grooves. The qualitative behavior of the density distribution for $|z - z_0| \geq 4D$ is quite similar to that of a density distribution function in front of a planar wall located at $|z - z_0| = 4D$ (cmp. Fig. 4.2 (a)): The density is maximal for all rod lengths at distances where orientations are no longer affected by the substrate. Only the longest rods form a weak layer flat on top of the wall/grooves and ρ^*_7 lowers measurably between the maxima from '||' and '|−' constellations. Obviously, narrow grooves act almost like a

planar substrate for rods that are not inside the grooves.

Fig. 4.10 (b) depicts curves in the high pressure regime. Multiple layers are found inside the grooves, again. The values of the different ρ^*_λ at the peaks as well as their ratios are comparable to the broader grooves. The density between the layers, i. e. in the minima, reduces distinctly, however. The density profiles on top of the grooves differ significantly from the broad grooves, especially for $\lambda = 7$ and $\lambda = 5$ rods. Two peaks occur in ρ^*_7 and ρ^*_5. The value of ρ^*_7 at $|z - z_0| \approx 4.7D$ is about twice as large as for broad grooves and the correlations imposed by the narrow grooves range further into the bulk.

Typical rod configurations at high pressure are drawn in Fig. 4.11 for both broad and narrow grooves. The view is along the z-axis and the planar

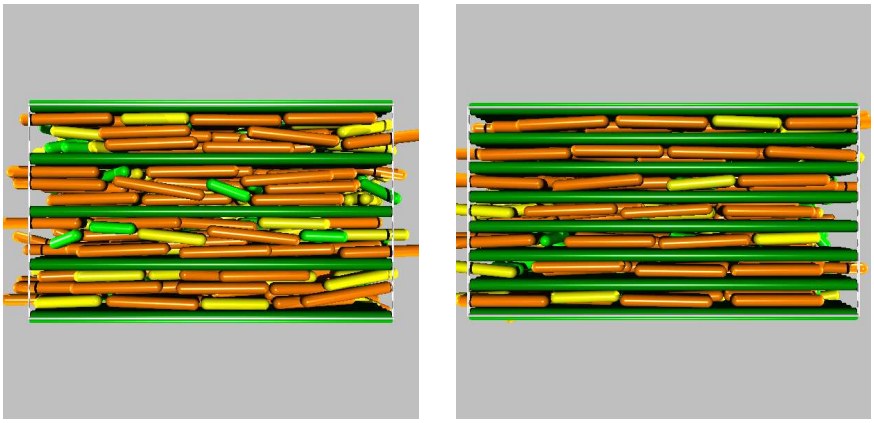

(a) $P^* = 4$, $y_C = 3.5D$ (b) $P^* = 4$, $y_C = 1.5D$

Figure 4.11: Snapshots of the tridisperse hard rod suspension in contact with a substrate with (a) broad and (b) narrow grooves at high pressure.

wall is transparent. The side walls of the grooves are made up of infinitely long cylinders, which are colored green in the snapshots.

Before we turn to the next substrate pattern, here comes a brief summary of the results for the grooves: We investigated a tridisperse mixture of hard rods in contact with a substrate with broad and narrow grooves. The systems were studied at low ($P^* = 0.5$) and high ($P^* = 4$) pressure. In the low pressure regime, the density of small rods is largest in the broad grooves whereas for narrow grooves the density of long rods dominates. At high pressure, multiple layers of predominantly long rods build in the grooves.

4.1.3 Cavity pattern

The third type of studied substrate patterns has a rectangular cavity structure formed by a set of side walls in x- and y-direction on top of the hard plane at $|z-z_0| = 0$ (see Fig. 4.12 (d)). All cavities have a width $y_C = 3.5D$. The depth is chosen $z_C = 4D$ throughout this section. In the following four different lengths of the cavities are investigated: Cavities where the longest rods fit in ($x_C = 8.5D$), cavities for the intermediate ($x_C = 6.5D$) and short rods ($x_C = 4.5D$), and cavities where no rod fits in with its orientation planar to the wall and parallel to the side wall ($x_C = 3.5D$). One can image a cavity pattern as a groove structure with additional cross walls that break the translational invariance of the groove structure in x-direction.

Density distribution functions of the systems with the longest cavities ($x_C = 8.5D$) in the low, intermediate, and high pressure regime are presented in Fig 4.12 (a)-(c). The low pressure results are shown in part (a). The behavior of ρ_3^* (-·-·-) equals that from the planar wall and the groove structure. The maximum of the '|−' constellations is somewhat smaller, however. Larger deviations from the previously studied substrate types are observed for the longer rods. ρ_5^* (—) is reduced significantly in the range $|z - z_0| \leq 2D$ and ρ_7^* (– – –) is decreased to about 10% of the bulk value. The additional restriction of the accessible volume due to the cross walls has its largest impact on longer rods, apparently. The characteristics for $|z - z_0| \geq 4D$ are essentially the same as for the groove structure.

One pronounced and one weak layer of rods parallel to the substrate are observed at intermediate pressure $P^* = 2$ (Fig. 4.12 (b)) inside the cavities. The layers are mainly composed of long rods. There is no indication that short rods are incorporated in the second layer. Instead, they show the peak from '|−' constellations. All in all, the composition inside the cavities in the intermediate pressure regime is quite heterogeneous.

The polydispersity inside the cavities reduces drastically in the high pressure regime as demonstrated in Fig. 4.12 (c). The cavities are essentially filled with long rods arranged in three layers. ρ_5^* is about 15% of ρ_7^* and ρ_3^* is basically zero. One also finds some layering on top of the cavities but with a distinctly larger polydispersity. A first comparison of the planar wall, grooves, and long cavities points out that the best results concerning a length specific aggregation are obtained by the cavities. These properties are illuminated in detail in Section 4.1.4.

Fig. 4.13 depicts density distribution functions for cavities of length $x_C = 6.5D$ and $x_C = 4.5D$ in the high pressure regime. Results for the low pressure are omitted due to their similarity with the low pressure results of long cavities. In the interior of the cavities of intermediate length (Fig. 4.13 (a)),

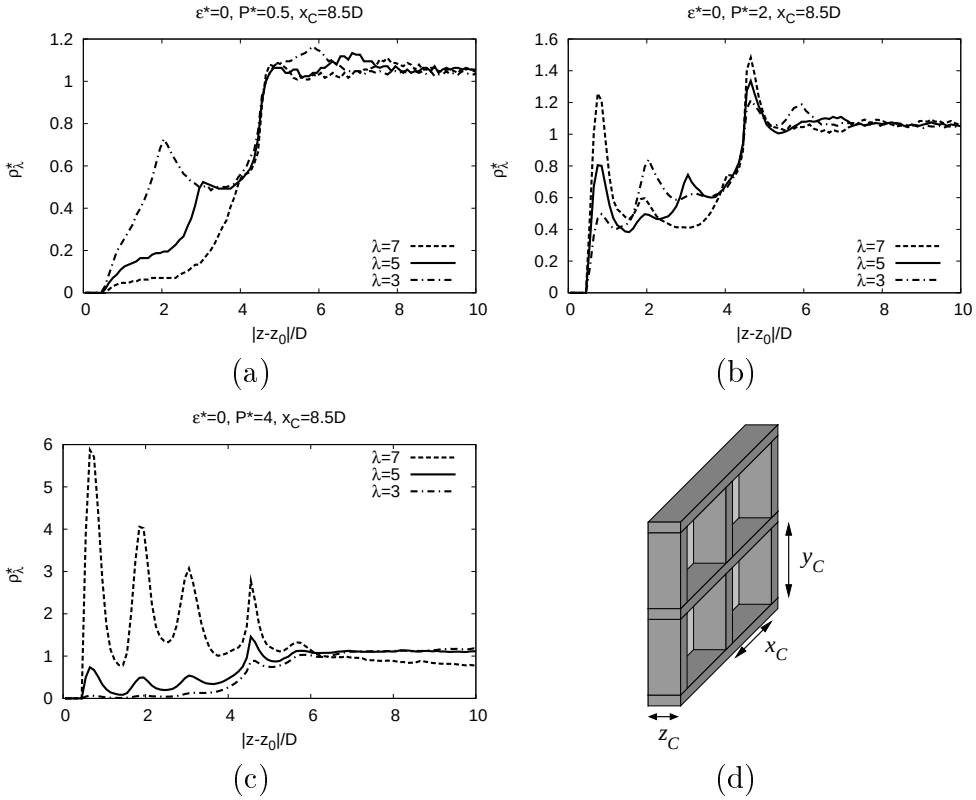

Figure 4.12: Density distribution ρ_λ^* as a function of the distance $|z - z_0|$ to the wall of a tridisperse system of hard rods in contact with a substrate with long cavities of length $x_C = 8.5D$ (a) at low pressure ($P^* = 0.5$), (b) at intermediate pressure ($P^* = 2$), and (c) at high pressure ($P^* = 4$). (d) Illustration of a substrate with rectangular cavities.

three layers are found. The main contribution stems from rods of axis ratio $\lambda = 5$. Short rods are incorporated into the layers to a larger extend as in the case of long cavities. On top of the cavities, one pronounced and one weaker layer are formed, which consist mainly of the longest rods. The peak location at $|z - z_0| \approx 4.7D$ is typical for a layer flat on top of the cavities. The height of the maximum of ρ_7^* at $|z - z_0| \approx 4.7D$ is comparable to the longer cavities (Fig. 4.12 (c)) but the decay of ρ_7^* for $|z - z_0| \geq 6D$ is slower.

Short cavities of length $x_C = 4.5$ influence the structure of the system in a completely different manner as demonstrated in Fig. 4.13 (b). In the range $|z - z_0| \leq 2D$, only ρ_3^* is non zero. ρ_3^* reveals two maxima inside the cavities. The first maximum arises from short rods lying flat on the substrate whereas the second maximum stems from '|−' constellations. Maxima from

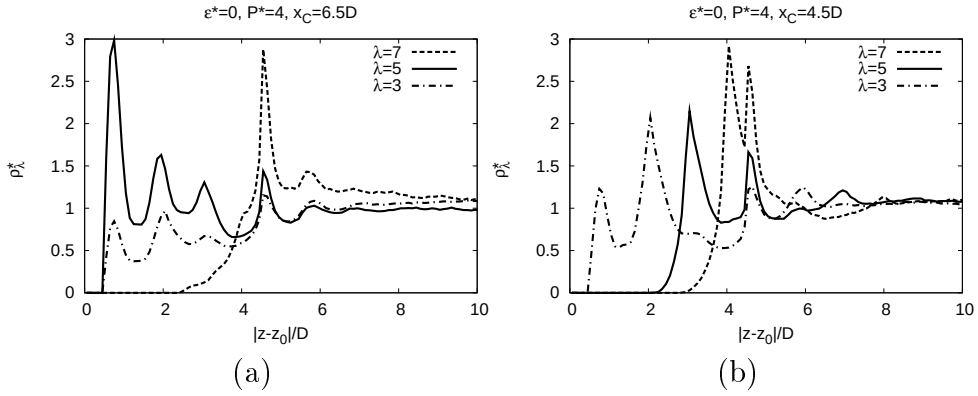

Figure 4.13: Density distribution ρ_λ^* as a function of the distance $|z - z_0|$ to the wall for hard rod systems in the high pressure regime in contact with a substrate with cavities of (a) length $x_C = 6.5D$ and (b) length $x_C = 4.5D$.

homeotropically aligned rods are also observed in ρ_5^* at $|z-z_0| = 3D$ and in ρ_7^* at $|z-z_0| = 4D$. Thus, the short cavities are not entirely filled with short rods but longer rods penetrate the cavities with their orientation perpendicular to the substrate plane.

Fig. 4.14 gives an overview of the orientational correlation function g_θ for the previously investigated cavity structures in the high pressure regime. In Fig. 4.14 (a), g_θ is plotted for the cavity structure for the long rods ($x_C = 8.5D$). The behavior is qualitatively very similar to the groove-like structure (Fig. 4.9 (c)) with multiple layers inside the cavities and the decay of the correlations for $|z - z_0| > 6D$. The orientational order of rods perpendicular to the z-axis is significantly smaller inside cavities of intermediate length ($x_C = 6.5D$) as demonstrated in Fig. 4.14 (b). We know already from the density profiles that layer formation in these cavities is less pronounced and long rods are prevented from entering. Short rods (▬·▬·) exhibit orientations in the xy-plane only in the first layer. g_θ increases quickly ending in the maximum arising from '|−' constellations. Two planar layers are observed for intermediate rods (▬). g_θ for long rods (▬ ▬) is zero in the range $0 \leq |z-z_0|/D \lesssim 3.5$ because the density is zero. The maximum is reached at the locations from '|−' constellations and g_θ forms several minima on top of the cavities. Inside the short cavities with $x_C = 4.5D$ (Fig. 4.14 (c)) only short rods close to wall orient perpendicular to the z-axis. Instead of a multilayer formation, pronounced peaks indicate '|−' configurations. Interestingly, short cavities do not induce long range orientational correlations since g_θ vanishes for $|z - z_0| \gtrsim 9D$, already. Even the system with the planar wall (Fig. 4.14

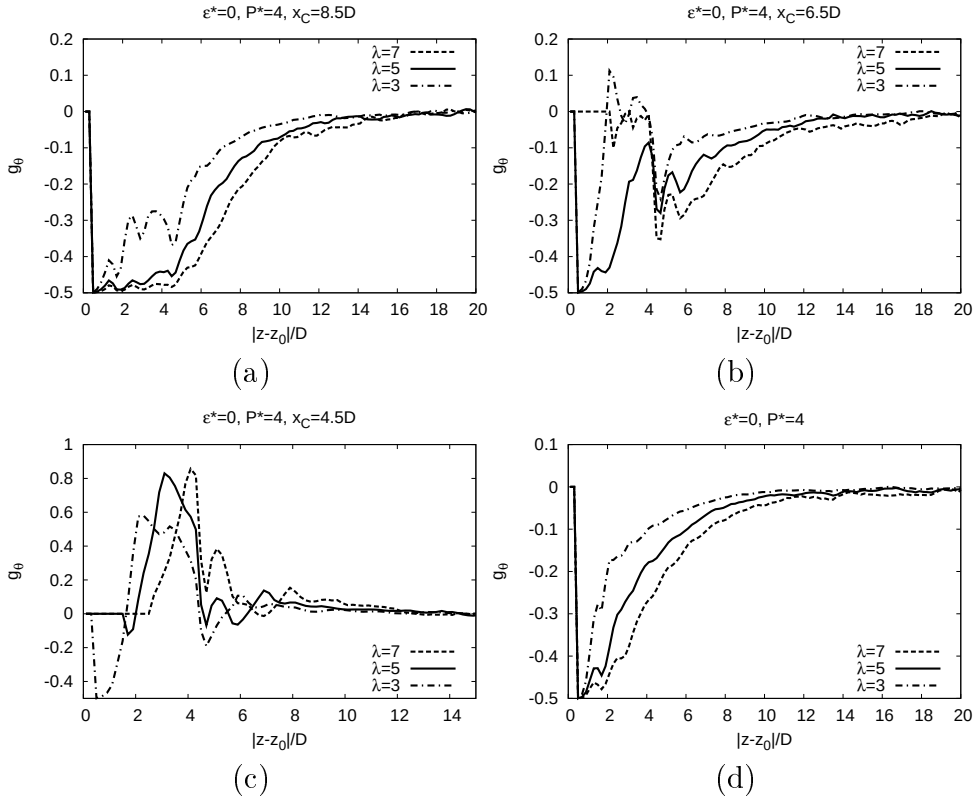

Figure 4.14: Orientational correlation function g_θ as a function of the distance $|z - z_0|$ to the wall at high pressure for (a) long, (b) intermediate, and (c) short cavities. Results for the planar wall are plotted in (d) for comparison.

(d)) is subject to longer ranged correlations.

Snapshots illustrate the described observations. The view in Fig. 4.15 (a)-(d) is along the z-axis and the planar wall is transparent, again. Typical examples of rod configurations in the high pressure regime at $P^* = 4$ are depicted in part (a)-(c). Part (a) shows the case of the longest cavities with length $x_C = 8.5D$ and confirms the high selectivity of the substrate pattern to the long rods. A snapshot for the intermediate cavity length is presented in part (b). We see that most cavities are either filled with rods of intermediate length or with short rods, i. e. a demixing of short and long rods occurs in the individual boxes. This distinction could not be made upon the results for the density distribution function where only averages in the xy-plane are obtained. The same observation holds for the small cavities shown in part (c): One cavity is either filled by short or homeotropically aligned longer rods. Part (d) depicts a system with intermediate cavities at a higher pressure

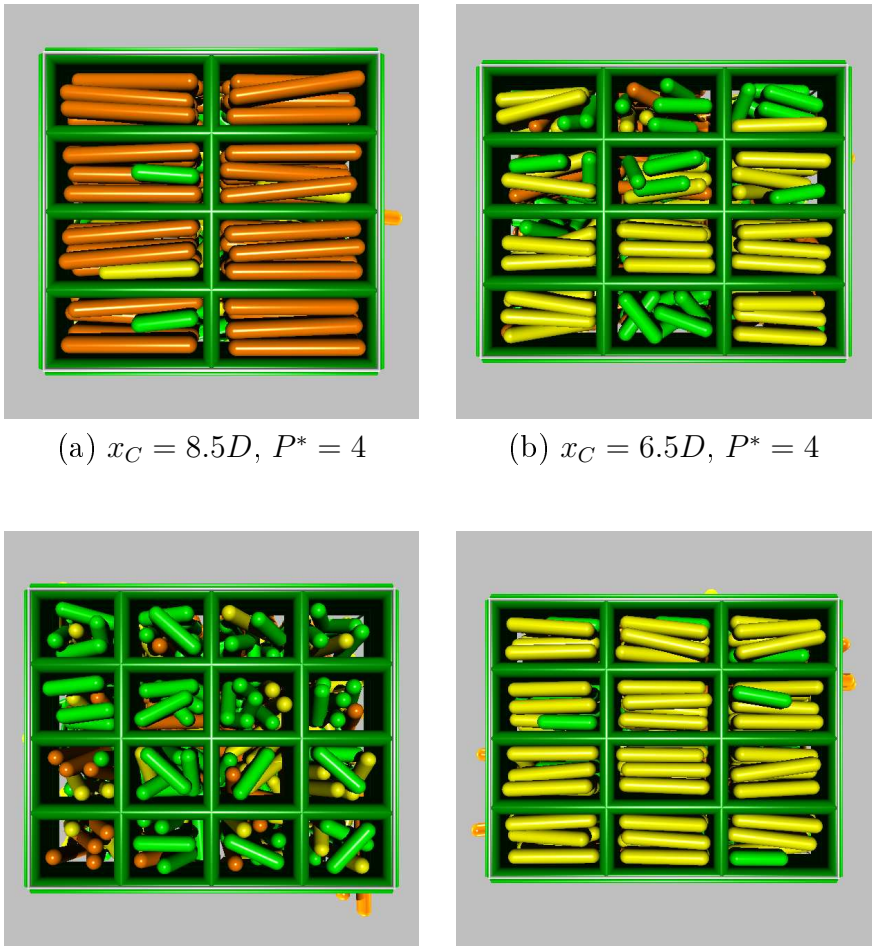

(a) $x_C = 8.5D$, $P^* = 4$ (b) $x_C = 6.5D$, $P^* = 4$

(c) $x_C = 4.5D$, $P^* = 4$ (d) $x_C = 6.5D$, $P^* = 5$

Figure 4.15: (a)-(c) Snapshots of tridisperse hard rod systems in the high pressure regime ($P^* = 4$) with cavities of different length x_C. (d) Cavities of intermediate length ($x_C = 6.5D$) at $P^* = 5$.

$P^* = 5$. All cavities are essentially filled with rods of intermediate length offering a better selectivity to $\lambda = 5$ rods than at the pressure $P^* = 4$.

The smallest cavities investigated have a length $x_C = 3.5D$. Thus, not even the short rods are able to align parallel to the x-axis inside the cavities. Density distribution functions at pressures $P^* = 0.5$ and $P^* = 2$ are presented in Fig. 4.16. At low pressure (Fig. 4.16 (a)), only short rods feature a peak from '|−' configurations inside the cavities. The densities of the longer rods do not adopt a maximal value at the respective locations but exhibit at small plateau. At $P^* = 2$ (Fig. 4.16 (b)), all three rod components possess

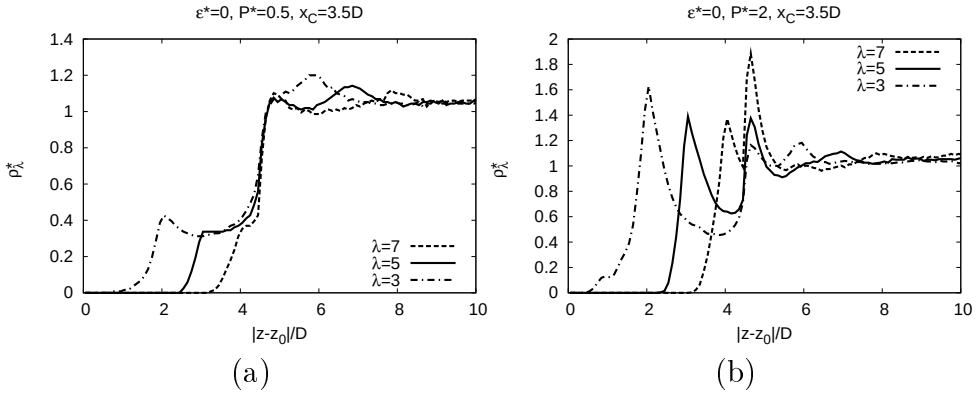

Figure 4.16: Density distribution ρ^*_λ as a function of the distance $|z - z_0|$ to the wall of the tridisperse hard rod suspension in contact with a substrate with very small cavities of length $x_C = 3.5D$ (a) at $P^* = 0.5$ and (b) at $P^* = 2$.

distinct peaks from '|−' configurations. The height of the maxima decreases with increasing rod length and on top of the cavity pattern a layer has formed again at $|z - z_0| \approx 4.7D$. Note that the orientations of the rods on top of the cavities are perpendicular to those inside the cavities. Fig. 4.17 contains the results for the higher pressures. Part (a) corresponds to $P^* = 4$, which is in qualitative agreement with the density profiles at $P^* = 2$ with the heights of all maxima increased. The heights of the peaks of the '|−' constellations,

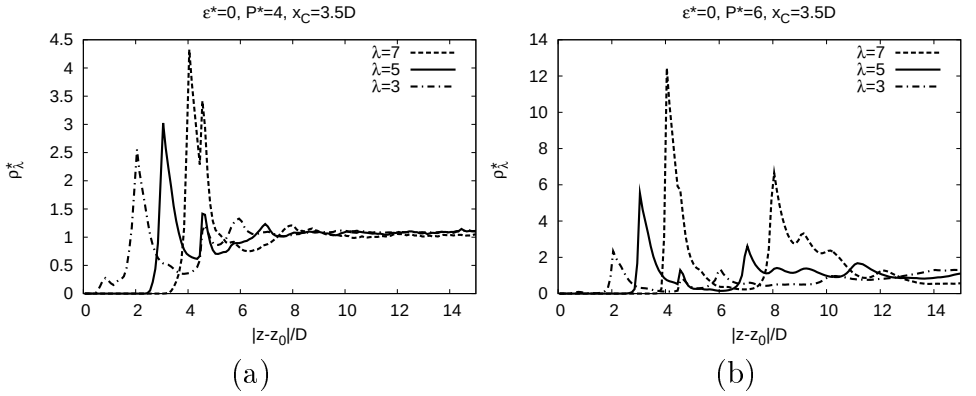

Figure 4.17: Density distribution ρ^*_λ as a function of the distance $|z - z_0|$ to the wall for a tridisperse hard rod system in front of very small cavities ($x_C = 3.5D$) at higher pressures (a) $P^* = 4$ and (b) $P^* = 6$.

however, have a reversed order, i. e. the height increases with the rod length.

The small peak in ρ_3^* at $|z - z_0| \approx 0.7D$ stems from short rods diagonally in the cavities. The density profile undergoes a significant change at $P^* = 6$ as demonstrated in Fig. 4.17 (b). In the region $7 \leq |z - z_0|/D \leq 12$, multiple maxima are observed of predominantely long and intermediate rod lengths. Apparently, a second layer of rods perpendicular to the substrate is created. ρ_7^* exhibits three maxima in that range. The peak at $|z - z_0| = 8D$ can be attributed to long rods oriented along the z-axis on top of the cavities or on top of $\lambda = 3$ rods inside the cavities. The peak at $|z - z_0| \approx 9D$ is related to long rods on top of the layer at $|z - z_0| \approx 4.7D$ and the peak at $|z - z_0| \approx 10D$ arises from a stacking on top of $\lambda = 5$ rods. The explanation for ρ_5^* is straightforward. The modulations of ρ_3^* are much smaller. We point out that the density of short rods reduces significantly in the high density range of long rods.

The homeotropic alignment of the system is analyzed in more detail in terms of g_θ in Fig. 4.18. At $P^* = 4$, homeotropic alignment is basically

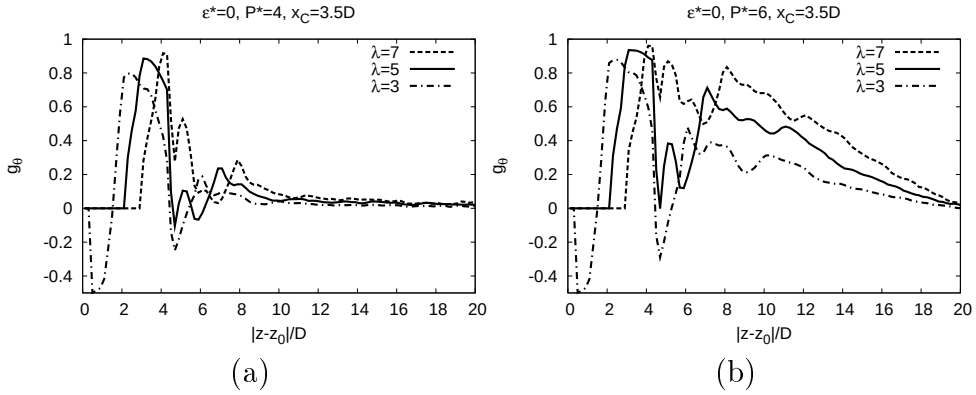

Figure 4.18: Orientational correlation function g_θ as a function of the distance $|z - z_0|$ to the wall of a system of hard rods in contact with a substrate with cavities of length $x_C = 3.5D$ (a) at $P^* = 4$ and (b) at $P^* = 6$.

restricted to the interior of the cavities for all rod lengths as shown in Fig. 4.18 (a). Only two minima with $g_\theta < 0$ appear, one exclusively from short rods inside the cavities and one from mainly short rods on top on the cavities. At $P^* = 6$ (Fig. 4.18 (b)), the rods are aligned more strongly along the z-axis, especially in the region above the cavities ($|z - z_0| > 4D$). The formation of a second homeotropic layer, as mentioned in the discussion of the density profile, is verified by g_θ.

In Fig. 4.19, simulation snapshots of systems at $P^* = 4$ and $P^* = 6$ are depicted. Fig. 4.19 (a) and (b) provide views along the z-axis. Part (a)

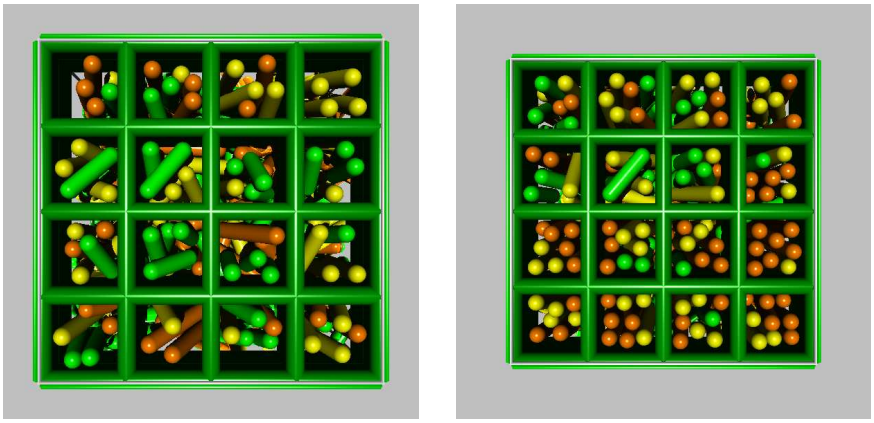

(a) $x_C = 3.5D$, $P^* = 4$ (b) $x_C = 3.5D$, $P^* = 6$

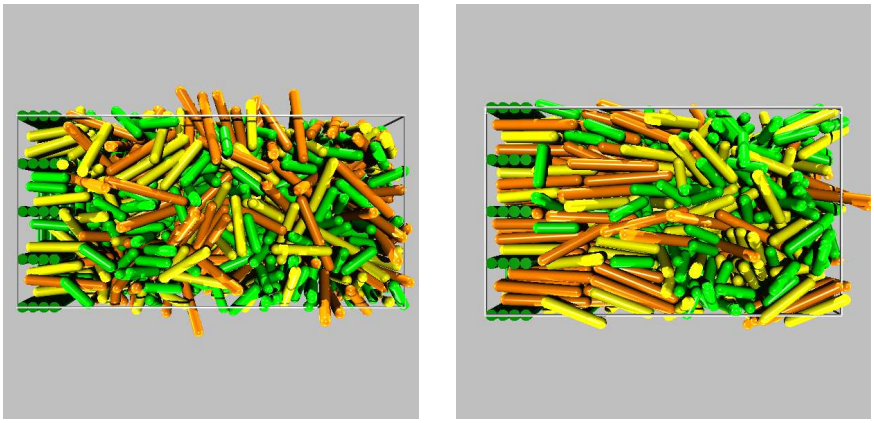

(c) $x_C = 3.5D$, $P^* = 4$ (d) $x_C = 3.5D$, $P^* = 6$

Figure 4.19: The tridisperse hard rod suspension in contact with a substrate with cavities of length $x_C = 3.5D$. Views along the z-axis of systems are provided in (a) at $P^* = 4$ and (b) at $P^* = 6$. Sideviews of the simulation boxes are shown in (c) at $P^* = 4$ and in (b) at $P^* = 6$. The first cavity walls parallel to the view plane are not drawn in order to enable a look inside the cavities.

depicts the situation at $P^* = 4$. The cavities are rather loosely filled and one also can distinguish between cavities with homeotropically aligned rods and cavities with isotropic short rods. The filling of the cavities is strongly enhanced at $P^* = 6$ as shown in part (b). Most cavities are densely packed with long and intermediate rods. Side views of the simulation boxes are provided in Fig. 4.19 (c) and (d). The homeotropic alignment at $P^* = 4$ is merely restricted to the interior of the cavities. At $P^* = 6$, a nematic region

of predominantely long rods has built in the left half of the simulation box whereas short rods accumulate in an isotropic phase in the right half. Thus, the substrate pattern is responsible for a spatial separation of lengths in the system, which is not observed for the corresponding bulk system.

The thermodynamic stability of the phase separated tridisperse system at $P^* = 6$ can not be fully answered in the considered NPT ensemble. The finite size of the system and the particle conservation may result in a metastable configuration. Nevertheless, metastable states play an important role in the early formation process of macroscopic structures. Slow particle transport can be a limiting factor in macroscopic systems. Thus, long-living metastable states can be observed [22]. We stress, that the limitations mentioned here are only directed towards systems at $P^* \gg 4$. Systems with $P^* \leq 4$ do not show any indications of phase separation.

4.1.4 Length specific aggregation

The investigations so far illuminated the spatial structure induced by various kinds of substrate patterns. Now we turn towards the question how the different substrate types modify the local mixing ratio and how the structures can be used to select specific rod types. The goal is to figure out suitable substrate patterns, which enable a precise control of the length distribution in a predefined region. The spatially resolved mole fraction x_λ as introduced in Section 2.5.4 provides a comprehensive overview of the efficiency of a substrate pattern to modify the ratio of the components. Results in the low pressure regime are presented in Fig. 4.20. The mole fraction of the short rods (▬·▬·) is increased close to the substrate in all plots but Fig. 4.20 (c), which shows data for the small grooves of width $y_C = 1.5D$. In latter case, approximately equal amounts of rod components are present. x_3 is particularly large in the cavity patterns (Fig. 4.20 (d)-(f)). One has to keep in mind, however, that a large local mole fraction does not imply a large local density. Especially inside the grooves and cavities the density of short rods is smaller than in the bulk.

Fig. 4.21 summarizes the mole fractions in the high pressure regime. The mole fractions of the system with the planar wall are plotted in Fig. 4.21 (a). x_7 (▬▬) is about 0.65 for rods in direct wall contact ($|z - z_0| = 0.5D$) and decays rapidly to a local minimum at $|z - z_0| \approx 1.3D$ where x_3 adopts a local maximum. The horizontal lines in the plot correspond to the bulk mixing ratio $0.47 : 0.304 : 0.226$. x_3 is slightly above the respective line for $|z - z_0| \geq 4D$ because of the displacement close to wall and the conservation of particles. x_7 is lowered compared to the bulk value for analogous reasons. The mole fraction of intermediate rods (▬) remains basically unchanged

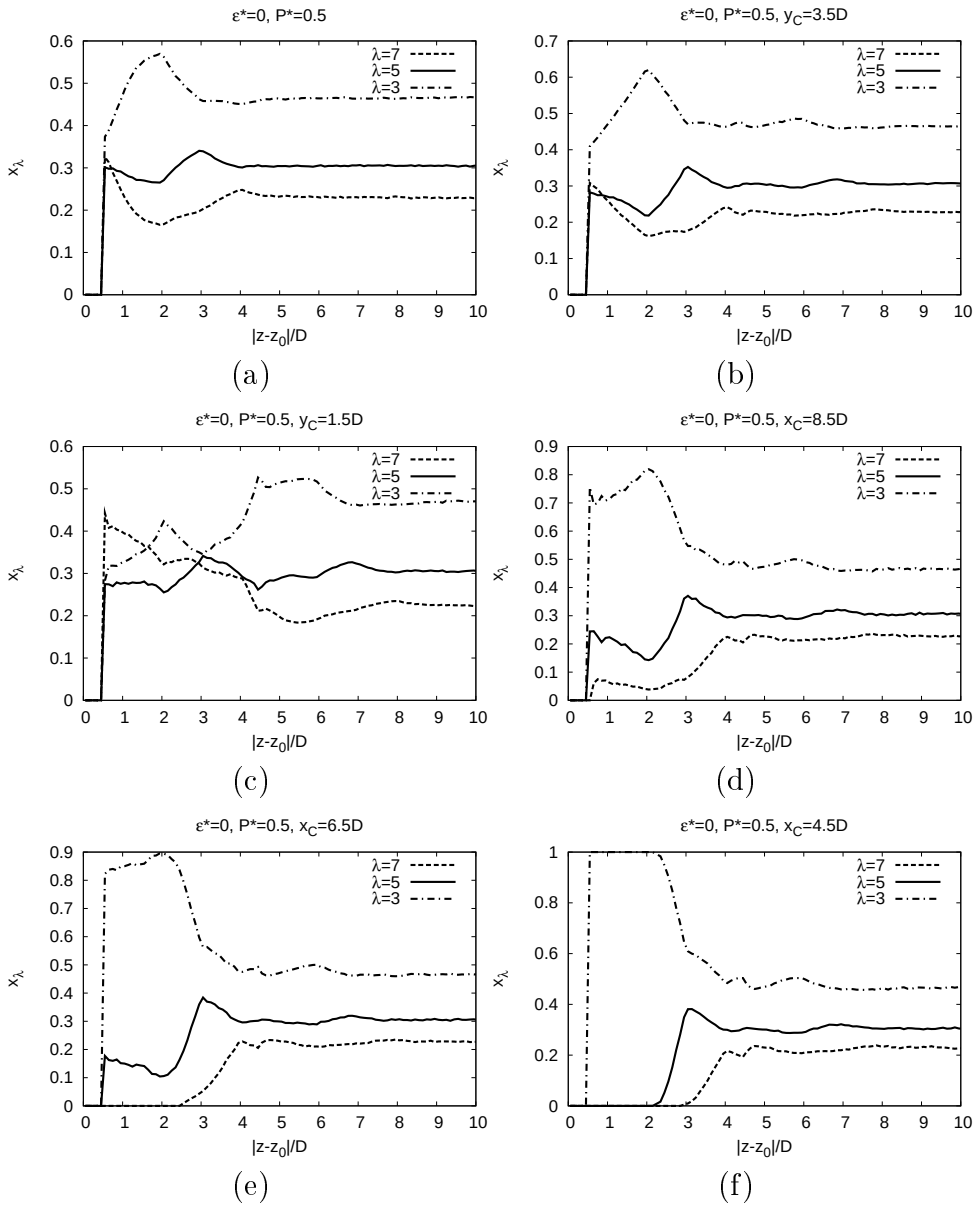

Figure 4.20: Spatially resolved mole fraction x_λ as a function of the distance $|z - z_0|$ to the wall for different substrate patterns in the low pressure regime. (a) Planar wall, (b) grooves of width $y_C = 3.5D$, (c) grooves of width $y_C = 1.5D$, (d) cavities of length $x_C = 8.5D$, (e) cavities of length $x_C = 6.5D$, and (f) cavities of length $x_C = 4.5D$.

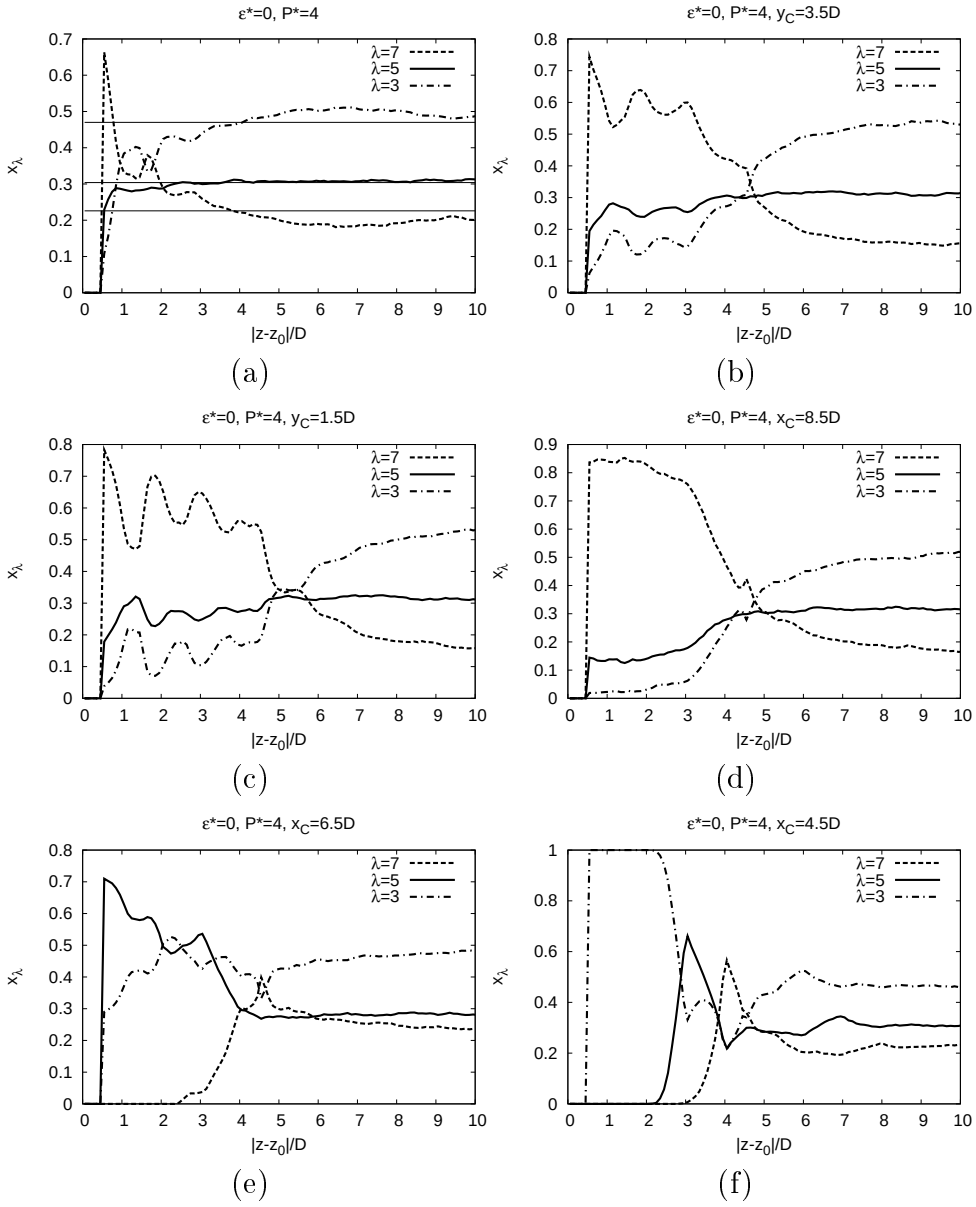

Figure 4.21: Spatially resolved mole fraction x_λ as a function of the distance $|z - z_0|$ to the wall in the high pressure regime ($P^* = 4$) of various substrate patterns. (a) Planar wall, (b) grooves of width $y_C = 3.5D$, (c) grooves of width $y_C = 1.5D$, (d) cavities of length $x_C = 8.5D$, (e) cavities of length $x_C = 6.5D$, and (f) cavities of length $x_C = 4.5D$.

and deviates only slightly from its bulk value inside the grooves as demonstrated in Fig. 4.21 (b) and (c). The grooves are capable to prolong the differentiation of long and short rods to $0 \leq |z - z_0|/D \leq 4$. Narrow grooves (Fig. 4.21 (c)) appear to be more effective than broad grooves (Fig. 4.21 (b)) in this sense. The longest cavities ($x_C = 8.5D$) provide the best selection of long rods as shown in Fig. 4.21 (d). More than 80% of the rods in the range $|z - z_0| \leq 3D$ have axis ratio 7 and short rods are mainly absent. The cavities also reduce x_5 distinctly, which is not observed for the planar and the corrugated wall. The composition inside the cavities is thus highly monodisperse. Cavities of intermediate length increase the mole fraction of intermediate rods (Fig. 4.21 (e)), especially around $|z - z_0| = 0$. In the range $2 \leq |z - z_0|/D \leq 4$, short and intermediate rods contribute about the equal amount. On the first view, short cavities (Fig. 4.21 (f)) seem to generate a purely monodisperse suspension of short rods in the range $z \leq 2D$. But short cavities are filled with homeotropically aligned intermediate and long rods to a large extent so that the volume inside the cavities is mainly used by longer rods. Note that the spatially resolved mole fraction as well as the density distribution function are defined in terms of the center of mass of the rods. The significancies from the '|−' configurations of $\lambda = 5$ and $\lambda = 7$ rods appear also in x_5 and x_7.

In summary, we find that in regions close to the substrate the mixing ratio changes. Structured substrates amplify this effect and expand the respective region. Cavities for the longest rods generate a highly monodisperse region of long rods and also the amount of intermediate rods can be enriched inside appropriate cavities. This effect improves at higher pressure as demonstrated in Fig. 4.22. Part (b) shows the mole fraction of a system with cavities of intermediate length at $P^* = 5$. For comparison the data at $P^* = 4$ is plotted in part (a), again. The cavities discriminate very sensitively between short and intermediate rods while the latter contribute about 80% to the composition in the range $|z - z_0| \leq 3D$.

4.1.5 Shallow cavities

From a technical point of view, cavities with a lower depth z_C might be fabricated more easily. In this section, cavities of depth $z_C = 1D$ are discussed, briefly. The low pressure regime is skipped since no important changes take place compared to the low pressure regime of a planar wall. The density distribution functions in the high pressure regime are plotted in Fig. 4.23. The profile of long cavities (Fig. 4.23 (a)) is qualitatively similar to the planar wall (Fig. 4.2 (b)) but the density of intermediate and short rods is strongly reduced inside the cavities. The ratio of ρ_5^* to ρ_7^* at the first maximum is

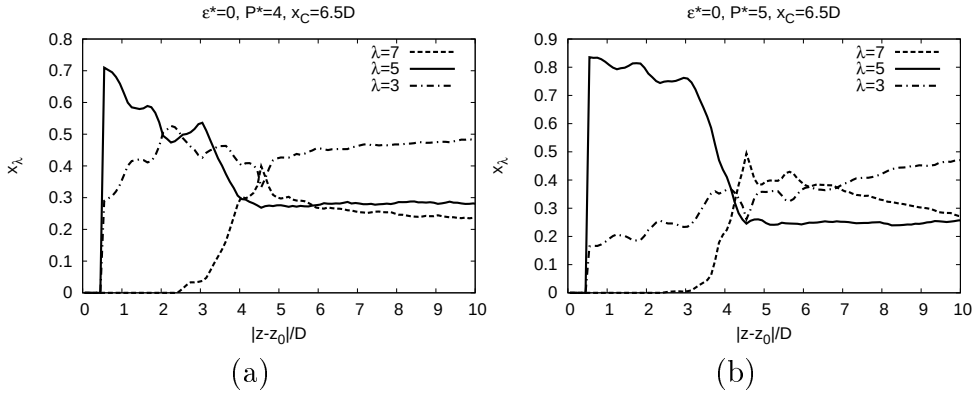

Figure 4.22: Spatially resolved mole fraction x_λ as a function of the distance $|z - z_0|$ to the wall of a tridisperse hard rod system in contact with cavities of intermediate length $x_C = 6.5D$ at the pressure (a) $P^* = 4$ and (b) $P^* = 5$. The fractionation is significantly more enhanced at $P^* = 5$.

about 30% for the planar wall and 18% for the shallow cavities. The best ratio, however, is obtained by the cavities of depth $z_C = 4D$ and amounts to 12%.

The result for the intermediate cavity length is presented in Fig. 4.23 (b). The curve for long rods (▬▬) is shifted to the right by roughly one rod diameter. Thus, the region $0.5 \leq |z - z_0|/D \leq 1.5$ is exclusively filled by short and intermediate rods with the latter contributing about 70% to the density.

In the case of short cavities (Fig. 4.23 (c)), the curves for long (▬▬) and intermediate rods (▬) are shifted rightwards. The density of short rods (▬·▬·) inside the cavities is larger than for cavities of length $x_C = 8.5D$ and length $x_C = 6.5D$ but does not exceed the bulk value noticeable.

All in all, shallow and deep cavities show similar properties. The cavities are preferentially filled with the longest rod component, which can be placed inside the cavities with the orientation of the rods parallel to the wall. The possibility to generate predefined regions in the system where demixing takes place is still given but to a reduced extend.

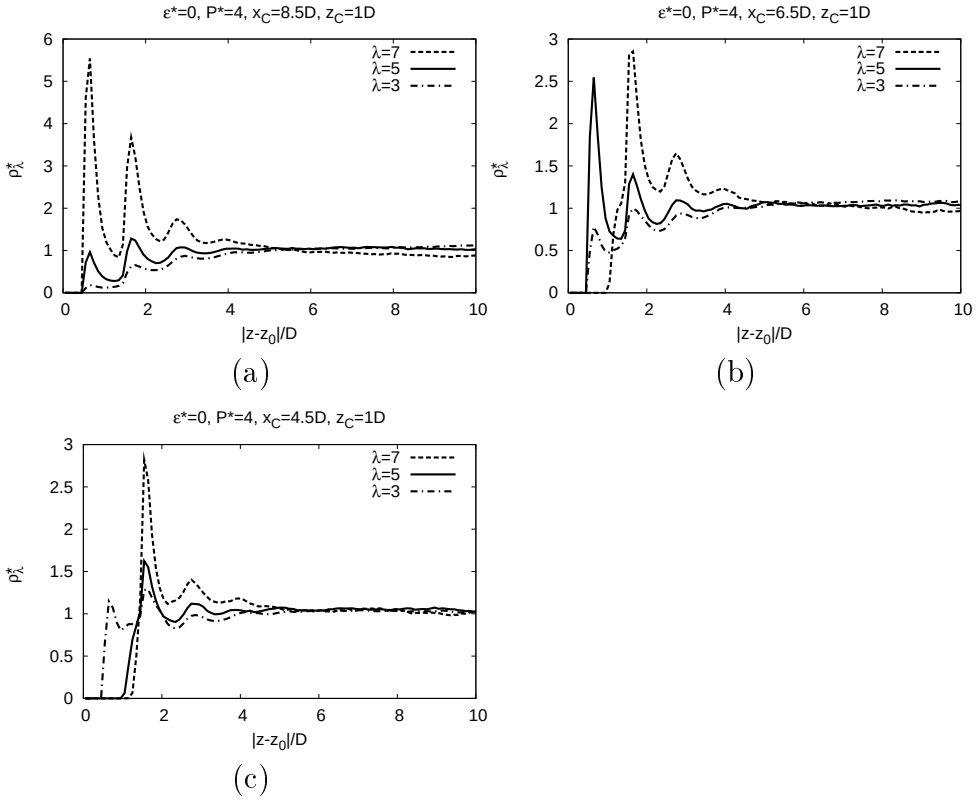

Figure 4.23: Density distribution ρ^*_λ as a function of the distance $|z - z_0|$ to the wall of systems with shallow cavities with depth $z_C = 1D$ in the high pressure region (a) for long, (b) for intermediate, and (c) for short cavities.

4.1.6 Attractive rods on hard substrates

The majority of the studies in the previous sections utilized the hard rod model ($\epsilon^* = 0$). Only few results for attractive rods ($\epsilon^* = 0.5$) at lower pressures were discussed in Section 4.1.1, in which minor differences compared to hard rod systems were observed. Appropriately designed substrate patterns bear most effects on the structure of the fluid at high pressures, particularly concerning length specific aggregation as demonstrated in Section 4.1.4. In this sense, structured substrates are much less effective in systems of attractive rods since pronounced fractionation takes place already in the bulk.

Some qualitative properties of attractive rod systems above the bulk ordering transition are explained on the basis of snapshots presented in Fig. 4.24. The pressure is $P^* = 3.5$ for all pictures. Fig. 4.24 (a) depicts the system in contact with a planar wall. The system has separated into

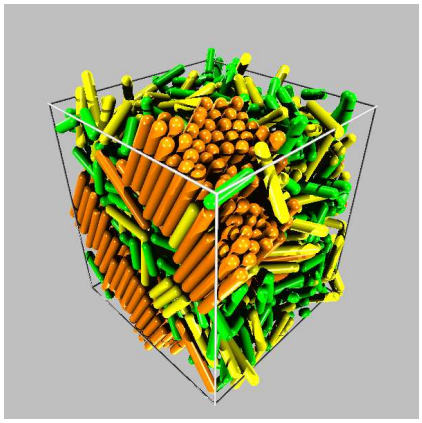

(a) $\epsilon^* = 0.5$, $P^* = 3.5$, planar wall

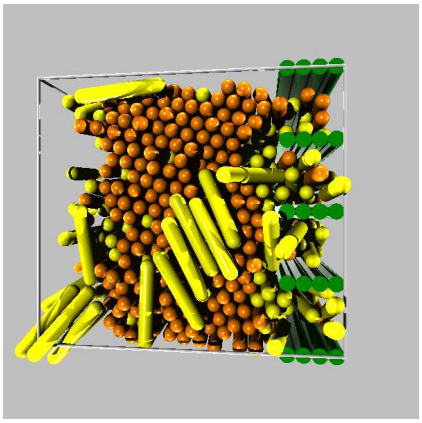

(b) $\epsilon^* = 0.5$, $P^* = 3.5$, $y_C = 3.5D$

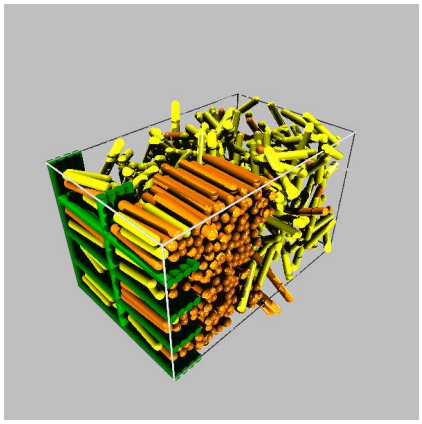

(c) $\epsilon^* = 0.5$, $P^* = 3.5$, $x_C = 8.5D$

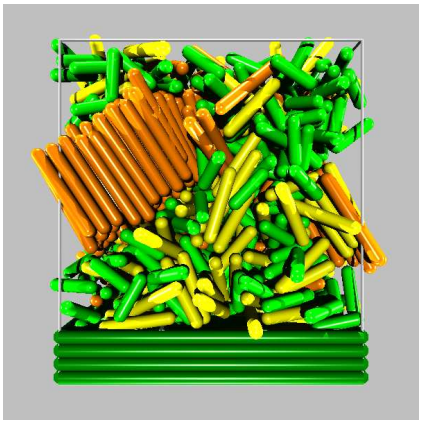

(d) $\epsilon^* = 0.5$, $P^* = 3.5$, $x_C = 6.5D$

Figure 4.24: Snapshots of systems of attractive rods in contact with various substrate types at pressure $P^* = 3.5$. (a) Planar wall, (b) grooves of width $y_C = 3.5D$, (c) cavities of length $x_C = 8.5D$, and (d) cavities length $x_C = 6.5D$. In (a)-(c) the hexatic cluster adheres at the substrate but not in (d).

a highly ordered monolayer of long and an isotropic fluid of shorter rods[3]. The cluster adheres at the substrate. The two visible domains of long rods are connected via the periodic boundaries. A system with grooves of width $y_C = 3.5D$ is shown in Fig. 4.24 (b) whereas short rods are not drawn in the snapshot. The cluster adheres at the substrate and the orientation of the

[3]The same separation is also observed in bulk systems.

rods in the cluster coincide with direction of the grooves. A system with a cavity pattern for the longest rods is presented in Fig. 4.24 (c). Short rods are omitted. The cluster orients along the grooves and adheres at the substrate, again. One must note, however, that most long rods are incorporated into the cluster and are therfore depleted from half of the cavities. Fig. 4.24 (d) illustrates a system with cavities of intermediate length. The cluster is surrounded completely by the isotropic fluid of shorter rods and does not adhere at the substrate. These examples the shown to demonstrate the influence of adjacent substrates on attractive rods. Further studies are needed to clarify the effects in detail.

4.2 Polydisperse suspension

This section is dedicated to study the structure of a polydisperse suspension in contact with the three substrate types, i. e. the planar wall, the grooves, and the rectangular cavities. The length distribution is the same as in Fig. 3.15 on page 53. The structure induced by the different substrate patterns was investigated in detail in the previous section for the tridisperse suspension. This section focuses on a representative selection of results for polydisperse rod systems, which are compared to the tridisperse analogs.

4.2.1 Planar substrate

Fig. 4.25 shows the density distribution functions of a hard rod system in contact with a planar wall. For the sake of clarity and to gain better statistics, cumulative distribution functions (Section 2.5.3) are presented where the two longest components ($\lambda \in \{7, 8\}$), the two intermediate ($\lambda \in \{4, 5\}$), and the two shortest components ($\lambda \in \{1, 2\}$) are subsumed. The agreement of the low and high pressure results with the tridisperse mixture (Fig. 4.2) is remarkable. At $P^* = 0.5$, maxima from '|−' configurations appear in every curve and a layer flat on the wall occurs only for the longest rods as demonstrated in Fig. 4.25 (a). The maxima from '|−' constellations are broader, however, since in each case the density profiles of two rod lengths are merged. At $P^* = 4$ (Fig. 4.25 (b)), layer formation mainly from the long rods (▬ ▬ ▬) is visible. Intermediate rods (▬) are incorporated in the layers distinctly less. Especially short rods (▬·▬·) are hardly affected by the layer formation.

Hard and attractive rods at $P^* = 2$ are compared in Fig. 4.26. Part (a) depicts the cumulative density distribution function for short and part (b) for long rods. The corresponding curves for hard and attractive rods are

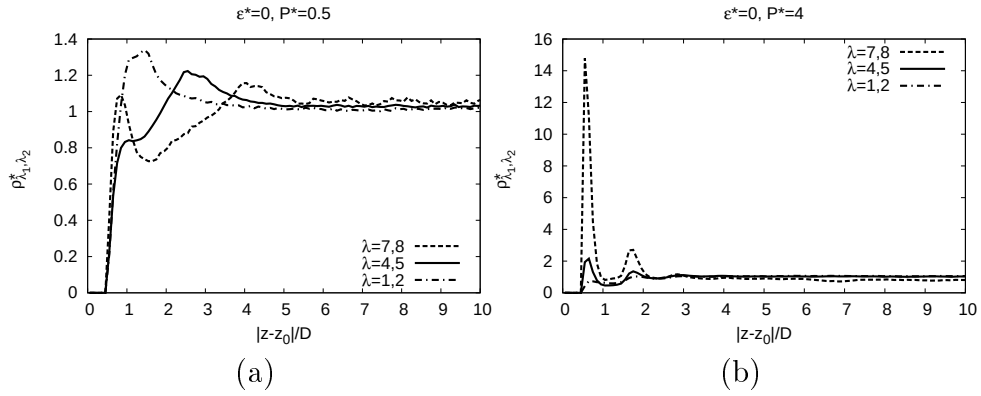

Figure 4.25: Cumulated density distribution $\rho^*_{\lambda_1,\lambda_2}$ as a function of the distance $|z - z_0|$ to the wall of a polydisperse hard rod system in contact with a planar wall. (a) Low pressure results for long (▬ ▬), intermediate (▬), and short rods (▬·▬·). (b) The corresponding high pressure results. The similarities to the tridisperse mixture (Fig. 4.2) are extensive.

basically identical and deviate only slightly at the second maximum in the same way as shown in Fig. 4.5 (c) and (d) for the tridisperse suspension.

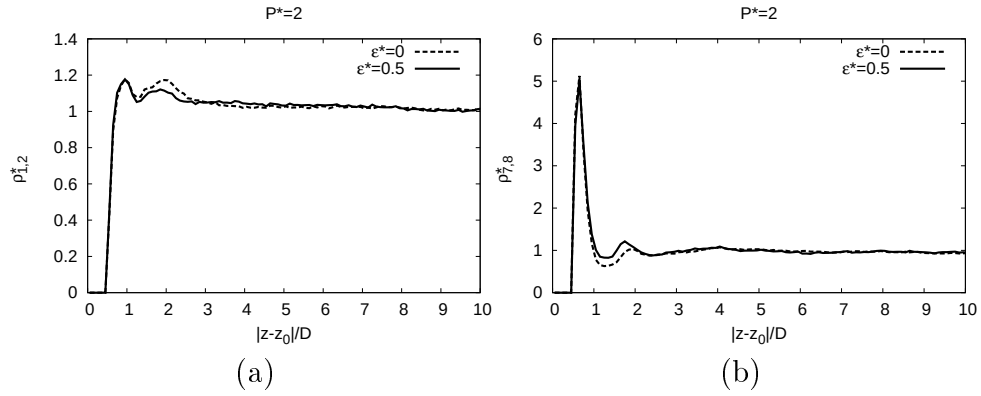

Figure 4.26: Cumulated density distribution $\rho^*_{\lambda_1,\lambda_2}$ as a function of the distance $|z - z_0|$ to the wall for hard (▬ ▬) and attractive rods (▬) in the medium pressure regime ($P^* = 2$) for (a) short ($\lambda \in \{1, 2\}$) and (b) long rods ($\lambda \in \{7, 8\}$).

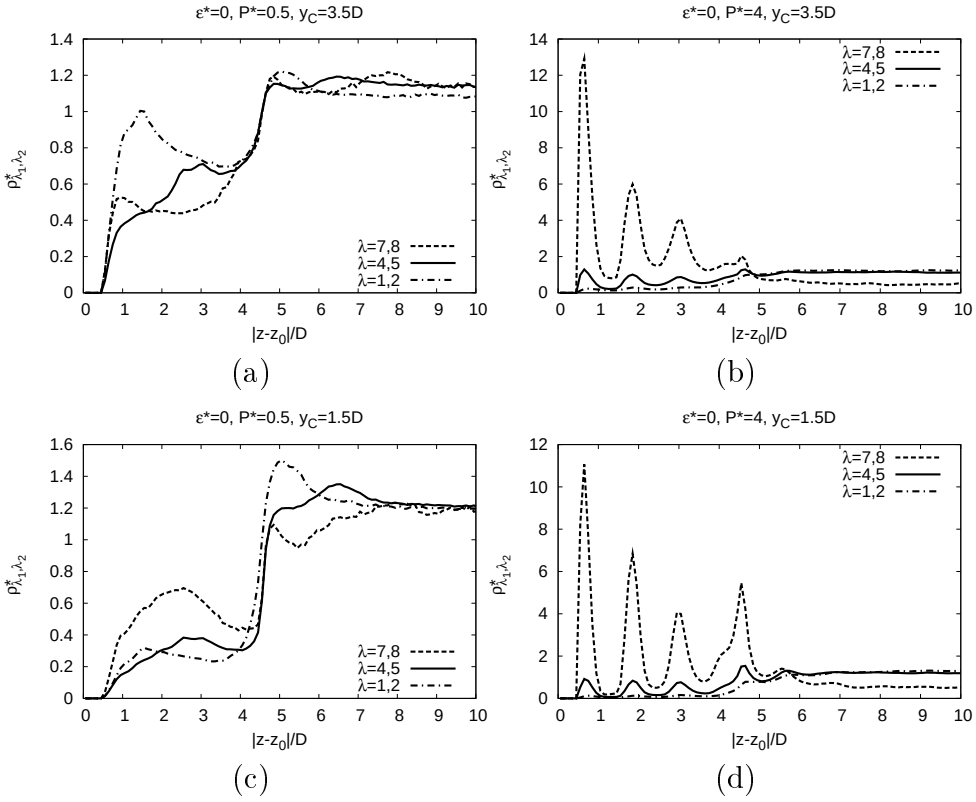

Figure 4.27: Cumulated density distribution $\rho^*_{\lambda_1,\lambda_2}$ as a function of the distance $|z - z_0|$ to the wall of a hard rod system in contact with a corrugated substrate. Broad grooves ($y_C = 3.5D$) at (a) low pressure and (b) high pressure. Narrow grooves ($y_C = 1.5$) at (c) low and (d) high pressure.

4.2.2 Corrugated substrate

Hard rod systems in contact with broad ($y_C = 3.5D$) and narrow grooves ($y_C = 1.5D$) are investigated in Fig. 4.27. The effects observed for the tridisperse mixture (Figs. 4.8 and 4.10) also emerge in the polydisperse mixture, which are:

1. The density of short rods is largest in broad grooves whereas in narrow grooves the long rods dominate in the low pressure regime (Fig. 4.27 (a) and (c)).

2. Rods in the region $|z - z_0| > 4D$ behave similar to those in front of a planar wall at $P^* = 0.5$ (Fig. 4.27 (c)).

3. At high pressure three layers of mainly long rods form inside the grooves

(Fig. 4.27 (b) and (d)).

4. The layer formation on top of the grooves $|z - z_0| \approx 4.7D$ is more pronounced for narrow grooves (Fig. 4.27 (c) and (d)).

Apparently, the tridisperse and the polydisperse mixture show the same effects in the investigated parameter range. The density distribution functions apportioned into long, intermediate, and short rods are comparable in both systems. Thus, the results hold a universal character and qualitatively similar effects are also expected to occur in length-polydisperse suspensions with other length distributions. In the following, systems with cavity patterns are studied where the density profiles of the single components are presented rather than the cumulative density distribution functions.

4.2.3 Cavity pattern

As demonstrated in Section 4.1.4, adequately tailored cavities are capable to induce a highly monodisperse segregation of predefined rod lengths close to the substrate. In the polydisperse suspension, eight rod lengths are present with integer values of the axis ratio allowing for a refined λ-dependent structure analysis. Fig. 4.28 depicts density profiles of hard rod systems in contact with cavities of length $x_C = 8.5D$ (part (a)) and $x_C = 6.5D$ (part (b)) at high pressure. Data is presented for the three longest rod lengths with

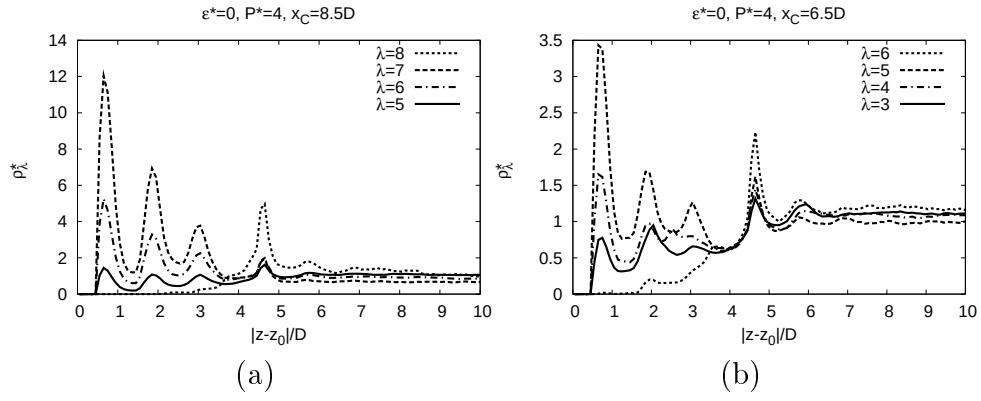

Figure 4.28: Density distribution ρ^*_λ as a function of the distance $|z - z_0|$ to the wall in the high pressure region of a polydisperse hard rod system in contact with cavities (a) of length $x_C = 8.5D$ and (b) of length $x_C = 6.5D$. Shown are curves for the three largest rod lengths that fit into the respective cavities and one for rods, which are longer than x_C.

$(\lambda+1)D < x_C$ and for the shortest rods with $(\lambda+1)D > x_C$. Three layers arise inside the long cavities (Fig. 4.28 (a)). The density of $\lambda = 7$ rods (▬▬) is largest and ρ_6^* (▬·▬·) is somewhat less than 50% of ρ_7^*. It is quite remarkable, to which extend ρ_5^* (▬) is reduced. The density of $\lambda = 5$ rods inside the cavities is about the bulk value whereas the two next longer components exceed their bulk value several times. Rods with $\lambda = 8$ (····) do not fit in layers into the cavities and thus aggregate on top.

The layer formation inside cavities of intermediate length (Fig. 4.28 (b)) is reduced noticeably but the main contributions stem from the two longest rod components, which are able to form layers inside the cavities. In this case, these are $\lambda = 5$ (▬▬) and $\lambda = 4$ rods (▬·▬·). Subsuming the observations, we conclude that cavities of a certain length are highly sensitive to the longest rods, which can form layers inside. In the studied systems, shorter rods, which in principle could enter the cavities, are significantly restrained.

A comprehensive overview of the demixing capabilities of the various substrate types delivers the integrated mole fraction x_λ^{int} as defined in Eq. (2.43). x_λ^{int} is obtained by integrating the mole fraction $x_\lambda(z)$ from $z = -z_0$ to $z = -z_0 + 4D$. Thus, x_λ^{int} is the number of rods with axis ratio λ in the region $z_{\min} \le z \le z_{\max}$ divided by the overall number of rods in that region. Fig. 4.29 contains the corresponding results. The symbols are measurements and the lines are a guide to the eye. Fig. 4.29 (a) depicts the data for the polydisperse suspension at $P^* = 4$. In the system with the planar wall (○), x_λ^{int} is about 10% for axis ratios smaller than 5 and increases monotonically for longer rods. Each component of the short rods ($\lambda \le 4$) reduces to less than 5% in the system with the broad grooves (▲) whereas the number of longer rods ($\lambda \ge 6$) increases distinctly. The number of $\lambda = 7$ rods increases even further in the system with the long cavities (□). About 50% of all rods have axis ratio $\lambda = 7$ and together with $\lambda = 6$ rods they contribute to about 80%. In the system with the intermediate cavities (●), rods with $\lambda \ge 6$ are very effectively suppressed. x_4^{int} and x_5^{int} add up to approximately 50%. At $P^* = 5$ (Fig. 4.29 (b)), the contribution of shorter rods ($\lambda \le 3$) reduces significantly for intermediate cavities (●). Less than 10% of the rods stem from each component with $\lambda \le 3$ whereas $\lambda = 4$ and $\lambda = 5$ rods constitute circa 70%. The curves for the other substrate types remain basically unchanged at $P^* = 5$.

For completeness, data of x_λ^{int} for the tridisperse mixture at $P^* = 4$ is presented in Fig. 4.29 (c). The correspondence of the tridisperse and the polydisperse mixture can be seen best if latter is classified in terms of short ($1 \le \lambda \le 3$), intermediate ($4 \le \lambda \le 5$), and long rods ($6 \le \lambda \le 8$).

We finish the investigations of the polydisperse mixture with some observations in a system with the shortest cavities of length $x_C = 3.5D$ in

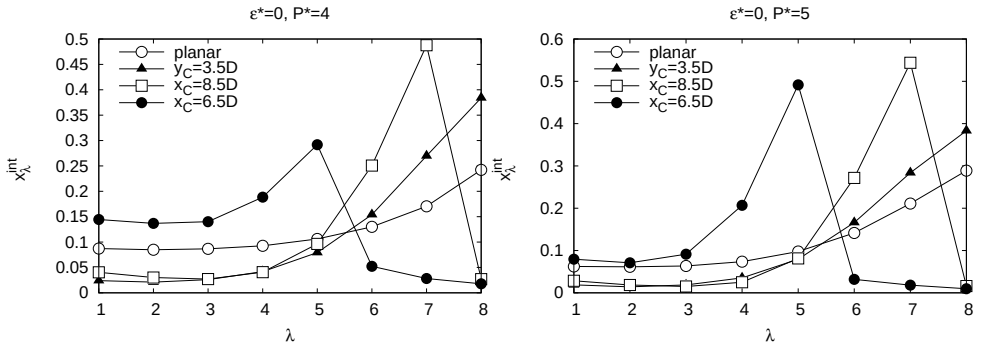

(a) polydisperse mixture, $P^* = 4$ (b) polydisperse mixture, $P^* = 5$

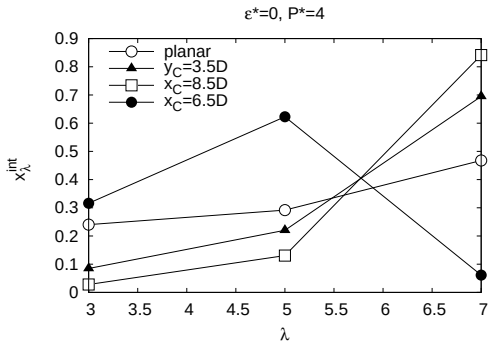

(c) tridisperse mixture, $P^* = 4$

Figure 4.29: The integrated mole fraction x_λ^{int} as a function of the axis ratio λ for the different substrate patterns. The polydisperse hard rod mixture (a) at $P^* = 4$ and (b) at $P^* = 5$. (c) The the tridisperse hard rod system at $P^* = 4$.

Fig. 4.30. In the corresponding system of a tridisperse mixture, homeotropic alignment and phase separation has been observed at pressure $P^* = 6$. Here, one finds similar effects, however, in a reduced manner. Fig. 4.30 (a) depicts the cumulated density profile at $P^* = 6.5$. Long (▬ ▬) and intermediate rod lengths (—) exhibit a pronounced homeotropic alignment in the cavities as revealed by the maxima at $|z - z_0|/D = (\lambda + 1)/2$. The double peaks in each curve are due to the subsumption of two rod lengths. In particular, the longest rods show an increased density in the range $8 \leq |z - z_0|/D \leq 10$, which is caused by a second layer of hometropically oriented rods. The snapshot in Fig. 4.30 (b) illustrates the described observations.

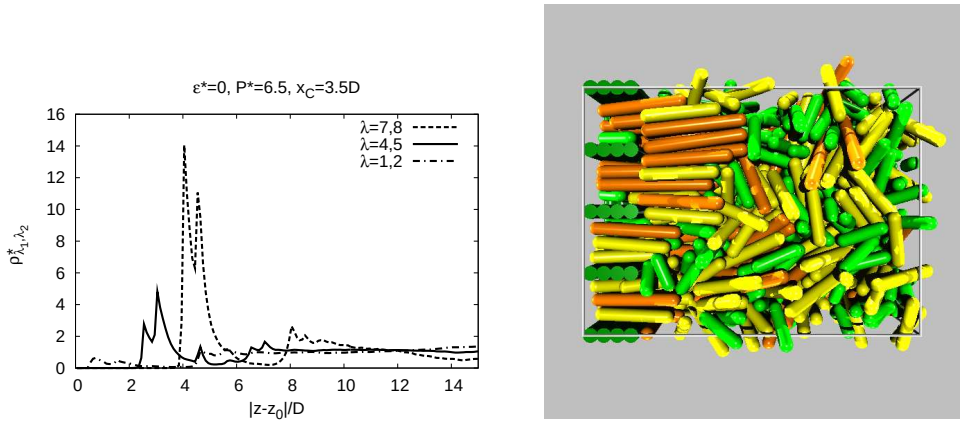

(a) (b)

Figure 4.30: (a) Cumulated density distribution $\rho^*_{\lambda_1,\lambda_2}$ as a function of the distance $|z - z_0|$ to the wall in the polydisperse hard rod system with the smallest cavities ($x_C = 3.5D$) at $P^* = 6.5$. (b) Snapshot of the same system. The longest rods ($6 \leq \lambda \leq 8$) are colored orange, intermediate rods ($4 \leq \lambda \leq 5$) are colored yellow, and the shortest rods ($1 \leq \lambda \leq 3$) are green.

4.3 Alternating cavity pattern

In the final section of this chapter some observations are presented, which arise in systems with alternating cavity patterns. The chosen compositions of the suspensions differ from the tridisperse and polydisperse suspension. The so-called 62 mixture consists of rods with $\lambda = 6$ and $\lambda = 2$. The constituents of the 7531 mixture have axis ratios $\lambda = 7$, $\lambda = 5$, $\lambda = 3$, and $\lambda = 1$. In both mixtures, each component comprises the same volume fraction. The applied pressures are in a range where the corresponding bulk systems start to order.

Firstly, we consider the 62 mixture. Two different setups are investigated. The first one consists of $N = 2000$ rods simulated with the mirroring technique to ensure that the behavior of the substrate at $-z_0$ will not be influenced by the substrate at z_0. The substrate is composed of cavities of alternating length $x_C^{(1)} = 7.25D$ and $x_C^{(2)} = 3.25D$. The width of all cavities is $y_C = 5D$ and the depth is $z_C = 3D$. In the second setup a system with $N = 1000$ particles and two opposing walls each with the same cavity structure is employed. The cavity lengths are $x_C^{(1)} = 7.5D$ and $x_C^{(2)} = 4D$. The system represents a slit pore with structured walls.

Results for the first setup are presented in Fig. 4.31. Part (a) depicts a bottom view of the system. The cavities induce an alternating structure of long and short rods in substrate proximity. The long rods form multiple

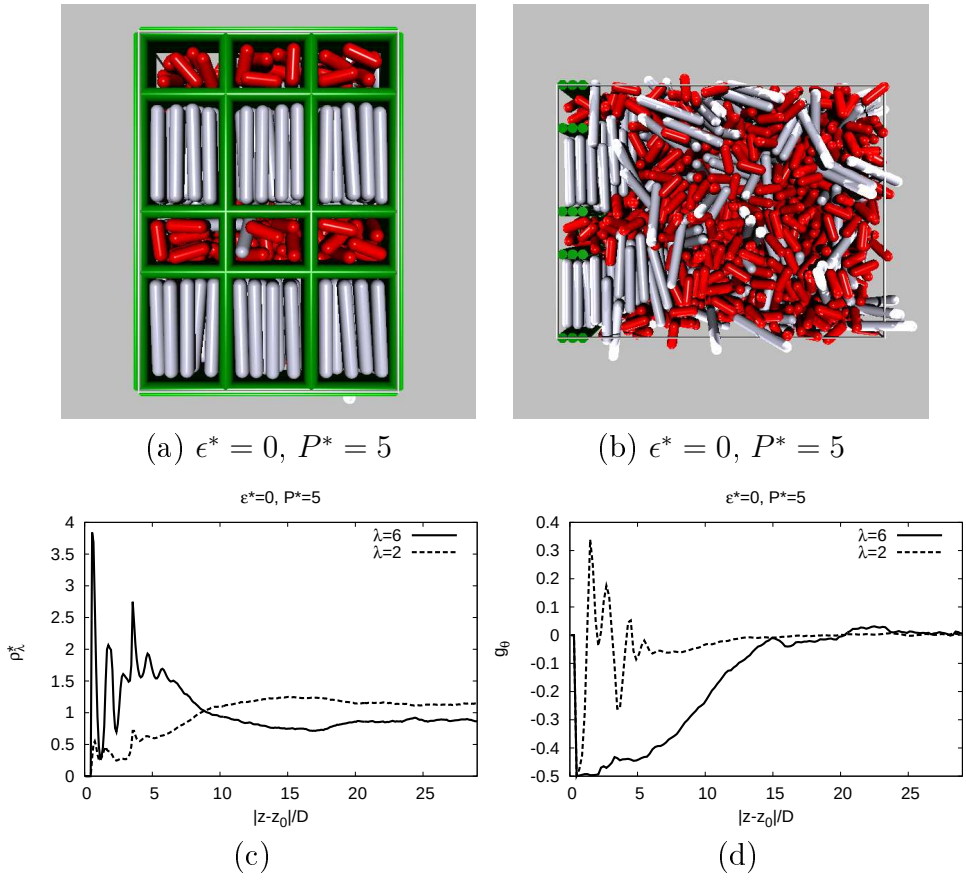

Figure 4.31: Results for the binary 62 mixture at $P^* = 5$ in contact with cavities of alternating length. (a) Bottom view and (b) side view of the simulation box. (c) The density distribution ρ^*_λ and (d) the orientational correlation function g_θ as a function of the distance $|z - z_0|$ to the wall of the same system.

layers inside the cavities as proven by the density profile (Fig. 4.31 (c)) and are strongly aligned as demonstrated by g_θ in Fig. 4.31 (d). The cavities for the long rods are capable to spatially fixate a smectic monolayer[4] of long rods. Fig. 4.31 (b) shows a side view of the simulation box. The interesting point is that the smectic layers exceed the cavity depth by several rod diameters. In the density profile 3-4 peaks are visible for $|z - z_0| \geq 3D$. The alternating cavity length allows short rods to cover regions close to the substrate. Short rods remain basically isotropic even in substrate proximity (Fig. 4.31 (d)).

The results for the second setup are collected in Fig. 4.32. Part (a) and

[4] A smectic monolayer may not be mixed up with a monolayer that covers the substrate.

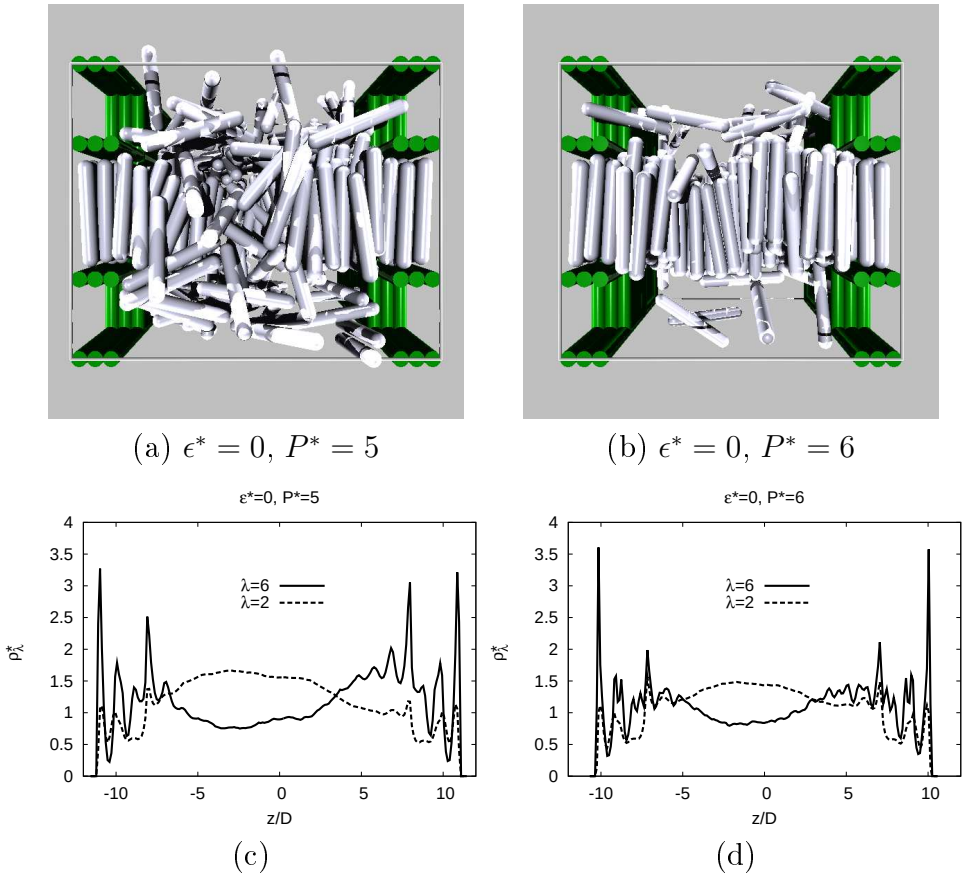

Figure 4.32: Results for the binary 62 mixture in a slit pore with structured walls. Snapshots of the simulation box at pressure (a) $P^* = 5$ and (b) $P^* = 6$. The corresponding density profiles are shown in (c) and (d).

(b) depict snapshots of the system at $P^* = 5$ and $P^* = 6$, respectively. The short rods are omitted for clearness. The cavities, inside which $\lambda = 6$ rods accumulate preferentially, oppose each other. It should therfore be possible to generate a smectic layer, which on the one hand is spatially fixated and on the other hand covers the whole box length. At $P^* = 5$, one smectic layer at each wall has formed. The layers do not penetrate the cavities more than in the case of a single wall (cmp. Fig. 4.32 (c) and Fig. 4.31 (c)). Rods in between both layers are weakly ordered. At the higher pressure $P^* = 6$, both layers join to one smectic layer, which spans the whole simulation box. The density profiles for $P^* = 5$ and $P^* = 6$ are presented in Fig. 4.32 (c) and (d). Long rods (—) exhibit a pronounced peak structure only inside and close to the cavities in both cases. Another interesting point at $P^* = 6$ is

the occurrence of a double peak pattern inside the cavities for $\lambda = 6$, which is characteristic for hexatic ordering and is not observed for $P^* = 5$. In the corresponding bulk system layer formation is also observed at $P^* = 6$ but the order in the transverse direction is clearly not hexatic as demonstrated by $g_\perp^{(6,6)}$ (▬▬) in Fig. 4.33.

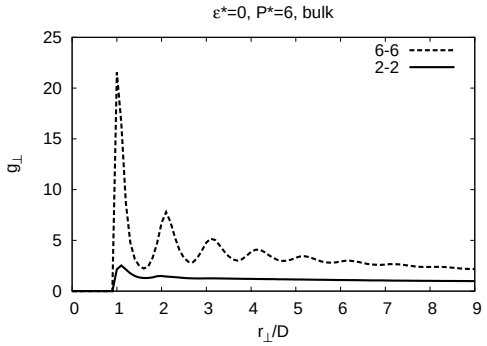

Figure 4.33: Transversal pair correlation function $g_\perp(r_\perp)$ at pressure $P^* = 6$ in a bulk system of the 62 mixture.

The last system studied is the 7531 mixture in contact with cavities of three different lengths $x_C^{(1)} = 8.5D$, $x_C^{(2)} = 6.5D$, and $x_C^{(3)} = 4.5D$. The width is $y_C = 3.5D$ and the depth is $z_C = 4D$. A bottom view of the simulation box at $P^* = 5$ is provided in Fig. 4.34 (a). Long and intermediate cavities are essentially filled by highly ordered rods of axis ratio $\lambda = 7$ and $\lambda = 5$, respectively. Inside the short cavities, isotropic rods with $\lambda = 1$ are mainly found even though the cavities are long enough to allow a layer formation of $\lambda = 3$ rods. The side view of the simulation box (Fig. 4.34 (b)) reveals a growth of a smectic layer of the long rods far into the bulk. From the density profile in Fig. 4.34 (c) we find that ρ_7^* is distinctly above the bulk value in the range $0 \leq |z - z_0|/D \lesssim 12$ and decreases quickly afterwards, i. e. where the smectic layer ends. The peak structure of the smectic layer outside the cavities gets lost but the orientational correlation function g_θ remains close to -0.5 (Fig. 4.34 (d)). The high ordered structure of $\lambda = 5$ rods is restricted to the interior of the cavities.

We summarize that a heterogeneous distribution of cavity lengths induces a heterogeneous distribution of rod lengths in substrate proximity. In addition, smectic layers can exceed the cavity depth significantly. Thus, cavities represent not only a possibility to generate highly monodisperse suspensions but may also serve as an interesting tool to study smectic monolayers in detail.

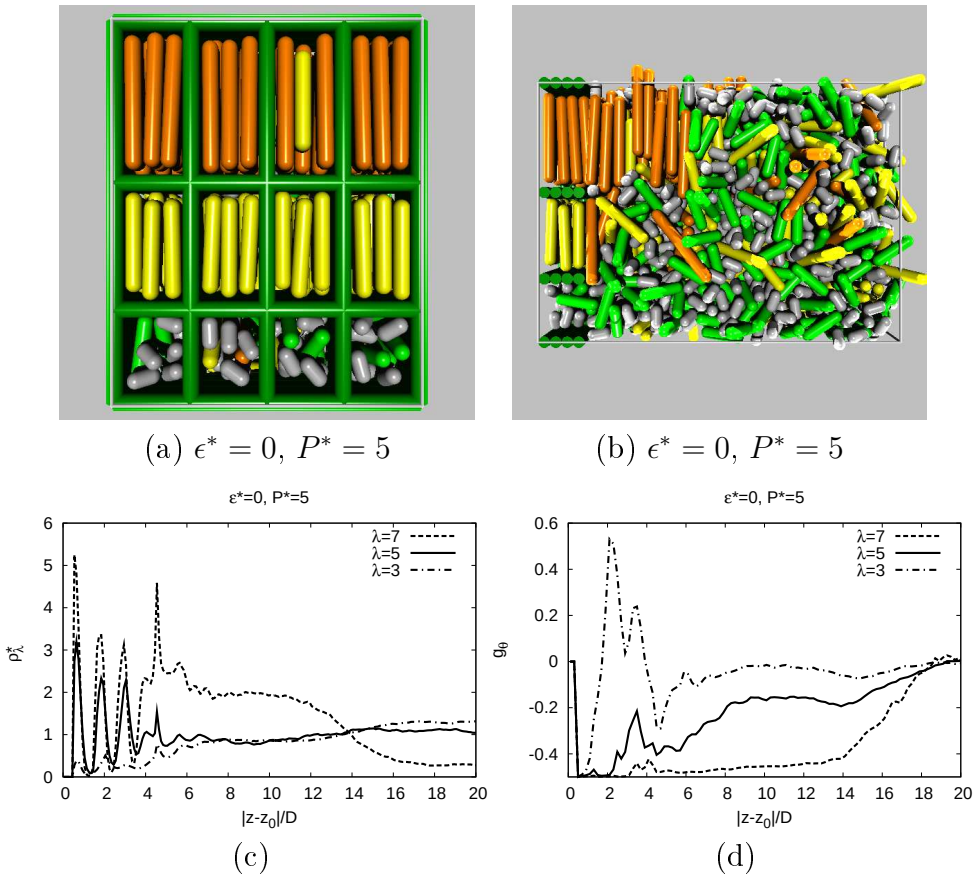

Figure 4.34: (a) Bottom view and (b) side view of the simulation box of the 7531 mixture at $P^* = 5$ in contact with cavities of alternating length. (c) The density distribution ρ^*_λ and (d) the orientational correlation function g_θ as a function of the distance $|z - z_0|$ to the wall.

Chapter 5

Summary and outlook

In this work, collective behavior of colloidal rods has been investigated with the help of Monte Carlo simulations concerning the phase behavior and structure formation in bulk systems and substrate induced effects. For polydisperse systems, nucleation and substrate induced fractionation has been studied. The influence of attractive and hard rods has been compared. The attractive rod potential for spherocylinders of Bolhuis *et al.* [8] has therefore been extended for arbitrary rod lengths to investigate polydisperse suspensions of colloidal rods. An effective method to calculate U_{AR} is derived in Appendix A.

In Section 3.1, we investigated the bulk behavior of monodisperse systems with axis ratios $\lambda = 3$ to $\lambda = 8$ for different interaction strengths and presented isotherms as a function of the reduced pressure P^*. In some cases, the first order phase transitions were accompanied by a strong hysteresis. We therefore applied biased multi-histogram sampling to explore the relevant part of the free energy landscape and to identify the thermodynamically stable phases. With the obtained results, we also could estimate the surface tension between the nematic and the hexatic phase. The structure of all involved phases was analyzed in more detail with suitable pair correlation functions. A comprehensive overview of the phase behavior of monodisperse systems was provided by phase diagrams in the $P^*\lambda$-plane. At low interaction strengths, the nematic and the smectic A phase exists in a relatively large pressure range. The nematic phase broadens with increasing axis ratio λ. At larger interaction strengths, the hexatic phase is predominant. With increasing axis ratio λ, the hexatic phase sets in at decreasing pressure. The nematic and the smectic A phase are lens shaped.

In Section 3.2, a tridisperse mixture of hard and attractive rods was investigated, which features many aspects of polydisperse systems. The spatial and orientational order in the system was studied separately for each rod

length. We observed a distinct dependence of the structure formation on the interaction strength of the potential. With attraction, a monolayer with long-range hexatic in-plane order of long rods forms, which is surrounded by an isotropic fluid of shorter rods. For hard rods, order sets in at higher pressure and the structure formation is less pronounced. The pair correlation functions revealed the structure of a nematic fluid. Thus, layer formation like for attractive rods is absent and fractionation is negligible.

The influence of attractivity has also been studied in a more realistic length-polydisperse suspension of rods in Section 3.3. The observations for the polydisperse mixture basically resemble those of the tridisperse mixture. With sufficiently strong interactions, we found the formation of a hexatic monolayer surrounded by an isotropic fluid. A strong fractionation occurs with mainly long rods incorporated in the hexatic monolayer and shorter rods accumulate in the isotropic fluid. In the case of hard rods, we found the formation of a nematic droplet of mainly long rods resulting in a moderate fractionation, which was not observed for the tridisperse mixture. The fractionation in the polydisperse systems is strongly enhanced by attractive interactions. A monolayer formation with long-range order was also observed experimentally is supensions of fd viruses [22]. In these experiments, attractive interactions were provided by depletion forces induced by non-adsorbing PEG polymers in the solution.

In Chapter 4, the tridisperse and the polydisperse suspension were studied in contact with (structured) substrates. The main results were obtained for low ($P^* = 0.5$) and high ($P^* = 4$) pressure in hard rod systems. Note that the corresponding bulk systems of hard rods are isotropic at the considered pressures. Again, we started with the tridisperse mixture, which is easier to discuss. Special attention was paid on the fluid structure near the wall in the low and high pressure region and on the influence of differently patterned substrates concerning spatial fractionation. The following results were obtained at low pressure: For the planar wall the density of short rods is larger in the substrate proximity and a layer formation of longer rods is strongly suppressed. For walls with parallel grooves, a larger density of short rods exists in broad grooves whereas in narrow grooves the density of long rods is largest. Rectangular cavities of different size do not change the fluid structure in a significant way in the low pressure regime. A very different behavior is found at high pressure for all substrate types. Close to a planar wall, we observed a multilayer coverage with the density of long rods enhanced in the layers. In systems with grooves, the multilayer formation sustains inside the grooves and long rods contribute most. The observed effects in broad and narrow grooves are alike, now. For cavities, however, the fluid structure inside the cavities depends distinctly on the dimension of

the cavities. In long cavities, we observed layer formation of almost exclusively long rods. Cavities of intermediate length induce layer formation of the medium sized rods while shorter cavities are filled with homeotropically aligned short and long rods. In terms of a substrate controlled fractionation, cavities provide by far the best control over the length distribution at the substrate. Rectangular cavities also represent an example of purely geometric molecule recognition. The majority of substrate investigations were done for the hard rod model. At $P^* \lesssim 2.9$, attractive and hard rods behave qualitatively similar. For $P^* \gtrsim 2.9$, a hexatic monolayer forms in bulk systems of attractive rods. Except for very unsuitable substrate patterns, the hexatic monolayer adheres at the substrate at pressure $P^* = 3.5$.

All three investigated substrate types have also been studied in contact with a polydisperse mixture. The results for the tridisperse suspension are confirmed in the low and high pressure regime. For example, cavities are mainly filled with the longest rods that fit inside and the density of shorter rods is reduced markedly in the cavities at high pressure. Finally, we turned towards alternating cavity patterns. We demonstrated how patterns can be constructed to induce an alternating substrate coverage of long and short rods and that smectic monolayers can be spatially fixated.

In the future, a variety of new or continuative aspects can be investigated. The biased multi-histogram simulations could be employed to determine the surface tensions for various types of systems. By controlling the shape of the interface with suitable bias potentials it should be possible to measure all surface tensions. So far, the hexatic phase in monodisperse bulk systems was not specified in detail. The question whether it is a liquid crystalline smectic B phase or the solid phase is still open but also far from trivial. It would also be interesting to test the comparability of the attractive rod potential and systems with an explicit consideration of depletion forces - regarding the percolation transition in dilute systems, for example. The studies with adjacent substrates could be extended to an even higher pressure regime where phase separation is expected. It would be interesting to see the impact of the different substrate types on the transition point and on the fluid structure using, for example, grand canonical ensemble Monte Carlo simulations. The various substrate patterns can also be studied concerning their influence on selfassembling rods.

Appendix A

Attractive part of the rod potential

The attractive part of the attractive rod (AR) potential given in Eq. (2.17) is obtained by integrating the attractive part $U^a(\cdot)$ of the square-well potential $U^{sw}(\cdot)$ over all pairs of locations on the cylinder axes of rods i and j. In Eq. (2.17) the cylinder axes are parameterized by α_i and α_j. It is convenient to use the step function $\Theta(x)$ to write down the integral. If the rods i and j have cylinder lengths L_i and L_j, the integration area in the α_i, α_j space is restricted to a rectangle with $-L_i/2 \leq \alpha_i \leq L_i/2$, $-L_j/2 \leq \alpha_j \leq L_j/2$, which we denote with R for convenience. With the step function

$$\Theta(r) = \begin{cases} 0 & \text{, if } r < 0 \\ 1 & \text{, if } r \geq 0 \end{cases} \tag{A.1}$$

Eq. (2.17) can be written as

$$U_r^a = -\frac{\epsilon}{D^2} \int_R \mathrm{d}\alpha_i \, \mathrm{d}\alpha_j \Theta\left(D_a^2 - (\mathbf{r}_{ij} + \alpha_j \mathbf{u}_j - \alpha_i \mathbf{u}_i)^2\right). \tag{A.2}$$

with the cut-off radius D_a. The prefactor ϵ represents the interaction strength.

The cylinder axis of rod i is a subset of the infinite straight line, that includes $\mathbf{r}_i$ and is parallel to $\mathbf{u}_i$. A respective straight line includes the cylinder axis of rod j. The vector of shortest distance $\mathbf{s}_{ij}$ between these straight lines can be written as

$$\mathbf{s}_{ij} = \mathbf{r}_{ij} - \mu_i \, \mathbf{u}_i + \mu_j \, \mathbf{u}_j \tag{A.3}$$

with parameters μ_i and μ_j. Since $\mathbf{s}_{ij}$ is perpendicular to $\mathbf{u}_i$ and $\mathbf{u}_j$, one has

$$\mu_i = \frac{\mathbf{r}_{ij} \cdot \mathbf{u}_i - \mathbf{r}_{ij} \cdot \mathbf{u}_j \, \mathbf{u}_i \cdot \mathbf{u}_j}{1 - (\mathbf{u}_i \cdot \mathbf{u}_j)^2} \tag{A.4}$$

$$\mu_j = \frac{-\mathbf{r}_{ij} \cdot \mathbf{u}_j + \mathbf{r}_{ij} \cdot \mathbf{u}_i \, \mathbf{u}_i \cdot \mathbf{u}_j}{1 - (\mathbf{u}_i \cdot \mathbf{u}_j)^2}. \tag{A.5}$$

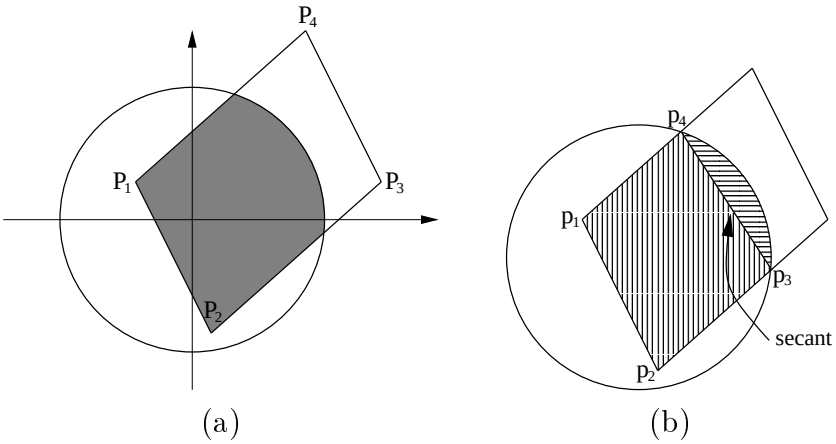

Figure A.1: (a) Calculating U_r^a is equivalent with finding the overlap of the unit circle and the parallelogram with vertices $\{P_1, P_2, P_3, P_4\}$. (b) The desired area can be split into a polygon inside the unit circle and segments of a circle.

Defining

$$s_- \equiv \sqrt{\frac{1 - \mathbf{u}_i \cdot \mathbf{u}_j}{D_a^2 - s_{ij}^2}} \tag{A.6}$$

and

$$s_+ \equiv \sqrt{\frac{1 + \mathbf{u}_i \cdot \mathbf{u}_j}{D_a^2 - s_{ij}^2}}, \tag{A.7}$$

the integral in Eq. (A.2) can be simplified with the help of a coordinate transformation from (α_i, α_j) to $(\lambda_i, \lambda_j) = T(\alpha_i, \alpha_j)$ with

$$T(\alpha_i, \alpha_j) = \frac{1}{\sqrt{2}} \begin{pmatrix} s_- & s_- \\ s_+ & -s_+ \end{pmatrix} \begin{pmatrix} \alpha_i + \mu_i \\ \alpha_j + \mu_j \end{pmatrix}. \tag{A.8}$$

Using the variables (λ_i, λ_j), Eq. (A.2) becomes

$$U_r^a = -\frac{\epsilon}{D^2} \frac{1}{s_- \, s_+} \int_{T(R)} \mathrm{d}\lambda_i \, \mathrm{d}\lambda_j \, \Theta\left(1 - \left(\lambda_i^2 + \lambda_j^2\right)\right). \tag{A.9}$$

The argument of the step function in Eq. (A.9) is larger than zero only in the unit circle. The rectangle R is transformed into the parallelogram $T(R)$ with the vertices $\{P_1, P_2, P_3, P_4\}$. Thus, calculating U_r^a is equivalent with finding the overlap area of the unit circle with the parallelogram $T(R)$ as depicted in Fig. A.1 (a).

For $L_i = L_j$ one obtains the overlap area of a unit circle and a lozenge [8].

The overlap area can generally be split into a polygon $\{p_1, \ldots, p_{N_{\text{poly}}}\}$ inside the unit circle and up to four segments of a circle (Fig. A.1 (b)). In order to obtain the N_{poly} vertex points $p_1, \ldots, p_{N_{\text{poly}}}$ we consider the lines

$$g_i(x_i) = \frac{P_{i+1} + P_i}{2} + x_i \frac{P_{i+1} - P_i}{2}, \quad i = 1, .., 4 \tag{A.10}$$

where $P_5 = P_1$. The boundaries of $T(R)$ are characterized by $x_i \in [-1; 1]$. The intersection points $\tilde{x}_{i,\pm}$ of the unit circle and the lines g_i are given by

$$g_i(\tilde{x}_{i,\pm})^2 - 1 = 0, \quad i = 1, \ldots, 4. \tag{A.11}$$

The polygon vertices p_j can be found by subsequently considering g_1, g_2, g_3 and g_4. If $\tilde{x}_{1,\pm}$ are complex, then g_1 does not intersect with the unit sphere and includes no polygon vertices. Otherwise one or two of the three points P_1, $g_1(\tilde{x}_{1,-})$ and $g_i(\tilde{x}_{1,+})$ are vertices of the polygon. (The improbable case $\tilde{x}_{1,+} = \tilde{x}_{1,-}$ can be subsumed.) If P_1 is within the unit circle, P_1 is a polygon vertex. Otherwise, $g_1(\tilde{x}_{1,-})$ is a polygon vertex if $\tilde{x}_{1,-} \,\epsilon\, [-1; 1]$. The next polygon vertex is $g_1(\tilde{x}_{i,+})$ if $\tilde{x}_{1,+} \,\epsilon\, [-1; 1]$. If the same procedure is repeated for g_2, g_3 and g_4, all N_{poly} vertices p_k of the polygon are obtained in a counterclockwise order, due to the definition of the lines g_i. The area of the polygon is easily calculated as

$$A_{\text{poly}} = -\frac{1}{2} \sum_{k=1}^{N_{\text{poly}}-1} p_k^x \, p_{k+1}^y - p_k^y \, p_{k+1}^x \tag{A.12}$$

If a '+'-solution $g_n(\tilde{x}_{n,+})$ is being followed by a '-'-solution $g_m(\tilde{x}_{m,-})$, a secant is determined by these points. The corresponding segment of a circle is

$$A_{\text{sec}} = \arcsin\left(\frac{c}{2}\right) - \frac{1}{2} \sin\left(2 \arcsin\left(\frac{c}{2}\right)\right) \tag{A.13}$$

with $c = |g_n(\tilde{x}_{n,-}) - g_m(\tilde{x}_{m,+})|$.

Finally, we mention two special cases. If $N_{\text{poly}} = 0$, there is either no overlap or the whole circle is within the parallelogram. In the case $N_{\text{poly}} = 2$ the overlap area is the segment of the unit circle that is characterized by the two intersection points and overlaps with the parallelogram.

With these results the attractive part of the AR potential is given by

$$U_r^a = -\frac{\epsilon}{D^2} \frac{1}{s_- \, s_+} \left(A_{\text{poly}} + \sum A_{\text{sec}}\right). \tag{A.14}$$

Appendix B

Correlations in RAN3

The following code shows the typical sequence of random number generation in the simulation program.

```
#include <iostream>
using namespace std;

long seed=-24332;//initial seed
long N=1000;//number of particles
double ran3(long *idum);
//generates a random floating point number in the interval [0,1)
int i_ran3(long *idum, int N_too_high);
//Return a random integer value in the range [0,N_too_high-1]
void random_unit_vec();

int main(){
  ran3(&seed);//initialization of the random number generator
  double dx[3];//cummulative displacement vector
  dx[0]=dx[1]=dx[2]=0;

  for(int i=0;i<100000;i++){
    for(int j=0;j<10000;j++){

      int r=i_ran3(&seed,N);//choose particle randomly
      int flag=i_ran3(&seed,3);//choose Monte Carlo step

      switch(flag){
      case 0://move particle
        dx[0] += (ran3(&seed)-0.5);//displacement vector
        dx[1] += (ran3(&seed)-0.5);
        dx[2] += (ran3(&seed)-0.5);
```

```
        ran3(&seed);//acceptance probability
        break;
      case 1://rotate particle
        random_unit_vec();//random axis of rotation
        ran3(&seed);//random rotation angle
        ran3(&seed);//acceptance probability
        break;
      case 2://move and rotate particle
        random_unit_vec();
        ran3(&seed);
        dx[0] += (ran3(&seed)-0.5);
        dx[1] += (ran3(&seed)-0.5);
        dx[2] += (ran3(&seed)-0.5);
        ran3(&seed);
      }
    }
    cout << dx[0] << '\t' << dx[1] << '\t' << dx[2] << endl;
  }
  return 0;
}

void random_unit_vec(){
  double vrnd[3];
  double l_vrnd;
  while(true){
    vrnd[0]=2.0*ran3(&seed)-1.0;
    vrnd[1]=2.0*ran3(&seed)-1.0;
    vrnd[2]=2.0*ran3(&seed)-1.0;
    l_vrnd = vrnd[0]*vrnd[0] + vrnd[1]*vrnd[1] + vrnd[2]*vrnd[2];
    if(l_vrnd<=1.0) break;
  }
}

//============= the random number generator ran3 ===========
#define MBIG 1000000000
#define MSEED 161803398
#define MZ 0
#define FAC (1.0/MBIG)
double ran3(long *idum){
  static int inext,inextp;
  static long ma[56];
  static int iff=0;
  long mj,mk;
```

```
  int i,ii,k;
  if (*idum < 0 || iff == 0) {
    iff=1;
    mj=labs(MSEED-labs(*idum));
    mj %= MBIG;
    ma[55]=mj;
    mk=1;
    for (i=1;i<=54;i++) {
      ii=(21*i) % 55;
      ma[ii]=mk;
      mk=mj-mk;
      if (mk < MZ) mk += MBIG;
      mj=ma[ii];
    }
    for (k=1;k<=4;k++)
      for (i=1;i<=55;i++) {
        ma[i] -= ma[1+(i+30) % 55];
        if (ma[i] < MZ) ma[i] += MBIG;
      }
    inext=0;
    inextp=31;
    *idum=1;
  }
  if (++inext == 56) inext=1;
  if (++inextp == 56) inextp=1;
  mj=ma[inext]-ma[inextp];
  if (mj < MZ) mj += MBIG;
  ma[inext]=mj;
  return mj*FAC;
}

int i_ran3(long *idum, int N_too_high){
  int iran;
  iran=(int)(ran3(idum)*N_too_high);
  if (iran>=N_too_high) iran=(N_too_high-1);
  return iran;
}
#undef MBIG
#undef MSEED
#undef MZ
#undef FAC
```

The volume move is omitted since it does not change the outcome considerably. Many MC simulation codes may have the same structural setup. The

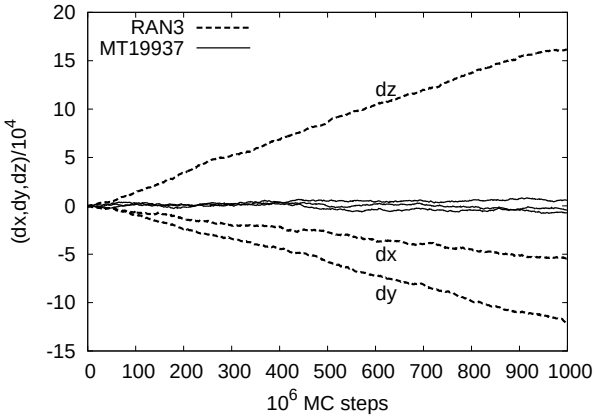

Figure B.1: The three components of the cumulative displacement vector. RAN3 gives rise to a pronounced drift in all three components. MT19937 generates the expected random behavior.

quantity of interest is the cumulative displacement vector `dx[3]`. In the inner loop of the program, random numbers are generated in the symmetric interval $[-1/2, +1/2]$ as this is the case for any particle displacement move. Every generated displacement vector is cumulated in `dx[3]`. An uncorrelated sequence of random numbers would create a random walk in 3D with the modulus of `dx[3]` averaged over many runs with different seeds proportional to the square root of the MC steps. Fig. B.1 displays the components of the cumulative displacement vector generated with the code shown above (**– – –**) and when MT19937 is used instead of RAN3 (**——**). `dx[3]` has a very strong drift in the first case. This observation is quite robust against slight modifications of the code (e. g. removing the random numbers, which are needed for the acceptance probability). Other values for the seed lead to comparable results. MT19937 produces no obvious artifacts and and is thus considered as appropriate.

Appendix C

Rescaling of the nematic order parameter for small numbers of rods

In simulations, the orientational order parameter S of a system of anisotropic molecules is typically obtained by averaging the largest eigenvalue $\lambda_{\max}$ of the alignment tensor Q (Eq. (2.37)) over many configurations. In order to compare the orientational order of two systems with different numbers of rods N, a system-size independent order parameter is desirable. However, the value of $\langle\lambda_{\max}(N)\rangle$ turns out to be size-dependent. Especially, for small amounts of rods with an isotropic distribution, one usually gets $\langle\lambda_{\max}(N)\rangle > 0$. Eppenga and Frenkel[24] investigated the N dependence of the eigenvalues of Q by studying the eigenvalue problem of the tensor

$$M \equiv \frac{1}{N}\sum_i \mathbf{u}_i\mathbf{u}_i, \tag{C.1}$$

which has the same eigenvectors as Q. The eigenvalues μ_n of M and λ_n of Q are related by $\mu_n = 2\lambda_n/3 + 1/3$. The characteristic equation

$$\det\left(M - \mu\mathbb{I}\right) = 0 \tag{C.2}$$

can also be written as

$$-\mu^3 + \mu^2 + c_1\mu + c_0 = 0, \tag{C.3}$$

where c_0 and c_1 are functions of the rod orientations. The order parameter $S(n) = (3\langle\mu_{\max}\rangle - 1)/2$ depends on the largest root $\mu_{\max}$ of Eq. (C.3) averaged over many configurations. Finding an analytic expression for this average

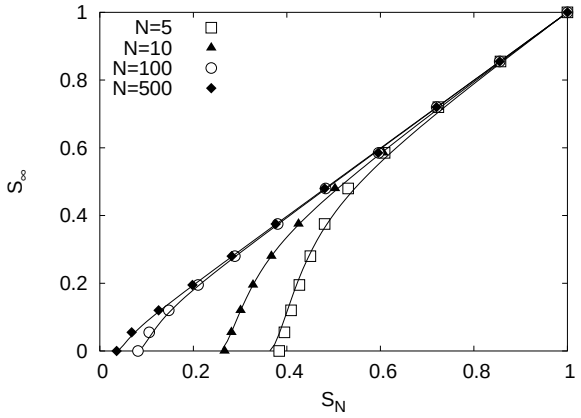

Figure C.1: Orientational order parameter S_∞ for an infinite number of rods compared to a corresponding order parameter $S(N)$ for a system of N rods. The solid line shows the fitting function (Eq. (C.6)), which allows to map $S(N)$ onto S_∞. Symbols are averages of $S(N)$ in ideal systems of N rods with known S_∞. The dashed lines correspond to the approach of Eppenga and Frenkel for $N = 5$ and $N = 10$, respectively. Both methods coincide for $N = 100$ and $N = 500$ (not shown).

is extremely difficult, if not impossible. Eppenga and Frenkel simplify the problem by solving Eq. (C.3) for the coefficients $\langle c_0 \rangle$ and $\langle c_1 \rangle$ and obtain for $\lambda = 3\mu/2 - 1/2$ the equation

$$\lambda^3 - \frac{3}{4}\frac{\lambda}{N}\left(1 + S_{\text{resc}}^2(N-1)\right) - \frac{S_{\text{resc}}^3}{4} - \frac{3(S_{\text{resc}}^2 - S_{\text{resc}}^3)}{4N} - \\ - \frac{1 - 3S_{\text{resc}}^2 + 2S_{\text{resc}}^3}{4N^2} = 0 \tag{C.4}$$

where S_{resc} corresponds to the rescaled order parameter, i.e. the value in the infinite system. With $S(N) \approx \lambda$ Eq. (C.4) provides a relation between $S(N)$, N and S_{resc}.

The accuracy of this method can be tested numerically, by calculating $S(N)$ for a system of N non-interacting rods. The rods are randomly distributed with a rotationally symmetric distribution $f(\cos(\theta))$ around the z axis $\mathbf{e_z}$ where $\cos(\theta) = \mathbf{u} \cdot \mathbf{e_z}$. A comparison between $S(N)$ and the order parameter

$$S_\infty = \int \mathrm{d}(\cos\theta)\, P_2(\cos\theta)\, f(\cos\theta) \tag{C.5}$$

for an infinite system is shown in Fig. C.1 for various N and different distributions $f(\cos(\theta))$. It shows that $S(N)$ and S_∞ differ especially for low

orientational order. The approach by Eppenga and Frenkel works well for not too small numbers of rods. For $N \leq 10$ deviations from the numeric result can be seen. Using the numerical results, we define a fit function, which serves only two purposes: It is rather simple and it fits the numerical data down to small N. Both is fulfilled by

$$S_\infty \approx S(N)\left(1 - \gamma^{-1}(S(N), N)\right) \tag{C.6}$$

with

$$\gamma(S(N), N) \equiv 1 + 25\sqrt{N}\frac{\left(S(N) - S^i(N)\right)^{5/3}}{1 - S(N)} \tag{C.7}$$

where $S^i(N) \approx 0.81/\sqrt{N}$ denotes $S(N)$ for a system of N isotropically oriented rods with $f(\cos(\theta)) = const.$ Note that S_∞ gets 1 for $S(N) = 1$ while S_∞ vanishes for $S(N) = S^i(N)$, the minimum value of $S(N)$ as shown in Fig. C.1. The fit function in Eq. (C.6) is used to calculate S_∞ from values of $S(N)$ sampled in the simulations. For $S(N) < S_i(N)$, Eq. (C.7) – as well as Eq. (C.4) – provides a complex solution. In the rare cases where this happened $|S(N) - S_i(N)|$ turned out to be small and we set $S_\infty = 0$.

Appendix D

Surface tension between a hexatic and a nematic phase

The surface tension can be extracted from the graph in Fig. D.1. For conve-

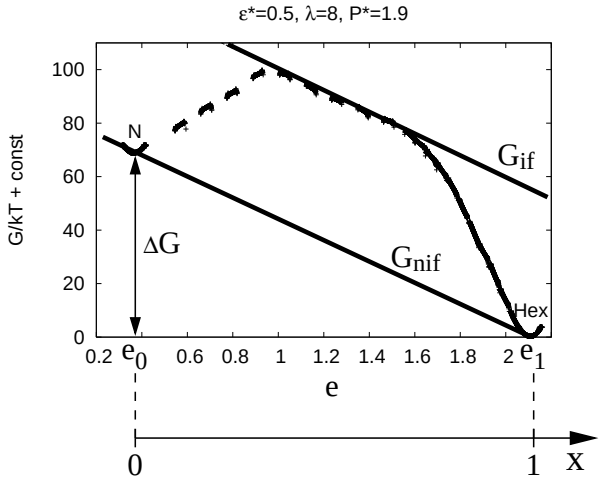

Figure D.1: Free energy profile as function of the internal energy e. The internal energy e has to be mapped on the 'good' order parameter x.

nience we introduce $e \equiv \langle E_{\rm rod} \rangle / E_{\rm min}$. e_0 corresponds to the internal energy per rod in the nematic phase and e_1 to the internal energy per rod in the hexatic phase. We consider the two straight lines $G_{\rm if}$ and $G_{\rm nif}$. $G_{\rm if}$ corresponds to the free energy of a system with an interface between the nematic and the hexatic phase and $G_{\rm nif}$ gives the free energy with no interface between the phases. The offset $\Delta G_s = G_{\rm if} - G_{\rm nif}$ of the two straight lines gives the free energy related to the interface. If the chosen order parameter e would be a

'good' order parameter, the interfacial free energy ΔG_s would be related to the surface tension σ via $\Delta G_s = \sigma A_s$ where A_s is the interfacial area. The specific choice of the internal energy e as order parameter, however, requires a correction, which is due to the fact that the internal energy of a system with fixed size of the nematic and the hexatic region would be different with and without interface. To see this, we map the free energies G_{if} and G_{nif} on a 'good' order parameter x, which is 0 in the nematic and 1 in the hexatic phase (cmp. Fig. D.1):

$$G_{\text{if}}(x) = \Delta G - \Delta G\, x + \sigma A_s \tag{D.1}$$
$$G_{\text{nif}}(x) = \Delta G - \Delta G\, x. \tag{D.2}$$

The same has to be done for the internal energies e_{if} and e_{nif}:

$$e_{\text{if}}(x) = e_0 + (e_1 - e_0)\, x + e_s \tag{D.3}$$
$$e_{\text{nif}}(x) = e_0 + (e_1 - e_0)\, x. \tag{D.4}$$

e_s is change in internal energy because of the interface. Resolving Eqs. (D.3) and (D.4) for x and substitution in Eqs. (D.1) and (D.2) yields

$$\Delta G_s = \sigma A_s + \Delta G \frac{e_s}{e_1 - e_0}, \tag{D.5}$$

where the second term on the right hand side is the correction for two systems, which are compared at $e_{\text{if}} = e_{\text{nif}}$.

In the following we estimate e_s. Therefore, we assume that rods in the interfacial region are in contact with about 1/4 of their contact zone with the corresponding other phase. Fig. D.2 illustrates the situation. The drawing

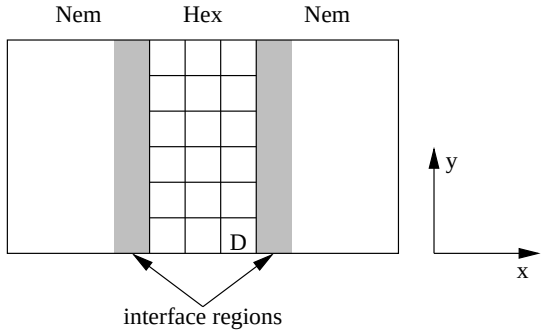

Figure D.2: Estimation of the interfacial energy e_s. The drawing is schematic for a simulation box like in Fig. 3.2 (c) on page 38. The view is along the negative z-axis.

shows a top view on the hexatic region, i. e. the rods point out of the plane. The width of the interfacial region in x-direction is estimated as one rod diameter D. Thus, the volume of the interface region is about $V_{\rm if} = 2\,L_y L_z D$, if $L_{x,y,z}$ denotes the box dimension in the respective direction. The internal energy of the interface is then roughly given by

$$e_s = \frac{1}{4}\frac{V_{\rm if}}{V}(e_1 - e_0) \tag{D.6}$$

$$= \frac{D}{2\,L_x}(e_1 - e_0). \tag{D.7}$$

From Eqs. (D.5) and (D.7) we find $\sigma = 0.062kT/D^2$. Note that the correction because of e_s is very small. An estimate of the surface tension in the naive way as $\sigma = \Delta G_s/A_s$ would yield $0.063kT/D^2$.

Bibliography

[1] D. Akcakayiran, D.G. Kurth, S. Röhrs,G. Rupprechter, and G.H. Findenegg, Langmuir, **21**, 7501 (2005).

[2] S. Auer and D. Frenkel, Nature, **409**, 1020 (2001).

[3] M.A. Bates and D. Frenkel, J. Chem. Phys., **109**, 6193 (1998).

[4] M.A. Bates and G.R. Luckhurst, J. Chem. Phys., **110**, 7087 (1999).

[5] C.H. Bennett, J. Comp. Phys., **22**, 245 (1976).

[6] L. Belloni, J. Phys.: Condens. Matter, **12**, R549 (2000).

[7] P.G. Bolhuis, and D. Frenkel, J. Chem. Phys., **106**, 666 (1997).

[8] P.G. Bolhuis, A. Stroobants, D. Frenkel, and H.N.W. Lekkerkerker, J. Chem. Phys., **107**, 1551 (1997).

[9] J.T. Brown, M.P. Allen, E.M. del Rio, and E. de Miguel, Phys. Rev. E, **57**, 6685 (1998).

[10] P.A. Buining, C. Pathmamanoharan, J.B.H. Jansen, and H.N.W. Lekkerkerker, J. Am. Ceram. Soc., **74**, 1013 (1991).

[11] S. Chandrasekhar, *Liquid Crystals, 2nd edition*, (Cambridge University Press, 1992).

[12] R. Chelakkot, T. Gruhn, and R. Lipowsky, Macromolecules, **39**, 7138 (2006).

[13] L. Chen, L. Zhuang. P. Deshpande, and S. Chou, Langmuir, **21**, 818 (2005).

[14] G. Cinacchi, L. Mederos, and E. Velasco, J. Chem. Phys., **121**, 3854 (2004).

[15] N. Clarke, J.A. Cuesta, R. Sear, P. Sollich, and A. Speranza, J. Chem. Phys., **113**, 5817 (2000).

[16] A. Cuetos, B. Martinez-Haya, L.F. Rull, and S. Lago, J. Chem. Phys., **117**, 2934 (2002).

[17] P.G. de Gennes and J. Prost, *The physics of liquid crystals, 2nd edition*, (Clarendon Press, Oxford, 1993).

[18] E. de Miguel, E.M. del Rio, J.T. Brown, and M.P. Allen, J. Chem. Phys., **105**, 4234 (1996).

[19] E. de Miguel, E.M. del Rio, and F.J. Blas, J. Chem. Phys., **121**, 11183 (2004).

[20] M.R. Diehl, S.N. Yaliraki, R.A. Beckman, M. Barahona, and J.R. Heath, Angew. Chem. Int. Ed., **41**, 353 (2002).

[21] M. Dijkstra, R. van Roij, and R. Evans, Phys. Rev. E., **63**, 051703 (2001).

[22] Z. Dogic and S. Fraden, Philos. Trans. R. Soc. London, Ser. A **359**, 997 (2001).

[23] M.T. Downtown and M.P. Allen, Europhys. Lett., **65**, 48 (2004).

[24] R. Eppenga and D. Frenkel, Mol. Phys., **52**, 1303 (1984).

[25] P. Feng, Q. Wan, and T.H. Wang, Appl. Phys. Lett., **87**, 213111 (2005).

[26] F.C. Frank, Discuss. Faraday Soc., **25**, 19 (1958).

[27] D. Frenkel, B. Smit, *Understanding molecular simulation, 2nd edition*, (Academic Press, California, 2002).

[28] J.G. Gay and B.J. Berne, J. Chem. Phys., **74**, 3316 (1981).

[29] M. Geissler and Y. Xia, Adv. Mater. **16**, 1249 (2004).

[30] H. Goldstein, *Classical mechanics, 2nd edition*, (Addison-Wesley, 1980).

[31] H. Graf and H. Löwen, J. Phys.: Condens. Matter, **11**, 1435 (1999).

[32] J.J. Gray and R.T. Bonnecaze, J. Chem. Phys., **114**, 1366 (2001).

[33] T. Gruhn and M. Schoen, Phys. Rev. E, **55**, 2861 (1997).

[34] T. Gruhn and M. Schoen, J. Chem. Phys., **108**, 9124 (1998).

[35] L. Harnau, S. Kondrat, and A. Poniewierski, Phys. Rev. E, **72**, 011701 (2005).

[36] S. Iijima, Nature, **354**, 56 (1991).

[37] S.H.L. Klapp and M. Schoen, J. Chem. Phys., **117**, 8050 (2002).

[38] D.A. Kofke and P.T. Cummings, Mol. Phys., **92**, 973 (1997).

[39] F.M. van der Kooij, D. van der Beek, and H.N.W. Lekkerkerker, J. Phys. Chem. B, **105**, 1696 (2001).

[40] E. Krämer, S. Förster, C. Göltner, and M. Antonietti, Langmuir, **14**, 2027 (1998).

[41] S. Kumar, Chem. Soc. Rev., **35**, 83 (2006)

[42] D.G. Kurth, N. Severin, and J.P. Rabe, Angew. Chem. Int. Ed. 41, **19**, 3681 (2002).

[43] S. Kondrat, A. Poniewierski,and L. Harnau, Eur. Phys. J. E, **10**, 163 (2003).

[44] S. Kondrat, A. Poniewierski, and L. Harnau, Liq. Cryst., **32**, 95 (2005).

[45] L.D. Landau and J.M. Lifschitz, *Lehrbuch der theoretischen Physik (Band 5), 8th edition*, (Akademie-Verlag Berlin 1979/1987).

[46] H.N.W. Lekkerkerker and G.J. Vroege, Phil. Trans. R. Soc. Lond. A, **344**, 419 (1993).

[47] G.T. Linke, R. Lipowsky, and T. Gruhn, Phys. Rev. E, **71**, 051602 (2005).

[48] W. Li and H.R. Ma, Eur. Phys. J. E, **16**, 225 (2005).

[49] a) W. Maier and A. Saupe, Z. Naturforsch., **A13**, 564 (1958).
b) W. Maier and A. Saupe, Z. Naturforsch., **A14**, 882 (1959).
c) W. Maier and A. Saupe, Z. Naturforsch., **A15**, 287 (1960).

[50] B. Martinez-Haya, A. Cuetos, and S. Lago, Phys. Rev. E, **67**, 051201 (2003).

[51] B. Martinez-Haya, A. Cuetos, S. Lago, and L.F. Rull, J. Chem. Phys., **122**, 024908 (2005).

[52] A. Matsuyama and T. Kato, Eur. Phys. J. E, **6**, 15 (2001).

[53] a) M. Matsumoto and T. Nishimura, ACM Trans. Modeling Comput. Simul., **8**, 3 (1998).
b) `http://www.math.sci.hiroshima-u.ac.jp/~m-mat/MT/emt.html`.

[54] N. Metropolis, A.W. Rosenbluth, M.N. Rosenbluth, A.N. Teller, and E. Teller, J. Chem. Phys., **21**, 1087 (1953).

[55] A. Miniewicz, A. Gniewek, and J. Parka, Optical Materials, **21**, 605 (2002).

[56] P. Model and M. Russel, Filamentous bacteriophage, In: *The bacteriophages*, edited by R. Calendar, (Plenum Press, New York, 1988).

[57] L. Onsager, Ann. N.Y. Acad. Sci. **51**, 627 (1949).

[58] F. Oosawa and S. Asakura, J. Chem. Phys., **22**, 1255 (1954).

[59] C.W. Oseen, Trans. Faraday Soc., **29**, 883 (1933).

[60] A.Z. Panagiotopoulous, Mol. Phys., **61**, 813 (1987).

[61] A.Z. Panagiotopoulous, Mol. Phys., **63**, 527 (1988).

[62] A. Poniewierski, Phys. Rev. E, **47**, 3396 (1993).

[63] F. Porcheron, M. Schoen, and A.H. Fuchs, J. Chem. Phys., **116**, 5816 (2002).

[64] W.H. Press, S.A. Teukolsky, W.T. Vetterling, and B.P. Flannery, *Numerical recipes in C, 2nd edition*, (Cambridge University Press, 1988).

[65] P.K. Rai, R.A. Pinnick, A.N.G. Parra-Vasquez, V.A. Davis, H.K. Schmidt, R.H. Hauge, R.E. Smalley, and M Pasquali, J. Am. Chem. Soc., **128**, 591 (2006).

[66] F. Reinitzer, Monatsch. Chem., **9**, 421 (1888).

[67] A. Richter and T. Gruhn, J. Chem. Phys., **112**, 064908 (2006).

[68] A. Richter and T. Gruhn, Mol. Phys., accepted.

[69] S.S. Rogers, P. Venema, L.M.C. Sagis, E. van der Linden, A.M. Donald, Macromolecules, **38**, 2948 (2005).

[70] L.F. Rull, G. Jackson, and B. Smit, Mol. Phys., **85**, 435 (1995)

[71] M. Schadt and W. Helfrich, Appl. Phys. Lett., **18**, 127 (1971).

[72] M. Schadt, Annu. Rev. Mater. Sci., **27**, 305 (1997).

[73] T. Schilling and D. Frenkel, Phys. Rev. Lett., **92**, 085505 (2004).

[74] A.D. SchlÃ$\frac{1}{4}$ter and J.P. Rabe, Angew. Chem. Int. Ed. 39, **5**, 864 (2000).

[75] F. Schmid and N.B. Wilding, Int. J. Mod. Phys. C, **6**, 781 (1995).

[76] R.P. Sear, Phys. Rev. E, **57**, 1983 (1998).

[77] T.J. Sluckin, Contemporary Physics, **41**, 37 (2000).

[78] A. Speranza and P. Sollich, Phys. Rev. E, **67**, 061702 (2003).

[79] H. Steuer, S. Hess, and M. Schoen, Phys. Rev. E, **69**, 031708 (2004).

[80] A. Stroobants, J. Phys.: Condens. Matter, **6**, A285 (1994).

[81] B. Sun and H. Sirringhaus, Nano Lett., **5**, 2408 (2005).

[82] Y. Sun, H. Ma, Z. Zhang, and S. Wu, J. Appl. Phys., **92**, 1956 (2002).

[83] K. Tarumi, M. Bremer, and T. Geelhaar, Annu. Rev. Mater. Sci., **27**, 423 (1997).

[84] M. Tokushima, H. Yamada, and Y. Arakawa, Appl. Phys. Lett., **84**, 4298 (2004).

[85] G.M. Torrie and J.P. Valleau, J. Comp. Phys., **23**, 187 (1977).

[86] O.K.C. Tsui, F.K. Lee, B. Zhang, and P. Sheng, Phys. Rev E, **69**, 021704 (2004).

[87] R. Tuinier, D.G.A.L. Aarts, H.H. Wensink, and H.N.W. Lekkerkerker, Phys. Chem. Chem. Phys., **5**, 3707 (2003).

[88] R. van Roij, B. Mulder, and M. Dijkstra, Physica A, **261**, 374 (1998).

[89] R. van Roij, M. Dijkstra, and R. Evans, Europhys. Lett., **49**, 350 (2000).

[90] I. Vattulainen, T. Ala-Nissila, and K. Kankaala, Phys. Rev. Lett., **73**, 2513 (1994).

[91] J.A.C. Veerman and D. Frenkel, Phys. Rev. A, **43**, 4334 (1991).

[92] E. Velasco and E. Velasco, J. Chem. Phys., **109**, 2361 (1998).

[93] G. Vertogen and W.H. de Jeu, *Thermotropic liquid crystals, Fundamentals*, (Springer-Verlag, 1988).

[94] R.L.C. Vink, S. Wolfsheimer, and T. Schilling, J. Chem. Phys., **123**, 074901 (2005).

[95] P. Virnau and M. Müller, J. Chem. Phys., **120**, 10925 (2004).

[96] T.T.M. Vo, L.-J. Chen, and M. Robert, J. Chem. Phys., **119**, 5607 (2003).

[97] G.J. Vroege and H.N.W. Lekkerkerker, Colloids. Surf. A, **130**, 405 (1997).

[98] G.D. Wall and D.J. Cleaver, Phys. Rev. E, **56**, 4306 (1997).

[99] H.H. Wensink and G.J. Vroege, J. Chem. Phys., **119**, 6868 (2003).

[100] C. Wetter, Biologie in unserer Zeit, **3**, 81 (1985).

[101] B. Widom, J. Chem. Phys., **39**, 2802 (1963).

[102] J. Chem. Phys., **119**, 10209 (2003).

[103] T.D. Wilkinson, C.D. Henderson, D. Gil Leyva, and W.A. Crossland, J. Mater. Chem., **16**, 3359 (2006).

[104] S.-M. Yang, S.G. Jang, D.-G. Choi, S. Kim, and H.K. Yu, small, **2**, 458 (2006).

[105] Z.X. Zhang and J.S. van Duijneveldt, J. Chem. Phys., **124**, 154910 (2006).

Danksagungen

An dieser Stelle möchte ich mich bei all den Menschen bedanken, die zur Entstehung dieser Arbeit beigetragen haben.

An erster Stelle gilt mein Dank Herrn Prof. Lipowsky, der mir die Möglichkeit gegeben hat, die Arbeit an seinem Institut anzufertigen. Insbesondere möchte ich ihm für die inspirierende wissenschaftliche Atmosphähre in der Theorieabteilung danken.

Mein ganz besonderer Dank gilt Thomas Gruhn, der als wissenschaftlicher Betreuer immer als Ansprechpartner zur Verfügung stand. Ich möchte ihm danken für die vielen hilfreichen Diskussionen und Erklärungen, die mir sehr weitergeholfen haben, für das Korrekturlesen der Arbeit und für seine Anregungen.

Mein Dank gilt auch Tanja Schilling. Von ihr konnte ich viel Wissen über fortgeschrittene Monte Carlo Methoden erlernen.

Natürlich gilt mein Dank auch all den Leuten am Institut, die für eine gute Arbeitsatmosphäre gesorgt haben, insbesondere meinen jetzigen und ehemaligen Bürokolleginnen und Bürokollegen.

Schließlich möchte ich meiner Familie und meinem Paten danken, die mich während der gesamten Studienzeit und der Promotion unterstützt haben.